PHOTOSYNTHETICA
International Journal for Photosynthesis Research

DOI 10.32615/ps.2023.041 PHOTOSYNTHETICA 61 (SI): 61-68, 2023

Special issue in honor of Prof. Győző Garab

Photosynthetic reaction center/graphene bio-hybrid for low-power optoelectronics

J. VUJIN[*], T. SZABÓ[**], R. PANAJOTOVIC[*], A.G. VÉGH[***], L. RINYU[#], and L. NAGY[**,##,+]

Institute of Physics Belgrade, University of Belgrade, Pregrevica 118, 11080 Belgrade, Serbia[*]
Institute of Medical Physics and Informatics, University of Szeged, Korányi Fasor 9, H-6720 Szeged, Hungary[**]
HUN-REN Biological Research Centre, Szeged, Institute of Biophysics, Temesvári Krt. 62, Szeged, Hungary[***]
Isotope Climatology and Environmental Research Centre (ICER), HUN-REN Institute for Nuclear Research, Bem tér 18/c, 4026 Debrecen, Hungary[#]
HUN-REN Biological Research Centre, Szeged, Institute of Plant Biology, Temesvári Krt. 62, Szeged, Hungary[##]

Abstract

Photosynthetic reaction center (pRC) purified from *Rhodobacter sphaeroides* 2.4.1 purple bacteria was deposited on a graphene carrier exfoliated from the liquid phase and layered on the surface of SiO_2/Si substrate for optoelectronic application. Light-induced changes in the drain-source current *vs*. gate voltage are demonstrated. Dried photosynthetic reaction centers/graphene composite on SiO_2/Si shows a photochemical/-physical activity, as a result of interaction with the current flow in the graphene carrier matrix. The current changes are sensitive to light, due to the contribution from the charge separation in the pRC, and to the applied gate and drain-source voltages.

Keywords: field effect; graphene; liquid-phase exfoliation; optoelectronics; photosynthetic reaction center.

Introduction

At the turn of the 21st century, the synergy of research laboratories of fundamental and applied sciences together with the emerging request for advanced technologies led to the constructive interference of a wide range of disciplines (such as optoelectronics, (bio)photonics, nanotechnology, and nanobionics). A new generation of optoelectronic systems designed for energy conversion, imaging devices, optical switches, and sensors (Tamiaki *et al.* 2006, Nagy *et al.* 2010, 2014; Giraldo *et al.* 2014, Szabó *et al.* 2015, Daliento *et al.* 2017) became valuable tools in modern science and industry (Nagy and Magyar 2022). In addition, discovering new types of nano(bio)hybrid materials provides the possibility to create functional complexes that are considered in the literature as materials for the future (Darder *et al.* 2007, Shoseyov and Levy 2008, Nagy *et al.* 2014, Szabó *et al.* 2015).

Highlights

- Interaction between electric current in graphene and charge transfer in pRCs
- Electric field effect on charge separation in photosynthetic reaction centers
- Photosynthetic reaction center/graphene biohybrid for low-power optoelectronics

Received 11 September 2023
Accepted 2 November 2023
Published online 10 November 2023

[+]Corresponding author
e-mail: lnagy@sol.cc.u-szeged.hu

Abbreviations: AFM – atomic force microscopy; CNT – carbon nanotube; CVD – chemical vapor deposition; CWDL – continuous wave diode laser; DI – de-ionized; I_{DS} – drain-source current; IR – infrared; LB – Langmuir–Blodgett; LBA – Langmuir–Blodgett assembly; LPE – liquid phase exfoliation; mRGO – mercapto reduced graphene oxide; pRC – photosynthetic reaction center; RMS – root mean square; SEM – scanning electron microscopy; U_{DS} – drain-source voltage; U_G – gate voltage; UV – ultraviolet.

Acknowledgements: The research was supported by the European Union and the State of Hungary, co-financed by the European Regional Development Fund in the project of GINOP-2.3.2.-15-2016-00009 'ICER'. Thanks are due to the Hungarian Ministry of Innovation and Technology, National Research, Development and Innovation Fund (OTKA grants FK-139067). The authors R.P. and J.V. acknowledge funding provided by the Institute of Physics Belgrade, through a grant by the Ministry of Education, Science, and Technological Development of the Republic of Serbia. Partial support was provided by the Eötvös Loránd Research Network (ELKH KÖ-36/2021).
Conflict of interest: The authors declare that they have no conflict of interest.

The new generation of technologies offers unique solutions for specific tasks, such as optimizing the size of the devices and sample quantity, aiming single-molecular, fast, reversible, online, real-time, remote operation, and highly reproducible, sensitive, selective responses (Magyar *et al.* 2013, 2016; Luka e*t al.* 2015, Szabó *et al.* 2017). There is a large number of reports and reviews summarizing the advantageous properties of graphene for a wide range of applications referring to its unique transport properties (optical and electric conductivity) (Geim and Novoselov 2007, Geim 2009) as well as its extraordinarily high mechanical (strength and flexibility) and chemical stability (Blake e*t al.* 2008, Wang *et al.* 2008, Kim *et al.* 2009, Li *et al.* 2009).

To utilize the full potential of graphene, the selection of the appropriate methods of synthesis plays an important role. In addition to commonly used preparation methods, such as chemical vapor deposition (CVD) or mechanical exfoliation, liquid-phase exfoliation (LPE) followed by self-assembling Langmuir–Blodgett (LB) technique deposition represents a simple and inexpensive route that enables obtaining the thin, transparent, and low-resistance films of high crystal quality and graphene flakes free of chemical modifications (Coleman 2013, Kim *et al.* 2013, Tomašević-Ilić *et al.* 2016, Szabó *et al.* 2021).

The light-sensitive bio-hybrid composites, among the future generation of materials, has been attracted much attention because light-matter interaction is fundamental not only in basic and applied research but also in advanced technology, where fast and efficient performance is a prerequisite, *e.g.*, in information, security, energy conversion, and sensor technology (Wraight and Clayton 1974, Xua *et al.* 2004, Tamiaki *et al.* 2006, Nagy *et al.* 2010, 2014; Cogdell *et al.* 2013, Hartmann *et al.* 2014, Szabó *et al.* 2015, Daliento *et al.* 2017, Hajdu *et al.* 2017, 2021; Ryu *et al.* 2018, Allen *et al.* 2022). Bio-hybrid composites, as the combination of carbon-based materials and light-sensitive biological molecules such as photosynthetic proteins, can be designed to convert light very efficiently into different kinds of energy forms within a tuneable time from femtoseconds to seconds and wavelength range from UV to IR, at the same time fulfilling another requirement that they are highly degradable into environmentally safe products.

Various photosynthetic materials, from light-sensitive pigments through macromolecules and molecular complexes to individual organisms, are already successfully combined with metal or semiconductor electrodes, as well as with carbon-based carrier matrices to benefit from the properties of both the biological and inorganic carriers. Photosynthetic reaction center proteins (pRC), which are known as 'nature's solar batteries' (Jones 2009), are the focus of numerous research aiming to create light-responsive low-power hybrid bio-optoelectronic devices (Tangorra *et al.* 2014, Csiki *et al.* 2018, Heifler *et al.* 2020, Altamura *et al.* 2021). In addition to the classical three-electrode electrochemical cells, typical architecture is an electrolyte-gated field-effect organic transistor arrangement in which redistribution of the photogenerated charges by the pRC drives photocurrent in suitable aqueous solution (Andronescu and Schuhmann 2017, Takshi *et al.* 2017, Zhang *et al*. 2017, Di Lauro *et al.* 2020).

It is already demonstrated that pRC isolated from the natural environment can preserve its photochemical/-physical activity to a large extent when dissolved in a water-based detergent micellar system, organic solvents (*e.g.*, hexane) (Tandori *et al.* 1991, Warncke and Dutton 1993) or even dried on inorganic carrier surfaces. It is known from the middle of the 1970s that pRCs keep their photoactivity when dried in chromatophores (the photosynthetic membrane in cells) on glass plates (Vermeglio and Clayton 1976, Clayton 1978). Purified pRCs also keep the photochemical/-physical activity when dried in gelatin films (Rafferty and Clayton 1979), in trehalose glasses (Palazzo *et al.* 2008), when bound to carbon nanotubes (CNTs), and dried on optical glass (Dorogi *et al.* 2006, Hajdu *et al.* 2011) or graphene (Szabó *et al.* 2021). CNTs can mimic the membrane environment and have a stabilization effect on the light-separated charges – the lifetime of the light-induced charge pair is increased, the redox species in the pRCs interact with the CNT (Dorogi *et al.* 2006), and the photochemical stability is kept for several months (Magyar *et al.* 2011). Exceptional stability and mechanical flexibility of the pRC-electrode system were reported where pRCs were directly immobilized on transparent graphene oxide (mRGO) electrodes (Zhang *et al.* 2017).

In the present work, we characterized dried bacterial photosynthetic reaction centers/graphene composite on SiO_2/Si wafer aiming to examine its photochemical/-physical activity as a light energy-converting system. The liquid-phase exfoliated graphene film was tested as a carrier in this configuration and the deposition of pRC onto its surface formed of closely packed graphene nanoflakes was performed by the drop-casting method. Different techniques, such as optical spectroscopy (Raman spectroscopy), microscopy techniques (scanning electron microscopy – SEM and atomic force microscopy – AFM), and electrical measurement based on light-induced change in $I_{source\text{-}drain}/U_{gate}$, were applied to investigate the properties of the complex after its drying. We demonstrated that films obtained using the LB technique from LPE graphene dispersion, have overlapping and edge-to-edge contact nanoflakes, providing the uniform large-area thin film suitable for the role of the carrier in the bio-hybrid complex for the optoelectronic devices.

Materials and methods

Reaction center purification: Reaction center protein was isolated from the intracytoplasmic membrane fraction of *Rhodobacter sphaeroides* 2.4.1 purple bacterial strain by detergent (LDAO, N,N-dimethyldodecylamine-N-oxide) solubilization and further purified by ammonium sulfate precipitation followed by (*DEAE Sephacell*) anion-exchange chromatography (Tandori *et al.* 1995). Both the primary (Q_A) and the secondary (Q_B) electron acceptor quinones were extracted according to Okamura *et al.* (1975). The sample was adjusted to about 60 μM pRC concentration, kept in a freezer at –77°C, and diluted to

the required concentration (*ca.* 10^{-9} M) to ensure monolayer coverage (Szabó *et al.* 2013, 2021) when it was used.

Preparation of graphene thin films: The graphene films were made at a water–air interface by Langmuir–Blodgett assembly (LBA) technique using liquid-phase exfoliated graphene, following the protocol described in earlier publications (Kim *et al.* 2013, Matković *et al.* 2016, Tomašević-Ilić *et al.* 2016). The commercial graphite powder (*Sigma Aldrich-332461*) was dissolved in N-methyl-2-pyrrolidone (NMP, *Sigma Aldrich-328634*) at an initial concentration of 18 mg ml^{-1}. After 14 h of sonication, in a low-power ultrasonic bath (*Bransonic CPXH Ultrasonic & Cleaning Bath*, 30 W), graphene dispersion was centrifuged at 3,000 rpm for 60 min using *Force 1624* microcentrifuge. Sonication time was optimised for obtaining the highest yield and quality of graphene nanoflakes with our ultrasound bath. We used the low-power bath, and we were adding the cool water every couple of hours, which kept the temperature in the bath close to the room temperature. By adding a small amount of graphene dispersion (0.3 ml) into the half-filled beaker of de-ionized (DI) water (electrical resistance of 18.2 MΩ) hydrophobic graphene nanosheets self-organize and form a close-packed thin film at the water–air interface. For transferring this film onto SiO_2/Si substrate (SiO_2 thickness of 80 ± 5 nm; Tomašević-Ilić *et al.* 2016) a simple automated dip-coater system (motorized pull-out sample holder) with vertical speed control allowed us to pull the substrate slowly through the interface and scoop the film without disturbing its integrity. After the transfer, the graphene film was left to dry in ambient conditions. To assess the integrity and morphology of our graphene samples, we used an atomic force microscope *N-Tegra Prima* (*NTMDT*, Russia) operating in a semi-contact mode and scanning electron microscopy (SEM). SEM images were taken at 15 kV acceleration voltage using a *Tescan MIRA3* field-emission gun (*Tescan*, Czech Republic). The statistics of the size of graphene nanoflakes was obtained using the SEM inbuilt software tools for selecting, outlining, and measuring their lateral size. For measuring the roughness and thickness profile in AFM images, we used the free *Gwyddion* software.

Preparing the pRC/graphene composite: After the graphene film has passed the quality control in morphology measurements, photosynthetic reaction centers, purified from *Rb. sphaeroides* 2.4.1 strain, were deposited on its surface by drop-casting. Following our earlier protocols (Kim *et al.* 2013, Matković *et al.* 2016, Tomašević-Ilić *et al.* 2016), pRC solution was dropped on the surface of graphene. The RC concentration was set to 1.25 nM, and the amount of LDAO was reduced to 0.006%, well below the c.m.c. (0.01%) by dialysis, and 5 µL pRC solution was dried at room temperature under an air stream to ensure approximately single-layer pRC coverage (Szabó *et al.* 2013, 2021) in a 2-mm diameter spot. No specific attempt was made for oriented binding of the RC to graphene in these experiments; this can be the aim of the following investigations. However, by using CNT and pRCs in our earlier investigations, we learned that hydrophobic–hydrophobic interactions play probably the major role (the main thermodynamic driving force) of the stabilization (Dorogi *et al.* 2006). The probably random orientation of the pRC is determined by the hydrophobic interaction between the graphene flakes and the membrane-spanning part of the pRC, maybe, with the involvement of π-stacking, without specific selection of the e^--donor or the -acceptor side of the protein.

Raman microscopy for spectroscopy: Raman spectra were obtained using the *NTegra Spectra P9* (*NT-MDT Spectrum Instruments*, Limerick, Ireland) controller and microscope, having a 100× objective, under ambient air conditions at room temperature. For the excitation, a 473-nm wavelength diode laser was used, while for spectral decomposition, a 300 groves mm^{-1} grating covering the range of 180–3,500 cm^{-1}. Before experiments, the system was calibrated to the first peak of a silicon surface at 520.5 cm^{-1}. Individual spectra were collected with a step size of 500 nm covering a total area of 40 µm × 20 µm resulting in 3,200 spectra in total. After all spectra were averaged, the background was removed by fitting the lowest count values with a 7th-order polynomial (Szőke *et al.* 2020).

Measuring current-voltage characteristics: Before the measurement, connecting electrodes were fixed by water-based carbon paste (*SUPELCO*) to Si (gate) and graphene (source and drain). Light-induced changes were measured by exciting the sample with a continuous wave laser diode (*CWDL*, 2 W, 808 nm, *Roithner*). The signal was detected by a *Keithley 2700* multimeter (*Tektronix Inc.*, USA) with a 6.5-digit resolution (Magyar *et al.* 2011, Szabó *et al.* 2013, 2021). Based on our earlier experiments (Szabó *et al.* 2021), the intensity of the exciting CWDL light was set to the maximum value of the linear increase in the current signal, and grey filters (reached around 1 mW cm^{-2} of light intensity) were used to minimize the probability of multiple excitations of the pRC. The measurements were controlled, and the data were collected and analysed using the self-developed *LabVIEW* software. The experimental arrangement for measuring light-induced changes in the electric properties of the graphene/pRC bio-hybrid is depicted in Fig. 1.

Results and discussion

Structural characterizations: Information about the structural characteristic of the film and its morphology was obtained using SEM (Fig. 2). It can be noticed in Fig. 2*A* that graphene flakes completely cover the substrate forming the film through overlapping and positioning side-by-side. For SEM image analysis, the nanoflakes were selected using the inbuilt instrument software, and their size was measured with appropriate software tools. The arrangement of the graphene flakes implies the mesoporous structure of the film. Fig. 2*B* presents histograms of the lateral sizes of graphene flakes, indicating that their average diameter was 130 ± 10 nm.

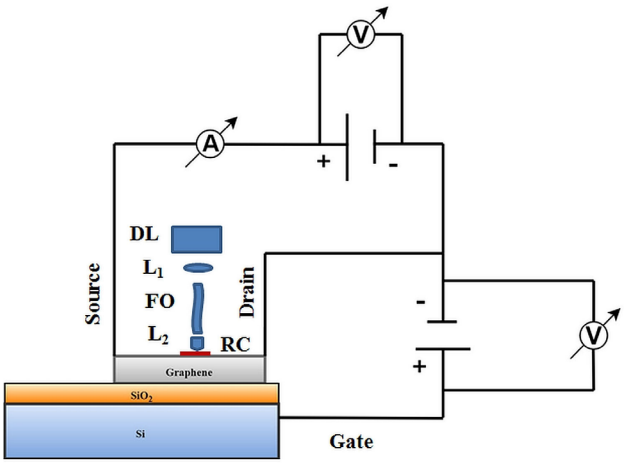

Fig. 1. Schematic representation of the experimental arrangement. CWDL – diode laser; L_1 and L_2 – lenses; FO – fiber optics; RC – reaction centre.

Further analysis of the graphene film surface was performed by AFM. The AFM topographic images (Fig. 3) confirmed good surface coverage of the SiO_2/Si substrate by overlapping graphene nanoflakes. Using the statistical analysis with the *Gwyddion* software enabled us to estimate the average roughness of the film in the order of 10 nm. The overlap of individual graphene nanoflakes in the film prevented the exact measurement of their thickness by AFM. However, it has been established in our previous work (Matković *et al*. 2016) that the graphene flakes obtained using our exfoliation protocol were composed of a few layers, comparable to the size of the pRC particle.

Considering that the pRC water solution also contains the surfactant (although well below the c.m.c., which is sufficiently enough to keep the pRC in suspension) that stabilizes the protein particles and prevents their agglomeration, we assumed that the drop-casted pRC would likely be randomly distributed over the drop area and not accumulate anywhere in particular. Therefore, we can consider our composite structure to be close to a monolayer of pRC on graphene, as in our earlier experiments (Szabó *et al.* 2013, 2021).

To confirm the pRC adsorption on the graphene film, the sample coverage was analysed by Raman microscopy in the range of 180–3,500 cm^{-1} where the characteristic peaks of Si, graphene, pRC carotenoids, and NH- and saturated CH-bands can be visualized (Adar 2022). As a reference, Raman spectra of multilayer pRCs deposited onto SiO_2/Si were recorded. Fig. 4 shows that the characteristic peaks of Si/SiO_2, graphene, and the numbers of the pRC peak can be clearly identified and coincide well with the ones reported already in the literature for the pRC (Robert 1990) and for Si/SiO_2/graphene substrates (Hrubý *et al.* 2020). At 473-nm laser excitation preferentially, the carotenoids bound to pRC are excited and show characteristic resonance peaks. When RCs are bound to graphene film, probably, due to large overlap with graphene, the carotenoid peaks are reduced considerably, however, in the range of CH-NH bands of the spectrum, the pRC binding is indicated. The positions and modifications of the peaks due to different pRC conditions (substrate binding, environment, light–dark, *etc*.) are a matter of further investigation.

Electric current measurements: The thin graphene film transferred onto the SiO_2/Si substrate (Si is n-type of semiconductor) shows the diode-like I/V characteristics due to the good contact at the interface (Fig. 1). Fig. 5 shows that the current in the dark equilibrium can clearly be distinguished in the negative and the positive directions. When the device is illuminated by light, current flow opens in the positive U_G (Fig. 5) without affecting the current in the negative U_G (Fig. 5) with or without the pRC coverage.

The asymmetric light response with the gate voltage is better demonstrated when the 'light minus dark' drain-source (I_{DS}) current is plotted *vs*. the gate voltage (U_G, Fig. 6). In this representation, the signal is compensated with any (electric and/or thermal) effect accompanying the light excitation in the Si, SiO_2, and graphene phases and/or at the interfaces. Light-induced changes in the I_{DS} can be seen only in the positive U_G range and are enhanced significantly when graphene is functionalized with the pRCs. The change in the drain-source current does not show dependence on the drain-source voltage (U_{DS}) (in the investigated range, 0–1,000 mV, at least), however, is highly sensitive to U_G.

There are multiple effects of the excitation of this layered structure by light in the near-infrared range (the excitation wavelength in our case was 808 nm).

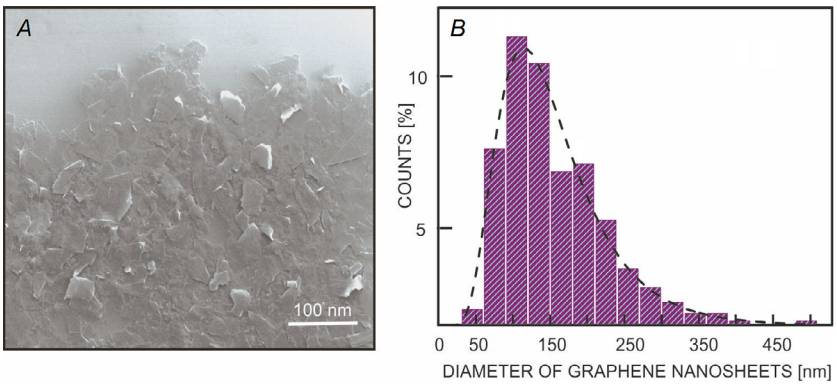

Fig. 2. (*A*) SEM image of graphene film on SiO_2/Si wafer, (*B*) histograms of graphene nanosheet diameter obtained from five 2 × 2 μm² SEM images (~1,400 flakes). *The black dashed line* corresponds to the log-normal fit.

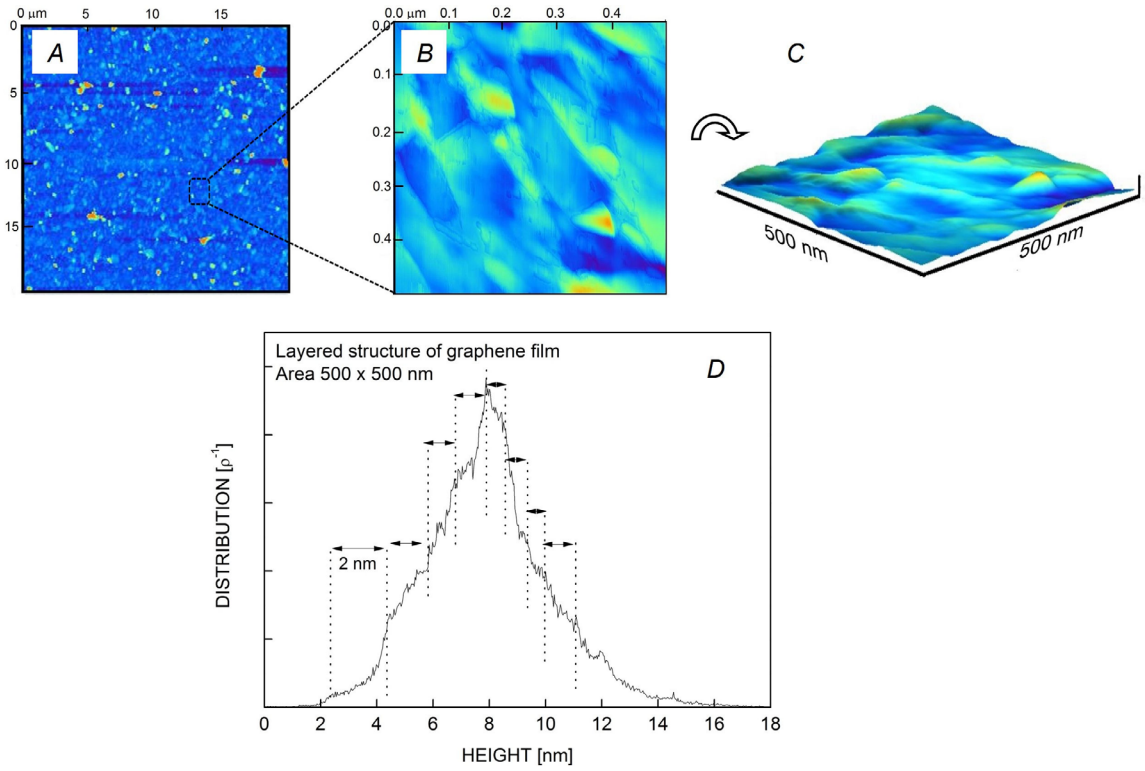

Fig. 3. AFM mapping of graphene thin films on the SiO2/Si substrate (colours represent the virtual gradient in height): top images – graphene flakes are fully covering the substrate (20 × 20 µm scan), with mean height distribution of 36 ± 2 nm, and roughness parameter (root mean square, RMS) of 13 ± 5 nm, detail of a large scan – height distribution shows the layered structure and overlap of graphene flakes (500 × 500 nm scan), with the thickness ranging from less than 1 nm to several nanometres.

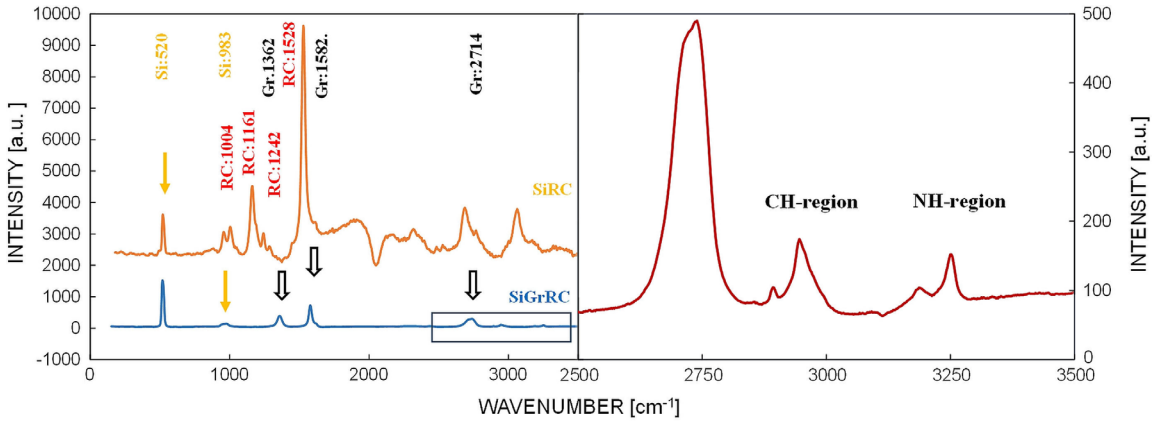

Fig. 4. *Left*: Raman intensity of RC thin film combined on graphene/SiO_2/Si substrate (SiGrRC) and RC deposited on SiO_2/Si (SiRC) in the range of 180–3,700 cm^{-1}. The characteristic peaks of SiO_2/Si, graphene, and reaction centres are indicated. *Solid and open arrows* indicate positions of SiO_2/Si and graphene, respectively. *The open box* indicates the range of the spectrum indicated in the right figure. *Right*: Raman intensity of RC thin film combined on graphene/SiO_2/Si substrate in the CH-NH range of the spectrum. The spectral range is depicted from the range indicated in the open box in the left figure.

Although graphene film does not have a plasmonic excitation at this wavelength, thermal dissipation of the absorbed photon energy is very likely an alternative reason for the change in I/V. In addition, due to the relatively large transparency of the graphene film, light can induce an electronic excitation of the Si bulk, as well as the conductivity change at the interfaces of Si/SiO_2/graphene. Structural and functional conditions of the pRC deposition were optimized to reduce the possible artifacts (*e.g.*, due to integrity of the protein structure, overexcitation of the photochemistry/-physics of the pRC, possible effects of the detergent on the RC–substrate interaction; *see* 'Materials and methods, Preparing the pRC/graphene composite') in the light-induced current changes.

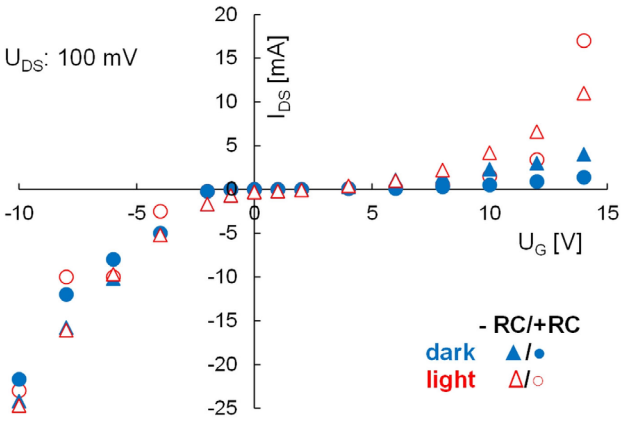

Fig. 5. Typical transient of the drain-source current (I_{DS}) *vs*. gate voltage (U_G) in graphene on silicon oxide with or without RCs in the dark or under light excitation, as indicated. Measurement was carried out with drain-source voltage (U_{DS}) fixed at 100 mV.

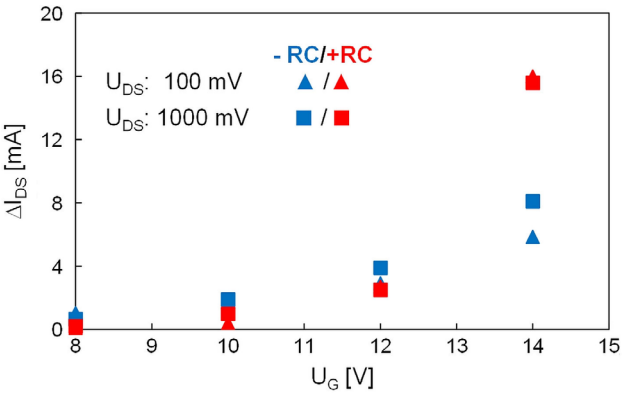

Fig. 6. Light-minus-dark drain-source current (ΔI_{DS}) of the graphene with or without the RC as a function of the gate voltage (U_G) under two drain-source voltage values (U_{DS} = 100 mV and 1,000 mV, as indicated).

Because of the effects, which are 'non-specific' to the charge transfer in pRCs (possible artifact-like signals, temperature effect, events in the bulk phase of Si, SiO_2, graphene or at the interfaces, *etc.*), the absolute current values show some variations, so that Fig. 5 shows results of individual measurements with typical characteristics. However, these non-specific 'side effects' can be subtracted, the results of individual samples can be compensated, and the light-induced current enhancement is better visualized when light-minus-dark transients are represented.

It must be noted that the measurements were carried out under conditions when pRCs were dried without reconstituting the donor and acceptor sides by artificial external e^- donors or acceptors. Under these conditions, the pRC is not capable of performing multiple turnovers of the photocycle, only single charge separation followed by charge recombination occurs. In pRCs purified from *Rb. sphaeroides* 2.4.1, the e^--acceptor quinones were completely depleted, PBPheo → P^+BPheo^- charge separation occurred in a ps-time scale after excitation by light followed by recombination in about tens of nanoseconds (P^+BPheo^- → PBPheo) (Nagy *et al.* 2015). Here, P and P^+, BPheo, and $BPheo^-$ are the reduced and oxidized primary e^--donor and bacteriopheophytin, respectively. There is a large number of reports in the literature about direct electronic interaction between redox centers of the pRC and carrier matrices (*e.g.*, electrode surfaces in electrochemical cells for attempting photovoltaic or biosensor applications). In these reported experiments, the full photocycle of the pRC is fulfilled, usually in traditional electrochemical cells (*cf.* 'Introduction'). At the present state of our experiments, we do not have direct evidence for the contribution either of charge transfer between the pRC and graphene or of the effect of the electric field. Because the electron transfer through the pRC is blocked, the redox transient of the pRC probably does not contribute significantly to the charge density in the graphene layer, however, the interaction between the electric fields can be accounted for.

Conclusions: This is the first report to show that the dried bacterial photosynthetic reaction centers/graphene composite on SiO_2/Si performs a photochemical/-physical activity and this activity is in interaction with the graphene carrier matrix. The current through the possible Si/SiO_2/graphene/pRC junction is sensitive to light, due to the contribution from the light-activated pRC to the applied gate and DS voltages. Our data provide useful information for the future direction of creating simple and efficient light-responsive low-power hybrid bio-optoelectronic organic devices. One reasonable improvement of dry pRC/graphene devices could be achieved by providing specific donor–acceptor sites on graphene for pRCs to bind at a specific orientation. A specific pattern and density of these sites will also provide more uniform and controlled adsorption of a larger amount of pRC, which in turn will improve their efficiency as an electric power source and/or specific optoelectronic devices. These experiments can also be done using specifically modified RCs in which the light-induced turnover rate and the spectral sensitivity can be modulated in a wide range in future experiments.

References

Adar F.: Interpretation of Raman spectrum of proteins. – Spectroscopy **37**: 9-13, 2022.

Allen J.P., Chamberlain K.D., Olson T.L., Williams J.C.: A bound iron porphyrin is redox active in hybrid bacterial reaction centers modified to possess a four-helix bundle domain. – Photoch. Photobio. Sci. **21**: 91-99, 2022.

Altamura E., Albanese P., Marotta R., Mavelli F.: Chromatophores efficiently promote light-driven ATP synthesis and DNA transcription inside hybrid multicompartment artificial cells. – PNAS **118**: e2012170118, 2021.

Andronescu C., Schuhmann W.: Graphene-based field effect transistors as biosensors. – Curr. Opin. Electrochem. **3**: 11-17, 2017.

Blake P., Brimicombe P.D., Nair R.R. *et al.*: Graphene-based liquid crystal device. – Nano Lett. **8**: 1704-1708, 2008.

Clayton R.K.: Effects of dehydration on reaction centers from *Rhodopseudomonas sphaeroides*. – BBA-Bioenergetics **504**: 255-264, 1978.

Cogdell R.J., Gardiner A.T., Molina P.I., Cronin L.: The use and misuse of photosynthesis in the quest for novel methods to harness solar energy to make fuel. – Philos. T. Roy. Soc. B **371**: 20110603, 2013.

Coleman J.N.: Liquid exfoliation of defect-free graphene. – Acc. Chem. Res. **46**: 14-22, 2013.

Csiki R., Drieschner S., Lyuleeva A. *et al.*: Photocurrent generation of biohybrid systems based on bacterial reaction centers and graphene electrodes. – Diam. Relat. Mater. **89**: 286-292, 2018.

Daliento D., Chouder A., Guerriero P. *et al.*: Monitoring, diagnosis, and power forecasting for photovoltaic fields: a review. – Int. J. Photoenergy **2017**: 1356851, 2017.

Darder M., Aranda P., Ruiz-Hitzky E.: Bionanocomposites: a new concept of ecological, bioinspired and functional hybrid materials. – Adv. Mater. **19**: 1309-1319, 2007.

Di Lauro M., la Gatta S., Bortolotti C.A. *et al.*: A bacterial photosynthetic enzymatic unit modulating organic transistors with light. – Adv. Electron. Mater. **6**: 1900888, 2020.

Dorogi M., Bálint Z., Mikó C. *et al.*: Stabilization effect of single-walled carbon nanotubes on the functioning of photosynthetic reaction centers. – J. Phys. Chem. B **110**: 21473-21479, 2006.

Geim A.K.: Graphene: status and prospects. – Science **324**: 1530-1534, 2009.

Geim A.K., Novoselov K.S.: The rise of graphene. – Nat. Mater. **6**: 183-191, 2007.

Giraldo J.P., Landry M.P., Faltermeier S.M. *et al.*: Plant nanobionics approach to augment photosynthesis and biochemical sensing. – Nat. Mater. **13**: 400-408, 2014.

Hajdu K., Balderas-Valadez R.F., Carlino A. *et al.*: Porous silicon pillar structures/photosynthetic reaction centre protein hybrid for bioelectronic applications. – Photoch. Photobio. Sci. **21**: 13-22, 2021.

Hajdu K., Szabó T., Magyar M. *et al.*: Photosynthetic reaction center protein in nanostructures. – Phys. Status Solidi B **248**: 2700-2703, 2011.

Hajdu K., Szabó T., Sarrai A.E. *et al.*: Functional nanohybrid materials from photosynthetic reaction center proteins. – Int. J. Photoenergy **2017**: 9128291, 2017.

Hartmann V., Kothe T., Pöler S. *et al.*: Redox hydrogels with adjusted redox potential for improved efficiency in Z-scheme inspired biophotovoltaic cells. – Phys. Chem. Chem. Phys. **16**: 11936-11941, 2014.

Heifler O., Carmeli C., Carmeli I.: Chemical tagging of membrane proteins enables oriented binding on solid surfaces. – Langmuir **36**: 4556-4562, 2020.

Hrubý J., Vavrečková Š., Masaryk L. *et al.*: Deposition of tetracoordinate Co(II) complex with chalcone ligands on graphene. – Molecules **25**: 5021, 2020.

Jones M.R.: The petite purple photosynthetic powerpack. – Biochem. Soc. T. **37**: 400-407, 2009.

Kim H., Mattevi C., Kim H.J. *et al.*: Optoelectronic properties of graphene thin films deposited by a Langmuir–Blodgett assembly. – Nanoscale **5**: 12365-12374, 2013.

Kim K.S., Zhao Y., Jang H. *et al.*: Large-scale pattern growth of graphene films for stretchable transparent electrodes. – Nature **457**: 706-710, 2009.

Li X., Zhu Y., Cai W. *et al.*: Transfer of large-area graphene films for high-performance transparent conductive electrodes. – Nano Lett. **9**: 4359-4363, 2009.

Luka G., Ahmadi A., Najjaran H. *et al.*: Microfluidics integrated biosensors: a leading technology towards lab-on-a-chip and sensing applications. – Sensors-Basel **15**: 30011-30031, 2015.

Magyar M., Hajdu K. Szabó T. *et al.*: Long term stabilization of reaction center protein photochemistry by carbon nanotubes. – Phys. Status Solidi B **248**: 2454-2457, 2011.

Magyar M., Hajdu K., Szabó T. *et al.*: Sensing hydrogen peroxide by carbon nanotube/horse radish peroxidase bio-nanocomposite. – Phys. Status Solidi B **250**: 2559-2563, 2013.

Magyar M., Rinyu L., Janovics R. *et al.*: Real-time sensing of hydrogen peroxide by ITO/MWCNT/horseradish peroxidase enzyme electrode. – J. Nanomater. **2016**: 2437873, 2016.

Matković A., Milošević I., Milićević M. *et al.*: Enhanced sheet conductivity of Langmuir–Blodgett assembled graphene thin films by chemical doping. – 2D Materials **3**: 015002, 2016.

Nagy L., Hajdu K., Fisher B. *et al.*: Photosynthetic reaction centres – from basic research to application possibilities. – Not. Sci. Biol. **2**: 7-13, 2010.

Nagy L., Kiss V., Brumfeld V. *et al.*: Thermal effects and structural changes of photosynthetic reaction centers characterized by wide frequency band hydrophone: Effects of carotenoids and terbutryn. – Photochem. Photobiol. **91**: 1368-1375, 2015.

Nagy L., Magyar M.: No alternatives to photosynthesis: from molecules to nanostructures. – In: Jeschke P., Starikov E.B. (ed.): Agricultural Biocatalysis: Theoretical Studies and Photosynthesis Aspects. Pp. 210-247. Jenny Stanford Publishing, New York 2022.

Nagy L., Magyar M., Szabó T. *et al.*: Photosynthetic machineries in nano-systems. – Curr. Protein Pept. Sci. **15**: 363-373, 2014.

Okamura M.Y., Isaacson R.A., Feher G.: Primary acceptor in bacterial photosynthesis: obligatory role of ubiquinone in photoactive reaction centers of *Rhodopseudomonas sphaeroides*. – PNAS **72**: 3491-3495, 1975.

Palazzo G., Francia F., Mallardi A. *et al.*: Water activity regulates the Q_A^- to Q_B electron transfer in photosynthetic reaction centers from *Rhodobacter sphaeroides*. – J. Am. Chem. Soc. **130**: 9353-9363, 2008.

Rafferty C.N., Clayton R.K.: Linear dichroism and the orientation of reaction centers of Rhodopseudomonas sphaeroides in dried gelatin films. – BBA-Bioenergetics **545**: 106-121, 1979.

Robert B.: Resonance Raman studies of bacterial reaction centers. – BBA-Bioenergetics **1017**: 99-111, 1990.

Ryu D.H., Kim Y.J., Kim S.I. *et al.*: Thylakoid-deposited micro-pillar electrodes for enhanced direct extraction of photosynthetic electrons. – Nanomaterials **8**: 189, 2018.

Shoseyov O., Levy I.: NanoBioTechnology: BioInspired Devices and Materials of the Future. Pp. 485. Humana Press, Totowa 2008.

Szabó T., Bencsik G., Magyar M. *et al.*: Photosynthetic reaction centers/ITO hybrid nanostructure. – Mater. Sci. Eng. C **33**: 769-773, 2013.

Szabó T., Csekő R., Hajdu K. *et al.*: Sensing photosynthetic herbicides in an electrochemical flow cell. – Photosynth. Res. **132**: 127-134, 2017.

Szabó T., Magyar M., Hajdu K. *et al.*: Structural and functional hierarchy in photosynthetic energy conversion – from molecules to nanostructures. – Nanoscale Res. Lett. **10**: 458, 2015.

Szabó T., Panajotović R., Vujin J. *et al.*: Photosynthetic reaction-center/graphene biohybrid for optoelectronics. – J. Nanosci. Nanotechnol. **21**: 2342-2350, 2021.

Szőke Á.F., Szabó G.S., Hórvölgyi Z. *et al.*: Accumulation of 2-acetylamino-5-mercapto-1,3,4-thiadiazole in chitosan coatings for improved anticorrosive effect on zinc. – Int. J. Biol. Macromol. **142**: 423-431, 2020.

Takshi A., Yaghoubi H., Wang J. *et al.*: Electrochemical field-effect transistor utilization to study the coupling success rate of photosynthetic protein complexes to cytochrome *c*. – Biosensors **7**: 16, 2017.

Tamiaki H., Nishihara K., Shibata R.: Synthesis of self-aggregative zinc chlorophylls possessing polymerizable esters as a stable

model compound for main light-harvesting antennas of green photosynthetic bacteria. – Int. J. Photoenergy **2006**: 090989, 2006.

Tandori J., Nagy L., Maróti P.: Semiquinone oscillation as a probe of quinone/herbicide binding in bacterial reaction centers. – Photosynthetica **25**: 159-166, 1991.

Tandori J., Nagy L., Puskás A. *et al.*: The Ile^{L229} → Met mutation impairs the quinone binding to the Q_B-pocket in reaction centers of *Rhodobacter sphaeroides*. – Photosynth. Res. **45**: 135-146, 1995.

Tangorra R.R., Antonucci A., Milano F. *et al.*: Photoactive film by covalent immobilization of a bacterial photosynthetic protein on reduced graphene oxide surface. – MRS Online Proceedings Library **1717**: 12-18, 2014.

Tomašević-Ilić T., Pešić J., Milošević I. *et al.*: Transparent and conductive films from liquid phase exfoliated graphene. – Opt. Quant. Electron. **48**: 319, 2016.

Vermeglio A., Clayton R.K.: Orientation of chromophores in reaction centers of *Rhodopseudomonas sphaeroides*. Evidence for two absorption bands of the dimeric primary electron donor. – BBA-Bioenergetics **449**: 500-515, 1976.

Wang X., Zhi L., Müllen K.: Transparent, conductive graphene electrodes for dye-sensitized solar cells. – Nano Lett. **8**: 323-327, 2008.

Warncke K., Dutton P.L.: Experimental resolution of the free energies of aqueous solvation contributions to ligand-protein binding: quinone-Q_A site interactions in the photosynthetic reaction center protein. – PNAS **90**: 2920-2924, 1993.

Wraight C.A., Clayton R.K.: The absolute quantum efficiency of bacteriochlorophyll photooxidation in reaction centres of *Rhodopseudomonas sphaeroides*. – BBA-Bioenergetics **333**: 246-260, 1974.

Xua J., Bhattacharya P., Váró G.: Monolithically integrated bacteriorhodopsin/semiconductor opto-electronic integrated circuit for a bio-photoreceiver. – Biosens. Bioelectron. **19**: 885-892, 2004.

Zhang H., Carey A.-M., Jeon K.-W. *et al.*: A highly stable and scalable photosynthetic reaction center–graphene hybrid electrode system for biomimetic solar energy transduction. – J. Mater. Chem. A **5**: 6038-6041, 2017.

LANGMUIR

pubs.acs.org/Langmuir Article

Direct Probing of Water Adsorption on Liquid-Phase Exfoliated WS_2 Films Formed by the Langmuir–Schaefer Technique

Jasna Vujin, Weixin Huang, Jovan Ciganović, Sylwia Ptasinska, and Radmila Panajotović*

Cite This: *Langmuir* 2023, 39, 8055–8064 Read Online

ACCESS | Metrics & More | Article Recommendations | Supporting Information

ABSTRACT: Tungsten disulfide, a transition metal dichalcogenide, has numerous applications as active components in gas- and chemical-sensing devices, photovoltaic sources, photocatalyst substrates, etc. In such devices, the presence of water in the sensing environment is a factor whose role has not been well-understood. To address this problem, the *in situ* probing of H_2O molecule adsorption on WS_2 films supported on solid substrates has been performed in a near-ambient pressure X-ray photoelectron spectroscopy (NAP-XPS) setup. Instead, on the individual nanoflakes or spray-coated samples, the measurements were performed on highly transparent, homogeneous, thin films of WS_2 nanosheets self-assembled at the interface of two immiscible liquids, water and toluene, transferred onto a solid substrate by the Langmuir–Schaefer technique. This experiment shows that edge defects in nanoflakes, tungsten dangling bond ensuing the exfoliation in the liquid phase, represent active sites for the WO_3, WO_{3-x}, and $WO_3{\cdot}nH_2O$ formation under ambient conditions. These oxides interact with water molecules when the WS_2 films are exposed to water vapor in the NAP-XPS reaction cell. However, water molecules do not influence the W–S chemical bond, thus indicating the physisorption of H_2O molecules at the WS_2 film surface.

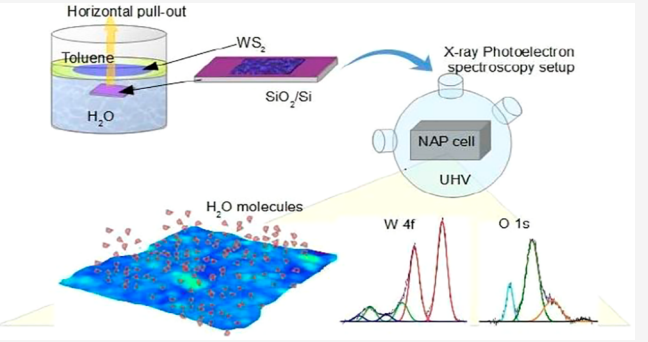

INTRODUCTION

Ambient humidity is an important factor in material research, especially in devices involving very thin layers of two-dimensional (2D) materials.[1,2] When working under ambient conditions, the information about the influence of adsorbed water molecules on the surface of 2D materials represents essential information before understanding the interaction between any other adsorbed molecules and the 2D-material. If devices based on 2D-materials are designed to detect different types of analytes, their high sensitivity to humidity could cause significant issues and discrepancies during the measurements, concerning the consistency and stability of the electrical signal or their chemical response to the presence of the analyte. Hence, an insight into the variations in surface sensitivity of 2D-material thin films to ambient humidity is necessary. During the interaction with water molecules, the electronic properties of 2D-materials, such as resistance or charge carrier concentration, are easily modulated, implying that these materials can also be used as promising components of humidity sensors.[3−5]

Tungsten disulfide (WS_2), the prominent member of the 2D transition metal dichalcogenide (TMD) material family, has attracted considerable attention regarding its potential application in the field of sensors as a result of its high surface-to-volume ratio, chemically active edges, and good electrical properties.[6] The ultrahigh surface sensitivity to the surrounding environment allows for the modification of the WS_2 surface, forming active biointerfaces convenient for biomedical applications.[7−9] 2D WS_2 represents a very suitable platform for a sensor not only for biomolecules (proteins, DNA, and liposomes) and biological cells but also for various gas molecules, such as CO, H_2S, NH_3, NO_2, and H_2.[10−13] WS_2 has also shown exceptional water-sensing properties with a prompt response and recovery time and good repeatability and stability that opened the possibility to use it as a humidity sensor for environmental monitoring or in healthcare applications as real-time dynamic monitoring of human breath.[14,15]

In recent reports, it has been shown that the properties of WS_2 humidity-sensing devices depend on the defects present on the WS_2 nanosheets.[14−18] Greater sensitivity to humidity can be a consequence of the existence of the low-coordination kinks, step edges, and dangling bonds at the edges of the WS_2 nanosheets. All of these types of defects have a significant role

Received: January 12, 2023
Revised: May 13, 2023
Published: June 2, 2023

https://doi.org/10.1021/acs.langmuir.3c00107
Langmuir 2023, 39, 8055–8064

in the humidity-sensing behavior because they represent potential active sites available for the adsorption/desorption of H_2O molecules. In the experiment of Jha et al.,[17] it was reported that treatment of suspended WS_2 nanosheets with ultraviolet (UV) light improved linearity of the sensor at the expense of its response to humidity. They suggested that this effect might be due to the decreased amount of oxygen species after the UV light treatment, which, according to the Grotthuss mechanism,[19] serves as a chemisorption site for water molecules. They also suggested that the existence of oxygenized sites on the WS_2 nanosheets is a consequence of the exfoliation protocol, which included acetone ketyl free radicals acting as a reducing agent. However, the direct evidence of the oxygen species in such samples and the mechanism of H_2O adsorption on WS_2 nanosheets are still missing.

The presence of humidity in ambient conditions is particularly important for the stability of the operation of gas sensors, which presents a significant limitation to their practical use.[20] In field-effect transistor (FET) gas sensors based on multilayer mechanically exfoliated WS_2 nanoflakes, Huo et al.[16] found that the drain current and photosensitivity of the device are higher in vacuum than in ambient air. Their density functional theory (DFT) calculations showed that O_2 and H_2O molecules from air can be physically adsorbed on the surface of WS_2 nanoflakes and withdraw electrons from it, thus reducing its conductivity. As a consequence, the response of the FET sensor to reducing gases (NH_3) may be good but not so to O_2, for example. Therefore, to design efficient, stable, and reliable gas sensors based on the WS_2 nanoflakes, it is necessary to understand the mechanism of water adsorption on its surface.

Considering different methods of 2D-material production,[14−16] liquid-phase exfoliation (LPE) stood out as a simple, inexpensive, and highly effective technique for obtaining a high yield of mono- and few-layer nanoflakes with the inherent (edges) types of defects.[21−23] To use the full potential of LPE-processed WS_2 nanosheets for sensing applications, thin films need to be fabricated with a high degree of order and continuity and a uniform surface. Conventional few-step deposition methods of WS_2 dispersion (and other 2D-materials), such as drop-casting[17] and spray and spin coating,[24−26] suffer from non-uniformity, agglomeration of nanoflakes arising during solvent evaporation, lack of reproducibility, and lack of control over the thickness of the films, which all affect the quality of the sensor response. Langmuir−Blodgett (LB) and Langmuir−Schaefer (LS) interface assemblies were recognized as promising methods for overcoming existing drawbacks,[27−29] especially in the case of self-assembled thin films of LPE graphene at the interface between two phases, liquid/gas or liquid/liquid.[27,30−32] In particular, liquid/liquid interfaces provide a suitable opportunity for the formation of uniform films with better confinement of TMD nanosheets. Few reports exist of TMD assembly at the liquid/liquid interface,[25,33,34] among them only one concerning the WS_2 nanosheet-based film.[35] Clark et al.[35] have demonstrated that continuous and closed-packed thin films can be obtained through the spontaneous creation of liquid/liquid assembly of TMDs (WS_2, MoS_2, and ReS_2), mixing the TMD nanosheet dispersion and octadecene by manual shaking. To avoid additional processing steps of film assembling and uncontrollable use of TMD dispersion, Nelson et al.[25] have proposed another approach, which is followed by direct injection of the MoS_2 dispersion to the preformed liquid/liquid interface. However, no such attempt for producing the WS_2 film from nanoflakes has been made thus far, on octadecene or any other solvent on top of water.

In this work, we characterized the liquid-phase exfoliated WS_2 films obtained at the interface of two immiscible liquids, water and toluene, for the first time. The thin WS_2 films supported on the solid substrate by the LS technique were then exposed to pure water vapor in near ambient conditions for the direct, *in situ* measurement of water molecule adsorption on their surface formed of closely packed WS_2 nanoflakes. Various characterization techniques were employed to investigate the properties of the LPE-LS WS_2 films: optical spectroscopy methods [ultraviolet−visible (UV−vis) and Raman spectroscopy], near-ambient pressure X-ray photoelectron spectroscopy (NAP-XPS), as well as microscopy techniques [scanning electron microscopy (SEM) and atomic force microscopy (AFM)]. We demonstrated that films formed using the LS technique from LPE WS_2 dispersion have overlapping and edge-to-edge contact of WS_2 nanoflakes, providing a uniform large-area thin film. Notably, these films exhibit defects at the edges of overlapping nanoflakes that provide a dense grid of active sites for molecular adsorption. This simple and inexpensive protocol produces much more compact and highly uniform, thin WS_2 films that can be deposited onto various substrates compared to those previously reported.[12,17,18,33]

We demonstrated that the heating in air or vacuum does not change the structure of such films, which allows them to be used in sensing devices at a high temperature without degradation. The NAP-XPS experimental data show that the water molecules adsorb predominantly on tungsten oxide sites, which originate from the exfoliation and film synthesis in ambient conditions, on and between the nanoflakes forming the film.

EXPERIMENTAL SECTION

Exfoliation and Characterization of WS_2 Dispersions. For liquid-phase exfoliation of WS_2 and preparation of dispersion, we followed the protocol described in an earlier paper.[36] We used tungsten(IV) sulfide powder (243639, Sigma-Aldrich) and *N*-methyl-2-pyrrolidone (NMP, biotechnology grade, ≥99.7%, 494496, Sigma-Aldrich) as a solvent. To optimize the exfoliation conditions for the highest yield of WS_2 nanoflakes in solution, the initial WS_2 powder concentration and sonication time were tuned. Four different initial concentrations of WS_2 dispersion were prepared: 6, 12, 18, and 24 mg mL^{-1}. All dispersions were sonicated in a low-power ultrasonic bath (Bransonic CPXH ultrasonic cleaning bath) for 14 h at room temperature (T = 23 °C) and humidity of 25−30%. To prevent aggregation and reduce the presence of non-exfoliated materials, the WS_2 dispersion was cascade-centrifuged: after the first 15 min cycle at 3000 rpm, the solution was decanted and the supernatant was centrifuged at 6000 rpm for another 15 min. The optical characterization of WS_2 dispersion was performed using UV−vis spectroscopy (see section 1 of the Supporting Information). On the basis of the results, the dispersion with 12 mg mL^{-1} of initial WS_2 concentration was chosen for further study.

Fabrication and Deposition of LPE LS WS_2 Films. The liquid-phase exfoliated WS_2 films were prepared at the water/toluene interface by the LS method. In a 15 mL beaker filled with 9 mL of deionized water (18 MΩ cm^{-1}), the substrate was immersed horizontally. The liquid interface was formed by adding 1 mL of toluene (≥99.7%, Sigma-Aldrich). The 0.3 mL of WS_2 dispersion was continuously cast down the inside wall of the beaker using the pipet. Passing through toluene, WS_2 nanoflakes gradually self-organized into a close-packed thin film at the water/toluene interface. After the WS_2 film was created, most toluene was gently removed with a syringe. The WS_2 films were then transferred onto substrates (SiO_2/Si, Au-

https://doi.org/10.1021/acs.langmuir.3c00107
Langmuir 2023, 39, 8055−8064

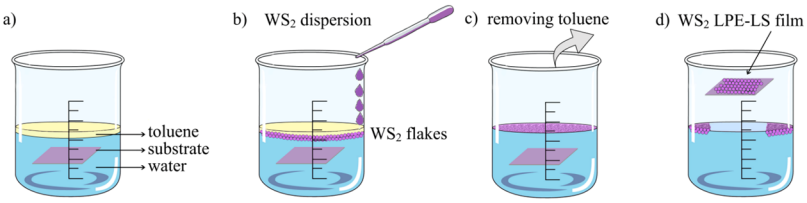

Figure 1. Schematic representation of the steps during the LPE-LS WS_2 film assembly by the LS method: (a) formation of the water/toluene interface, where the target substrate was previously horizontally immersed in the water, (b) introduction of LPE WS_2 dispersion down the inner wall of the beaker, where WS_2 nanoflakes pass through the toluene and are self-organized at the interface between liquids, (c) removing toluene, (d) thin WS_2 film transferring on a solid substrate by pulling through the interface.

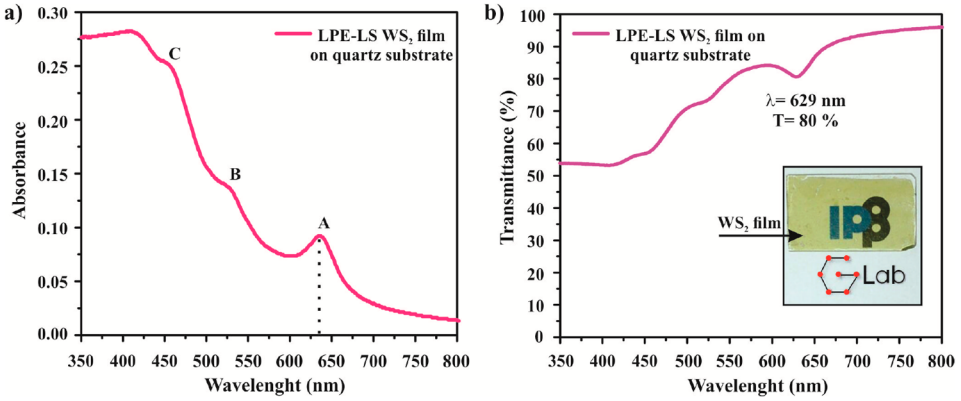

Figure 2. (a) Absorption and (b) transmission spectra for the thin LPE LS WS_2 film in the range from 350 to 800 nm. The inset in panel b illustrates the transparency and clarity of a single layer of the WS_2 film on the quartz substrate (1 × 2 cm) deposited by the LS method.

coated Si wafer, and quartz) using the homemade LS device. Further, they were left to dry for 30 min in ambient conditions. To ensure the removal of the residual solvent, the WS_2 films were annealed in a tube furnace in air for 20 min at a temperature of 120 °C.

Characterization of LPE LS WS_2 Films. The optical properties of LPE-LS WS_2 films on quartz were investigated using a UV−vis spectrophotometer (Beckman Coulter DU 720 UV−vis spectrophotometer). No more than 1% variation from the mean value existed over the entire film area, indicating LPE-LS WS_2 film uniformity on the scale of several square centimeters. Information about the morphology of WS_2 films was obtained using optical microscopy with a magnification of 400 times, and SEM (Tescan MIRA3 field-emission gun). All SEM images were taken at 20 kV. The topography of thin LPE-LS WS_2 films was characterized using a NTEGRA Prima atomic force microscope in non-contact mode. The thickness of the obtained LPE-LS WS_2 film was measured by non-contact optical profilometer ZYGO New View 7100. The gold-coated silicon wafer was chosen as a substrate as a result of its better light interference compared to the SiO_2/Si wafer. The thickness of the WS_2 film was estimated on the basis of five height profiles of film−substrate edges. The LPE-LS WS_2 film−substrate edge was made by a diamond pen. Raman spectra were measured with the Micro-Raman Tri Vista 557 triple spectrometer at room temperature (T = 23 °C) and humidity of 25%. To avoid the damage caused by heating, the power of the Nd:YAG laser (λ = 532 nm) was kept below 2 mW. The approximate size of the laser spot on the sample was 2 μm. An objective lens microscope with 50× magnifications was used. The measurements were performed on six different positions on the surface of each WS_2 film sample using an acquisition time of 300 s. The spectrum range was 200−3800 cm^{-1}. The measurements could not be performed below 200 cm^{-1}, considering the configuration of the experimental setup. XPS measurements have been performed at the custom-built NAP-XPS setup in the Notre Dame Radiation Laboratory (NDRL). The setup contained a reaction cell with a volume of ∼15 cm^3, which could sustain water vapor pressure up to 20 mbar.[37] Photoelectrons from the samples were collected and detected by the SPECS PHOIBOS 150 hemispherical analyzer, which was deferentially pumped. The base pressure of the system was of the order of 10^{-9}−10^{-10} mbar. The samples made of thin LPE-LS WS_2 films deposited on SiO_2/Si wafers were loaded first into the UHV chamber of the NAP-XPS setup and then introduced into the reaction cell. The pass energy of the analyzer was 20 eV for all high-resolution spectra. The energy of the spectrometer was calibrated to the gold standard sample. Considering the morphology of the thin films, we expected the presence of adventitious carbon (from air) in the form of CO or CO_2 species trapped on the surface and between the flakes in the film. To remove these and all other possible residual impurities (toluene and NMP), the LPE-LS WS_2 film was annealed at a temperature of 300 °C. After confirmation of the integrity and composition of the samples, pure water vapor was introduced into the reaction cell, within the pressure range corresponding to an approximately relative humidity (RH) between 4 and 22%.[38]

RESULTS AND DISCUSSION

The process of formation and controlled deposition of the WS_2 film is schematically illustrated in Figure 1. The continuous insertion of a small amount of WS_2 dispersion at the interface between two immiscible liquids, water and toluene, induces the self-assembly of WS_2 nanoflakes. The interfacial tension of the water/air system is approximately equal to the surface tension of water (∼73 mN/m at room temperature),[39] while the presence of toluene reduces it to 37.1 mN/m.[40] Driven by an overall reduction of the interfacial surface energy, WS_2 nanosheets form a large area of a densely packed thin film.

The successful formation of the WS_2 film at the liquid/liquid interface can be a consequence of the long-range dipolar repulsion of the particles as well as their attractive interaction.[41,42] The difference in dielectric constants of phases that create the interface, polar (water) and nonpolar (air and oil) substances, can create an asymmetric distribution of particles charging and the formation of the dipole moment.[41] The repulsive dipole−dipole interactions are responsible for

https://doi.org/10.1021/acs.langmuir.3c00107
Langmuir 2023, 39, 8055−8064

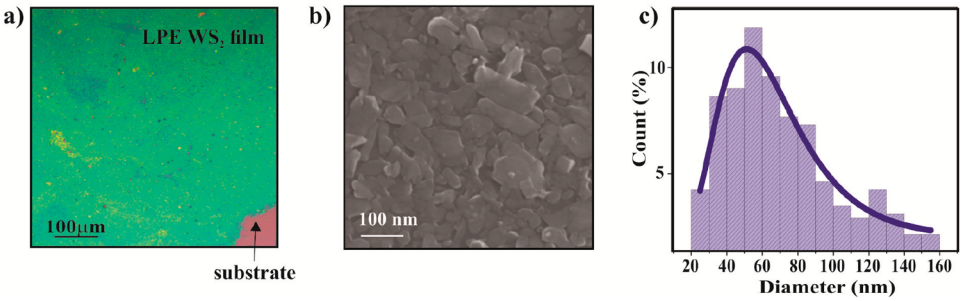

Figure 3. Images of the WS_2 film deposited on the SiO_2/Si substrate obtained by (a) optical microscopy, (b) SEM, and (c) histograms of the lateral size obtained from five 3 × 3 μm^2 SEM images (~1500 flakes). The distributions of the flake diameter have been fitted with a log-normal curve.

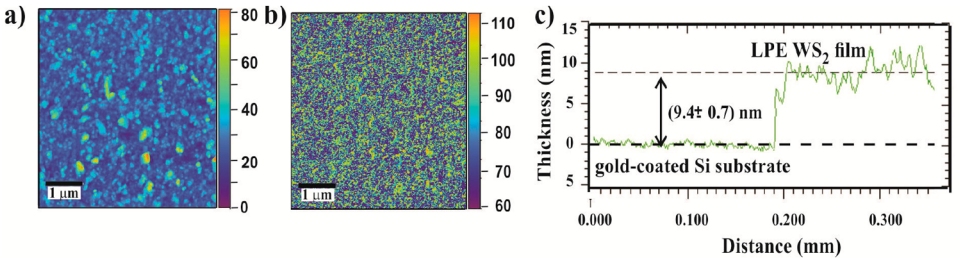

Figure 4. (a) AFM topographic image of the LPE-LS WS_2 film on the SiO_2/Si substrate (image includes a false color bar) of 5 × 5 μm^2, (b) phase image of the LPE-LS WS_2 thin film from the same area (image includes a false color bar) showing more contrast around the edges of the nanoflakes, and (c) height profile of the LPE-LS WS_2 film/Au-coated Si substrate performed by the optical profilometer (measurement started from the gold-coated Si substrate).

the ordering of the particles adsorbed at liquid interfaces.[41] Still, Nikolaides et al.[42] have shown that the dipolar electric field of particles causes electrical stress, inducing distortion of the liquid−liquid interface shape that results in the appearance of interparticle capillary attraction having a significant role in the stability of the particles at the liquid/liquid interface.[42] However, because the WS_2 nanoflakes can be described as rather flat-shaped than spherical, their stability and arrangement at the interface of two liquids may be more adequately explained by the free energy of their attachment/detachment over various contact angles at the interface of liquids.[30,43] Using an analysis developed by Binks and Horozov,[43] it has been shown that the attachment of the graphene and MoS_2 nanosheets at the liquid−liquid interface will be extremely energetically favorable if the energy of the detachment is maximized and the interfacial energy is minimized.[25,30] During the self-assembly, the highest stability of liquid-phase exfoliated WS_2 nanoflakes at the water/toluene interface is likely achieved by their parallel orientation to the interface. This spontaneous arrangement through the edge to edge contact of nanosheets and their overlapping enables the reduction of the interfacial area of liquids and the formation of tightly packed WS_2 films.[33,35] For further analysis and characterization, the LPE WS_2 films were deposited on solid substrates using the LS technique.

UV−Vis Characterization of LPE LS WS_2 Films. The optical characterization of LPE LS WS_2 films is represented in Figure 2. The absorption spectrum (Figure 2a) is characterized by three exciton peaks (A, ~629 nm; B, ~526 nm; and C, ~455 nm), confirming the 2H-semiconducting crystal structure of liquid-phase exfoliated WS_2 nanoflakes.[44] The average transparency for a single deposition of WS_2 film was 80 ± 1% at the wavelength of 629 nm (Figure 2b).

Morphology Characterization of LPE LS WS_2 Films. The morphology of LPE-LS WS_2 films is shown in Figure 3. The optical contrast between the SiO_2/Si substrate [$d(SiO_2) \approx$ 300 nm] and the film indicates complete coverage of the substrate and homogeneity of the film on the centimeter length scale (Figure 3a). In Figure 3b, the image taken by SEM provides more detailed information about the film structure. It can be noticed that the WS_2 nanoflakes collected by LS assembly form a well-packed array throughout their edge-to-edge contact. The overlapping of nanoflakes is also observed. The SEM image indicates that the water/toluene assembly technique can be used to obtain wrinkle-free WS_2 films with excellent nanosheet packing and uniformity, which cannot be achieved in a single-step spin-coating or drop-casting method.[12,34] This is in line with previous reports on the advantages of the LB and LS techniques of liquid-phase exfoliated 2D-materials compared to conventional deposition methods, such as drop casting, spray or spin coating, and vacuum filtration.[25,27,28,33−35] For example, the self-organization of graphene nanoflakes[27] at the interface enables their better mutual contact, in contrast to drop-casting, spin-coating, and vacuum-filtered techniques, where the presence of a large amount of NMP and its low volatility lead to the aggregation of graphene as a result of a longer drying time of the film. This impedes the control of the film thickness, which then affects both the transparency and the electrical properties of the film. The films produced through liquid/liquid assembly and transferred onto the substrate by LB/LS methods exhibit not only more uniform thickness but also a compact spatial arrangement, with the nanosheets aligned over a much larger area than can be achieved by spin or spray coating.[33] Similar conclusions apply to the MoS_2 thin films, where Neilson et al.[25] directly compare the characteristics of the LS MoS_2 film transferred from the liquid/liquid interface onto a solid substrate, with the MoS_2 film obtained by spray and spin deposition methods. On the basis of the measurement of the

https://doi.org/10.1021/acs.langmuir.3c00107
Langmuir 2023, 39, 8055−8064

flake diameter, the average lateral size of the WS_2 nanoflakes was estimated to be in the range of 60 ± 20 nm (Figure 3c).

In addition to the optical and electron microscopy, we performed the AFM topography scans of LPE-LS WS_2 films transferred on SiO_2/Si (panels a and b of Figure 4). The topography of thin LPE WS_2 films (Figure 4a) shows the existence of WS_2 nanosheets with different thicknesses and excellent surface coverage by layered overlapping WS_2 nanoflakes. The phase image (Figure 4b), which presents the phase shift in the cantilever oscillations, reflecting the combined material properties, such as stiffness, adhesion, viscosity, and dissipation, indicates good LPE-LS WS_2 film homogeneity and shows a better contrast around the nanoflake edges.

Optical profilometry measurements of the LPE-LS WS_2 film are shown in Figure 4c. On the basis of the height profiles of the film/substrate edge (Figure 4c), the thickness of the WS_2 films is estimated as 9.4 ± 0.7 nm.

Raman Spectroscopy of LPE LS WS_2 Films. For further characterization of the LPE-LS WS_2 thin film, Raman spectroscopy has been applied to verify the exfoliation of bulk WS_2 into few-layer WS_2 nanosheets. Figure 5 represents the Raman spectra of WS_2 thin films and their bulk as a reference.

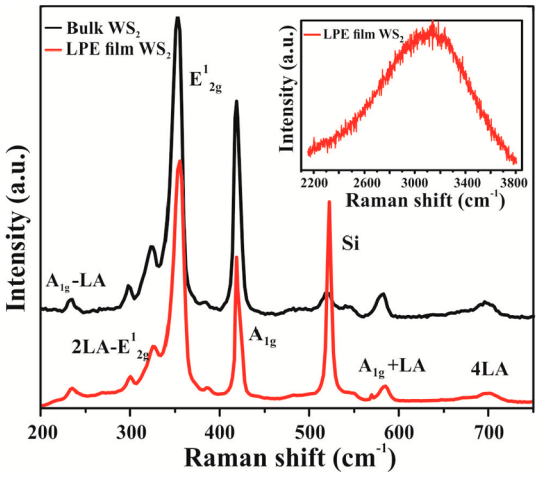

Figure 5. Raman spectra of WS_2 bulk materials and WS_2 thin films deposited on the SiO_2/Si wafer, with (inset) fluorescence in the Raman spectrum of the WS_2 thin film.

Because the laser wavelength (λ = 532 nm) corresponds to the exciton energy of WS_2 (the peak B at the absorption spectrum, Figure 2), the resulting spectra represent resonant Raman spectra.[45] Besides two characteristic Raman active first-order optical modes $A_{1g}(\Gamma)$ and $E^1_{2g}(\Gamma)$, the resonant Raman spectrum involves the longitudinal acoustic phonons at the M point of the Brillouin zone [LA(M)], overtones [2LA(M) and 4LA(M), second and fourth harmonics], and combination modes (A_{1g} − LA, 2LA − $2E^1_{2g}$, and A_{1g} + LA).[45,46] Under the resonance condition, the $E^1_{2g}(\Gamma)$ mode overlaps with the 2LA(M) mode.[46] LA(M) is positioned below 200 cm^{-1} (precisely at 176 cm^{-1} in the experiment of Berkdemir et al.[46]) and cannot be seen in spectra considering the range of our experimental setup, but the other vibrational bands are present in both spectra of thin-film WS_2 and the WS_2 bulk (Figure 5). It indicates that, during the exfoliation process, there was no interaction between the WS_2 nanosheets and the solvent molecules (NMP), which would lead to changes in the chemical composition of the material. In comparison to the Raman spectrum of the WS_2 bulk material, there are no significant changes in the Raman shift of the vibration modes: A_{1g} − LA (234 cm^{-1}), 2LA − $2E^1_{2g}$ (299 cm^{-1}), A_{1g} + LA (582 cm^{-1}), and 4LA (698 cm^{-1}). In the Raman spectra of the LPE LS WS_2 film, $A_{1g}(\Gamma)$ (418 cm^{-1}) and $E^1_{2g}(\Gamma)$ [+2LA(M)] (354 cm^{-1}) are red- and blue-shifted (for 2 cm^{-1}) compared to the WS_2 bulk, which is expected when the number of WS_2 layers is decreasing.[47] Changes in the electronic structure, formation of the direct energy gap, which is the characteristic of exfoliated WS_2, was confirmed by the presence of fluorescence in the Raman spectrum of the LPE-LS WS_2 thin film (inset spectrum in Figure 5).[48] The Raman spectra recorded in the range from 800 to 2200 cm^{-1} showed no vibrational modes (presented in section 3 of the Supporting Information).

The characterization of the LPE-LS WS_2 films produced at the toluene/water interface and transferred on solid substrates showed a high level of reproducibility in their physical and chemical properties. The transmittance, Raman spectra, and compactness of the films did not differ significantly between different samples (see sections 2−4 of the Supporting Information).

Effects of Water Molecules on the Surface of LPE-LS WS_2 Films. To obtain insight into the chemical composition and binding characteristics of the LPE-LS WS_2 films when they are exposed to water vapor, XPS analysis was performed. All represented core level photoemission spectra (W 4f, S 2p, O 1s, and C 1s) have been analyzed with a Gauss (30%)−Lorentz (70%) function defined in Casa XPS as GL (30) after a Shirley-type background subtraction. The C 1s peak at 284.8 eV was used for calibration of the binding energy scale. Panels a−c of Figure 6 depict the deconvoluted XPS spectra of the pristine LPE-LS WS_2 film. The W 4f core level spectrum (Figure 6a) is deconvoluted into six components: three W 4f doublet (W $4f_{7/2}$ and W $4f_{5/2}$). The doublet peaks arising as a result of spin−orbit splitting correspond to W^{4+} at 32.5 and 34.6 eV, W^{5+} at 35.5 and 37.8 eV, and W^{6+} at 36.7 and 38.7 eV binding energy. The XPS spectrum of sulfur is fitted into doublet S $2p_{3/2}$ and S $2p_{1/2}$ at 161.9 and 163.1 eV (Figure 6b). The two peaks of the S^{2-} and W^{4+} oxidation states are attributed, according to the literature, to the pure 2H-WS_2 phase.[49,50] Recent studies have reported that WS_2 films show poor stability and the tendency for spontaneous oxidation in the air environment at room or higher temperatures.[51−53] These results imply that, dependent upon the operating temperature range, WS_2 can be partially or totally converted into different forms: tungsten oxide (WO_3), non-stoichiometric tungsten oxide (WO_{3-x}), hydroxide and/or hydrate tungsten oxide ($WO_3 \cdot nH_2O$).[12,50,53,54] Considering the conditions of LPE-LS WS_2 film preparation (self-assembly of nanoflakes at the toluene/water interface and the annealing of films in air at 120 °C) and the value of the binding energies of W^{5+} and W^{6+}, the presence of these oxidation products in the LPE-LS WS_2 films can be expected. To complete the analysis, XPS of the O 1s core level was also performed in this study (Figure 6c). The broad O 1s spectrum observed in the range of 529−537 eV is deconvoluted into four components. The position of the peaks in the deconvoluted spectrum is tentative as a result of the large width of the O 1s peak and the overlapping of possible oxygen species with close values of binding energy. The assignment of these four peaks is based on

https://doi.org/10.1021/acs.langmuir.3c00107
Langmuir 2023, 39, 8055−8064

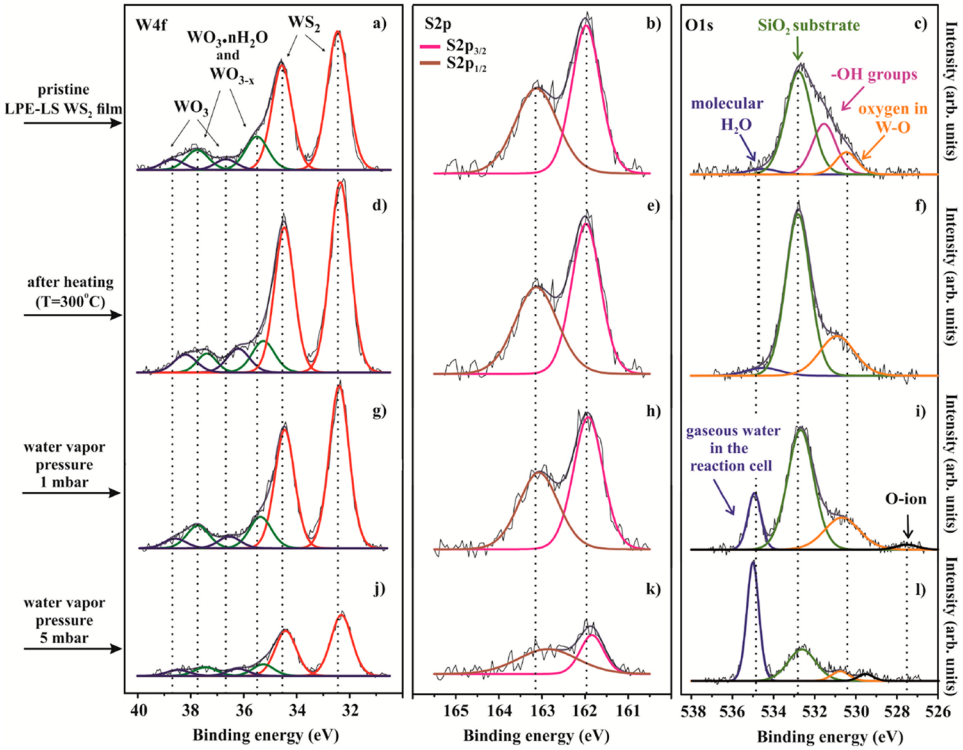

Figure 6. XPS W 4f, S 2p, and O 1s spectra of the LPE LS WS_2 film deposited on the SiO_2/Si substrate: (a–c) pristine, (d–f) after heating at T = 300 °C in vacuum, (g–i) exposure to 1 mbar water vapor, and (j–l) exposure to 5 mbar water vapor. The first column presents the W 4f spectrum with the three doublets attributed to WS_2 (red), WO_{3-x} and $WO_3 \cdot nH_2O$ (dark green), and WO_3 (dark blue). The second column shows a doublet of sulfur, S $2p_{3/2}$ (pink) and S $2p_{1/2}$ (brown). The third column represents the O 1s spectrum deconvoluted into components assigned to molecular H_2O from the water/toluene interface and gaseous water in the reaction cell (dark blue), SiO_2 (olive green), −OH groups (purple), and oxygen in $W-O_x$ (orange), with oxygen ions as nucleophilic oxygen (black line). The envelope curve for all spectra is marked as a dark gray line.

the literature and protocol for the creation and transfer of WS_2 films on solid substrates. The peak located at the lowest binding energy (530.3 eV) corresponds to oxygen ions (O^{2-}), confirming the formation of W−O bonds.[55] The existence of the hydroxyl group (−OH), assigned to the peak at 531.5 eV, indicates the hydration of tungsten/tungsten oxide.[56] The formation of the oxidation products consisting of oxide/hydroxide compounds of W and hydrate of WO_3 can be due to the presence of WS_2 film defects, as recently reported[57] that the liquid-phase exfoliation coupled with the LB technique produces self-assembled films with a high density of nanoflake edge defects. The edge defects of LPE-LS WS_2 nanoflakes/films, like tungsten dangling bonds, behave as active sites for the interaction with O_2, humidity from the atmosphere, and water present as a component of liquid/liquid interfaces.

The origin of the major peak in the O 1s spectrum, positioned at 532.8 eV, can be ascribed to the SiO_2 substrate and adsorption of O_2 molecules from the atmosphere.[58,59] In the previously reported studies[60,61] and database,[38] the peak presented at the highest binding energy in the O 1s spectrum is usually related to the chemisorbed/physisorbed H_2O molecules on the film surface. Thus, the highest binding energy peak (at 534.9 eV) in the observed spectrum refers to the adsorption of water molecules. These water molecules can be adsorbed on the WS_2 film surface or intercalated through its structure and trapped between the nanoflakes during the film formation.

As described earlier (Experimental Section), a small amount of NMP from the WS_2 dispersion is present during the self-assembly of WS_2 nanoflakes. This compound together with toluene may be detected in LPE-LS WS_2 films in the form of carbon. To assess the presence of carbon contamination from these solvents and other sources, including the interaction cell (adventitious carbon), we also recorded the high-resolution spectrum of C 1s (Figure S2 of the Supporting Information). Considering that, after the heating of LPE-LS WS_2 films at 120 °C in air, there was still residual water and solvents in the film (Figure 6c), the samples were additionally annealed in vacuum at 300 °C.

The XPS spectra of W 4f, S 2p, and O 1s for the post-annealed LPE-LS WS_2 film are shown in panels d–f of Figure 6. The position of the characteristic peaks (W 4f and S 2p) for pure 2H-WS_2 remained unchanged after heating of LPE-LS WS_2 films in high vacuum, suggesting that annealing does not affect the W−S chemical bonds (panels d and e of Figure 6). The S atoms are still bound exclusively to W without revealing additional chemical states or introducing new defects. However, it is worth noting that the binding energy of other peaks attributable to W with higher oxidation states in the W spectrum (Figure 6d) is downshifted for 0.5 eV. The significant chemical shift that refers to increasing of the binding energy for 0.6 eV is also remarked for the oxide ions O^{2-} (Figure 6f). The obtained results imply that changes in the W 4f and O 1s core level spectrum are probably caused by losing an oxygen atom in WO_3 during heat treatment of LPE LS WS_2 films in vacuum.[62] The creation of oxygen vacancies, as point defects, is usually accompanied by the reduction of W^{6+} to W^{5+} and the generation of WO_{3-x} compounds.[62] Released lattice oxygen atoms can leave the film and be evacuated from the chamber, but also their migration to filling the previously formed surface

https://doi.org/10.1021/acs.langmuir.3c00107
Langmuir 2023, 39, 8055−8064

oxygen vacancy defects, oxidation of WO_{3-x}, cannot be excluded. Furthermore, in the O 1s spectrum of post-annealed LPE-LS WS_2 films (Figure 6f), the OH peak entirely disappears, as evidence of film dehydration. The other two peaks ascribed to SiO_2 (at 532.8 eV) and H_2O (at 534.9 eV) molecules did not undergo any changes in terms of the chemical shift. The presence of the peak at 534.9 eV suggests that a complete desorption of water molecules from the LPE-LS WS_2 films did not occur. Considering the porous structure of the WS_2 films, it is likely that a certain amount of H_2O remains trapped within the film, with some of it also being chemisorbed and forming bridges between the nanoflakes.

After the sample WS_2 film was cooled to the room temperature, it was exposed to 1 and 5 mbar pressure of water vapor, which corresponds approximately to RH between 4 and 22% (panels g–l of Figure 6). The high-resolution XPS spectra show that the peak position of W 4f and S 2p doublets for pure 2H-WS_2 stay unchanged in both cases (panels g, h, j, and k of Figures 6). The existence of water molecules clearly does not influence the chemical bond of W–S, suggesting that the H_2O molecules are physisorbed onto the surface of the LPE-LS WS_2 films. After the increase of water vapor pressure in the chamber, multilayers of H_2O are formed through hydrogen bonds (Figure 6l). The chemical shift of the peak positioned at 534.9 eV as well as the peak corresponding to SiO_2 (at 532.7 eV) was not observed (panels i and l of Figure 6), which indicates that introduced water did not have access to the silicon wafer substrate; i.e., the homogeneous, full coverage of the WS_2 film on the surface has not been disrupted. The suppressed intensity and broadening of all peaks, except the peak at 534.9 eV (panels g–l of Figure 6), is due to the smaller number of photoelectrons reaching the detector in the presence of the water multilayer on the surface and free gaseous water molecules in the reaction cell.

The charge transfer in tungsten oxides, at 1 mbar, is evidenced by the shift (0.3 eV) of W^{5+} and W^{6+} peak positions toward the higher binding energy (Figure 6g) compared to those at the post-heating LPE-LS WS_2 films (Figure 6d). Also, the position of the peak corresponding to O^{2-} (Figure 6l) has undergone an alteration and downshift for 0.3 eV. The obtained results indicate the oxidation of W^{5+} to W^{6+}. Once the water vapor molecules come into contact with the surface of LPE-LS WS_2 films, the oxygen atoms will fill the previously formed point defects, oxygen vacancies in non-stoichiometric WO_{3-x}, forming WO_3, which is the opposite of the reduction of these compounds that occurs at post-annealed LPE-LS WS_2.[62] During the chemical bonding of oxygen with its adjacent tungsten atom, the transfer of electrons from W to the O atom has occurred and the electronic density near the tungsten atom decreases. In that case, the Coulomb interaction between the nucleus and the remaining electrons in the W atom becomes stronger. Thus, the binding energy of W peaks will be shifted to higher values, and for the O^{2-} peak, the binding energy will be shifted to lower values. In the O 1s spectrum shown in Figure 6i, the new peak has appeared at 527.5 eV and can be tentatively ascribed to the creation of hydrate tungsten oxide ($WO_3 \cdot nH_2O$)[63] or nucleophilic (atomic) oxygen.[64]

The introduction of water vapor at 5 mbar leads to W^{5+} and W^{6+} peak shift from 0.3 eV to lower binding energies (Figure 6j) and the large chemical shift by more than 2 eV of the O 1s peak, previously at 527.5 eV, to higher binding energies (Figure 6l). Such a shift has been previously observed in the adsorption of oxygen on Ag(110) and Ag(111) surfaces,[64] where atomic oxygen trapped in defects or different adsorption sites can have different ionic states and, therefore, different charges. In the case of the porous WS_2 film, the edge-rich structure offers a wide range of adsorption sites for oxygen, which can then be more weakly (ionic-like states) or more strongly (covalent bonds) bound to tungsten in the film. In the case of more covalently bound but not yet electrophilic, O 1s will still be lower than that which corresponds to WO_x but significantly higher than that in the nucleophilic form. An additional possibility for the appearance and binding energy shift of this O 1s peak could be that the chemical changes of the LPE-LS WS_2 film are caused by the formation of additional hydrides of tungsten oxides through the interaction of water molecules with defects (WO_3, and WO_{3-x}).[63] Considering the structure of our WS_2 films, it is plausible that both mechanisms are taking place during the exposure of LPE-LS WS_2 films to H_2O in a vacuum.

CONCLUSION

In this work, we presented the study of the water adsorption effect on WS_2 thin films obtained using the new toluene/water interfacial self-assembly technique from the liquid-phase exfoliated 2D material. In the first part, we characterized LPE-LS WS_2 films using various spectroscopic and microscopic techniques (UV–vis, Raman spectroscopy, SEM, and AFM). The toluene/water interfacial self-assembly technique and LS film deposition method provide a strong confinement of the WS_2 flakes. Using a small volume of the WS_2 dispersion allows the facile and rapid formation of theoretically unlimited large-area, highly transparent, and thin films of few-layer WS_2 nanosheets.

Chemical properties of the LPE-LS WS_2 films and their interaction with water molecules under near-ambient water vapor pressures reveal that defects in the WS_2 flakes play a major role in the chemical interaction of the water and LPE-LS WS_2 film surface. The presence of WO_3, WO_{3-x}, and hydrated tungsten oxide, in the freshly prepared LPE-LS WS_2 films, can be explained by the existence of the edge defects from tungsten dangling bonds that arose during the liquid-phase exfoliation of the WS_2 material. The temperature treatment of the LPE-LS WS_2 films in vacuum, performed before their exposure to water vapor, to remove the residual solvent, had a partial effect on their dehydration. This implies that the trapping of the H_2O molecules in the film structure and their chemisorptions represents the first stage of the water–WS_2 film interaction and an unavoidable event during the exposition of the film to the liquid water at the moment of its formation at the interface. Besides the expected significant physisorption of H_2O at the surface of LPE LS WS_2 films, during their exposure to H_2O gas at 1 and 5 mbar, oxygen-activated sites, such as WO_3 and WO_{3-x}, are the central places for the interaction with the water molecules from the gas phase. Except for the oxidation of W^{5+}, adsorption of intact and dissociated H_2O molecules is responsible for the formation of hydrated tungsten oxides.

The investigation of the interaction of water molecules with the surface of the thin 2D semiconductor WS_2 film is an imperative for fine tuning the sensing properties, regardless of the sensing target, because the presence of water in ambient conditions is unavoidable. Therefore, the characterization of molecular interactions between water molecules and the WS_2 film and the identification of specific chemical and physical bonds under near-ambient conditions are essential for further

https://doi.org/10.1021/acs.langmuir.3c00107
Langmuir 2023, 39, 8055–8064

use in sensing applications. These new data may be especially useful for improving the accuracy and responsiveness of various gas sensor devices operating in various environmental conditions, such as low or high humidity and high temperatures, or improving the sensitivity of biochemical sensors that usually deal with analytes in aqueous solution.

■ ASSOCIATED CONTENT

Supporting Information

The Supporting Information is available free of charge at https://pubs.acs.org/doi/10.1021/acs.langmuir.3c00107.

UV−vis spectroscopy used to determine the concentration of WS_2 dispersions, detailed AFM images of the LPE LS WS_2 film on a silicone substrate, Raman spectra recorded in the spectral range between 800 and 2200 cm^{-1}, transmittance for five thin LPE LS WS_2 films recorded in the range of 350−800 nm, and X-ray photoelectron spectra of the carbon C 1s state in the LPE LS WS_2 films deposited on the SiO_2/Si wafer (PDF)

■ AUTHOR INFORMATION

Corresponding Author

Radmila Panajotović − *Institute of Physics Belgrade, University of Belgrade, 11080 Belgrade, Serbia;* orcid.org/0000-0002-2174-0062; Email: radmila@ipb.ac.rs

Authors

Jasna Vujin − *Institute of Physics Belgrade, University of Belgrade, 11080 Belgrade, Serbia*

Weixin Huang − *Radiation Laboratory, University of Notre Dame, Notre Dame, Indiana 46556, United States*

Jovan Ciganović − *Department for Physical Chemistry, Institute of Nuclear Sciences Vinča, University of Belgrade, 11351 Belgrade, Serbia*

Sylwia Ptasinska − *Radiation Laboratory and Department for Physics and Astronomy, University of Notre Dame, Notre Dame, Indiana 46556, United States;* orcid.org/0000-0002-7550-8189

Complete contact information is available at: https://pubs.acs.org/10.1021/acs.langmuir.3c00107

Notes

The authors declare no competing financial interest.

■ ACKNOWLEDGMENTS

The authors acknowledge the funding provided by the Institute of Physics Belgrade, Institute of Nuclear Sciences Vinča (Grant 451-03-68/2022-14/200017), through the grant by the Ministry of Education, Science, and Technological Development of the Republic of Serbia. Weixin Huang and Sylwia Ptasinska acknowledge the U.S. Department of Energy, Office of Science, Office of Basic Energy Sciences, under Award DE-FC02-04ER15533 (NDRL 5372).

■ REFERENCES

(1) Davis, R. E.; McGregor, G. R.; Enfield, K. B. Humidity: A Review and Primer on Atmospheric Moisture and Human Health. *Environ. Res.* **2016**, *144*, 106−116.

(2) Sharma, A. K.; Kaur, B.; Popescu, V. A. On the Role of Different 2D Materials/Heterostructures in Fiber-Optic SPR Humidity Sensor in Visible Spectral Region. *Opt. Mater.* **2020**, *102*, 109824.

(3) Melios, C.; Giusca, C. E.; Panchal, V.; Kazakova, O. Water on Graphene: Review of Recent Progress. *2D Mater.* **2018**, *5* (2), 022001.

(4) He, P.; Brent, J. R.; Ding, H.; Yang, J.; Lewis, D. J.; O'Brien, P.; Derby, B. Fully Printed High Performance Humidity Sensors Based on Two-Dimensional Materials. *Nanoscale* **2018**, *10* (12), 5599−5606.

(5) Zhao, J.; Li, N.; Yu, H.; Wei, Z.; Liao, M.; Chen, P.; Wang, S.; Shi, D.; Sun, Q.; Zhang, G. Highly Sensitive MoS_2 Humidity Sensors Array for Noncontact Sensation. *Adv. Mater.* **2017**, *29* (34), 1702076.

(6) Chhowalla, M.; Shin, H. S.; Eda, G.; Li, L.-J.; Loh, K. P.; Zhang, H. The Chemistry of Two-Dimensional Layered Transition Metal Dichalcogenide Nanosheets. *Nat. Chem.* **2013**, *5* (4), 263−275.

(7) Li, A.; Zhang, J.; Qiu, J.; Zhao, Z.; Wang, C.; Zhao, C.; Liu, H. A Novel Aptameric Biosensor Based on the Self-Assembled DNA−WS_2 Nanosheet Architecture. *Talanta* **2017**, *163*, 78−84.

(8) Convertino, D.; Mishra, N.; Marchetti, L.; Calvello, M.; Viegi, A.; Cattaneo, A.; Fabbri, F.; Coletti, C. Effect of Chemical Vapor Deposition WS_2 on Viability and Differentiation of SH-SY5Y Cells. *Front. Neurosci.* **2020**, *14*, 592502.

(9) Yi, H.; Zhou, X.; Zhou, C.; Yang, Q.; Jia, N. Liquid Exfoliated Biocompatible WS_2 @BSA Nanosheets with Enhanced Theranostic Capacity. *Biomater. Sci.* **2021**, *9* (1), 148−156.

(10) Asres, G. A.; Baldoví, J. J.; Dombovari, A.; Järvinen, T.; Lorite, G. S.; Mohl, M.; Shchukarev, A.; Pérez Paz, A.; Xian, L.; Mikkola, J.-P.; Spetz, A. L.; Jantunen, H.; Rubio, Á.; Kordás, K. Ultrasensitive H_2S Gas Sensors Based on P-Type WS_2 Hybrid Materials. *Nano Res.* **2018**, *11* (8), 4215−4224.

(11) Järvinen, T.; Lorite, G. S.; Peräntie, J.; Toth, G.; Saarakkala, S.; Virtanen, V. K.; Kordas, K. WS_2 and MoS_2 Thin Film Gas Sensors with High Response to NH_3 in Air at Low Temperature. *Nanotechnology* **2019**, *30* (40), 405501.

(12) Paolucci, V.; Emamjomeh, S. M.; Nardone, M.; Ottaviano, L.; Cantalini, C. Two-Step Exfoliation of WS_2 for NO_2, H_2 and Humidity Sensing Applications. *Nanomaterials* **2019**, *9* (10), 1363.

(13) Kuru, C.; Choi, D.; Kargar, A.; Liu, C. H.; Yavuz, S.; Choi, C.; Jin, S.; Bandaru, P. R. High-Performance Flexible Hydrogen Sensor Made of WS_2 Nanosheet−Pd Nanoparticle Composite Film. *Nanotechnology* **2016**, *27* (19), 195501.

(14) Pawbake, A. S.; Waykar, R. G.; Late, D. J.; Jadkar, S. R. Highly Transparent Wafer-Scale Synthesis of Crystalline WS_2 Nanoparticle Thin Film for Photodetector and Humidity-Sensing Applications. *ACS Appl. Mater. Interfaces* **2016**, *8* (5), 3359−3365.

(15) Guo, H.; Lan, C.; Zhou, Z.; Sun, P.; Wei, D.; Li, C. Transparent, Flexible, and Stretchable WS_2 Based Humidity Sensors for Electronic Skin. *Nanoscale* **2017**, *9* (19), 6246−6253.

(16) Huo, N.; Yang, S.; Wei, Z.; Li, S.-S.; Xia, J.-B.; Li, J. Photoresponsive and Gas Sensing Field-Effect Transistors Based on Multilayer WS_2 Nanoflakes. *Sci. Rep.* **2014**, *4* (1), 5209.

(17) Jha, R. K.; Guha, P. K. Liquid Exfoliated Pristine WS_2 Nanosheets for Ultrasensitive and Highly Stable Chemiresistive Humidity Sensors. *Nanotechnology* **2016**, *27* (47), 475503.

(18) Leonardi, S. G.; Wlodarski, W.; Li, Y.; Donato, N.; Sofer, Z.; Pumera, M.; Neri, G. A Highly Sensitive Room Temperature Humidity Sensor Based on 2D-WS_2 Nanosheets. *FlatChem* **2018**, *9*, 21−26.

(19) Chen, Z.; Lu, C. Humidity Sensors: A Review of Materials and Mechanisms. *Sens. Lett.* **2005**, *3* (4), 274−295.

(20) Mao, S.; Chang, J.; Pu, H.; Lu, G.; He, Q.; Zhang, H.; Chen, J. Two-Dimensional Nanomaterial-Based Field-Effect Transistors for Chemical and Biological Sensing. *Chem. Soc. Rev.* **2017**, *46* (22), 6872−6904.

(21) Coleman, J. N.; Lotya, M.; O'Neill, A.; Bergin, S. D.; King, P. J.; Khan, U.; Young, K.; Gaucher, A.; De, S.; Smith, R. J.; Shvets, I. V.; Arora, S. K.; Stanton, G.; Kim, H.-Y.; Lee, K.; Kim, G. T.; Duesberg, G. S.; Hallam, T.; Boland, J. J.; Wang, J. J.; Donegan, J. F.; Grunlan, J. C.; Moriarty, G.; Shmeliov, A.; Nicholls, R. J.; Perkins, J. M.; Grieveson, E. M.; Theuwissen, K.; McComb, D. W.; Nellist, P. D.;

Nicolosi, V. Two-Dimensional Nanosheets Produced by Liquid Exfoliation of Layered Materials. *Science* **2011**, *331* (6017), 568−571.
(22) Backes, C.; Higgins, T. M.; Kelly, A.; Boland, C.; Harvey, A.; Hanlon, D.; Coleman, J. N. Guidelines for Exfoliation, Characterization and Processing of Layered Materials Produced by Liquid Exfoliation. *Chem. Mater.* **2017**, *29* (1), 243−255.
(23) Yao, Y.; Lin, Z.; Li, Z.; Song, X.; Moon, K.-S.; Wong, C. Large-Scale Production of Two-Dimensional Nanosheets. *J. Mater. Chem.* **2012**, *22* (27), 13494.
(24) Kymakis, E.; Stratakis, E.; Stylianakis, M. M.; Koudoumas, E.; Fotakis, C. Spin Coated Graphene Films as the Transparent Electrode in Organic Photovoltaic Devices. *Thin Solid Films* **2011**, *520* (4), 1238−1241.
(25) Neilson, J.; Avery, M. P.; Derby, B. Tiled Monolayer Films of 2D Molybdenum Disulfide Nanoflakes Assembled at Liquid/Liquid Interfaces. *ACS Appl. Mater. Interfaces* **2020**, *12* (22), 25125−25134.
(26) Zeng, X.; Hirwa, H.; Metel, S.; Nicolosi, V.; Wagner, V. Solution Processed Thin Film Transistor from Liquid Phase Exfoliated MoS_2 Flakes. *Solid-State Electron.* **2018**, *141*, 58−64.
(27) Kim, H.; Mattevi, C.; Kim, H. J.; Mittal, A.; Mkhoyan, K. A.; Riman, R. E.; Chhowalla, M. Optoelectronic Properties of Graphene Thin Films Deposited by a Langmuir−Blodgett Assembly. *Nanoscale* **2013**, *5* (24), 12365.
(28) Kaur, H.; Yadav, S.; Srivastava, A. K.; Singh, N.; Schneider, J. J.; Sinha, O. P.; Agrawal, V. V.; Srivastava, R. Large Area Fabrication of Semiconducting Phosphorene by Langmuir−Blodgett Assembly. *Sci. Rep.* **2016**, *6* (1), 34095.
(29) Andrić, S.; Tomašević-Ilić, T.; Bošković, M. V.; Sarajlić, M.; Vasiljević-Radović, D.; Smiljanić, M. M.; Spasenović, M. Ultrafast Humidity Sensor Based on Liquid Phase Exfoliated Graphene. *Nanotechnology* **2021**, *32* (2), 025505.
(30) Biswas, S.; Drzal, L. T. A Novel Approach to Create a Highly Ordered Monolayer Film of Graphene Nanosheets at the Liquid−Liquid Interface. *Nano Lett.* **2009**, *9* (1), 167−172.
(31) Woltornist, S. J.; Oyer, A. J.; Carrillo, J.-M. Y.; Dobrynin, A. V.; Adamson, D. H. Conductive Thin Films of Pristine Graphene by Solvent Interface Trapping. *ACS Nano* **2013**, *7* (8), 7062−7066.
(32) Salvatierra, R. V.; Souza, V. H. R.; Matos, C. F.; Oliveira, M. M.; Zarbin, A. J. G. Graphene Chemically Synthesized from Benzene at Liquid−Liquid Interfaces. *Carbon* **2015**, *93*, 924−932.
(33) Yu, X.; Prévot, M. S.; Guijarro, N.; Sivula, K. Self-Assembled 2D WSe_2 Thin Films for Photoelectrochemical Hydrogen Production. *Nat. Commun.* **2015**, *6* (1), 7596.
(34) Adilbekova, B.; Lin, Y.; Yengel, E.; Faber, H.; Harrison, G.; Firdaus, Y.; El-Labban, A.; Anjum, D. H.; Tung, V.; Anthopoulos, T. D. Liquid Phase Exfoliation of MoS_2 and WS_2 in Aqueous Ammonia and Their Application in Highly Efficient Organic Solar Cells. *J. Mater. Chem. C* **2020**, *8* (15), 5259−5264.
(35) Clark, R. M.; Berean, K. J.; Carey, B. J.; Pillai, N.; Daeneke, T.; Cole, I. S.; Latham, K.; Kalantar-zadeh, K. Patterned Films from Exfoliated Two-Dimensional Transition Metal Dichalcogenides Assembled at a Liquid−Liquid Interface. *J. Mater. Chem. C* **2017**, *5* (28), 6937−6944.
(36) Pešić, J.; Vujin, J.; Tomašević-Ilić, T.; Spasenović, M.; Gajić, R. DFT Study of Optical Properties of MoS_2 and WS_2 Compared to Spectroscopic Results on Liquid Phase Exfoliated Nanoflakes. *Opt. Quantum Electron.* **2018**, *50* (7), 291.
(37) Zhang, X.; Ptasinska, S. Dissociative Adsorption of Water on an H_2O/GaAs(100) Interface: In Situ near-Ambient Pressure XPS Studies. *J. Phys. Chem. C* **2014**, *118* (8), 4259−4266.
(38) National Institute of Standards and Technology (NIST). *NIST X-ray Photoelectron Spectroscopy Database, NIST Standard Reference Database Number 20*; NIST: Gaithersburg MD, 2000; DOI: 10.18434/T4T88K, https://srdata.nist.gov/xps/citation.aspx.
(39) Vargaftik, N. B.; Volkov, B. N.; Voljak, L. D. International Tables of the Surface Tension of Water. *J. Phys. Chem. Ref. Data* **1983**, *12*, 817−820.
(40) Saien, J.; Akbari, S. Interfacial Tension of Toluene + Water + Sodium Dodecyl Sulfate from (20 to 50) °C and pH between 4 and 9. *J. Chem. Eng. Data* **2006**, *51* (5), 1832−1835.
(41) Pieranski, P. Two-Dimensional Interfacial Colloidal Crystals. *Phys. Rev. Lett.* **1980**, *45* (7), 569−572.
(42) Nikolaides, M. G.; Bausch, A. R.; Hsu, M. F.; Dinsmore, A. D.; Brenner, M. P.; Gay, C.; Weitz, D. A. Electric-Field-Induced Capillary Attraction between like-Charged Particles at Liquid Interfaces. *Nature* **2002**, *420* (6913), 299−301.
(43) Binks, B. P.; Horozov, T. S. Colloidal Particles at Liquid Interfaces: An Introduction. *Colloidal Particles at Liquid Interfaces*; Cambridge University Press: Cambridge, U.K., 2006; Chapter 1, pp 1−74, DOI: 10.1017/CBO9780511536670.002.
(44) Pagona, G.; Bittencourt, C.; Arenal, R.; Tagmatarchis, N. Exfoliated Semiconducting Pure 2H-MoS_2 and 2H-WS_2 Assisted by Chlorosulfonic Acid. *Chem. Commun.* **2015**, *51* (65), 12950−12953.
(45) Zhao, W.; Ghorannevis, Z.; Amara, K. K.; Pang, J. R.; Toh, M.; Zhang, X.; Kloc, C.; Tan, P. H.; Eda, G. Lattice Dynamics in Mono- and Few-Layer Sheets of WS_2 and WSe_2. *Nanoscale* **2013**, *5* (20), 9677.
(46) Berkdemir, A.; Gutiérrez, H. R.; Botello-Méndez, A. R.; Perea-López, N.; Elías, A. L.; Chia, C.-I.; Wang, B.; Crespi, V. H.; López-Urías, F.; Charlier, J.-C.; Terrones, H.; Terrones, M. Identification of Individual and Few Layers of WS_2 Using Raman Spectroscopy. *Sci. Rep.* **2013**, *3* (1), 1755.
(47) Lee, C.; Yan, H.; Brus, L. E.; Heinz, T. F.; Hone, J.; Ryu, S. Anomalous Lattice Vibrations of Single- and Few-Layer MoS_2. *ACS Nano* **2010**, *4* (5), 2695−2700.
(48) Qiao, S.; Yang, H.; Bai, Z.; Peng, G.; Zhang, X. Identifying the Number of WS_2 Layers via Raman and Photoluminescence Spectrum. *Proceedings of the 2017 5th International Conference on Mechatronics, Materials, Chemistry and Computer Engineering (ICMMCCE 2017)*; Chongqing, China, July 24−25, 2017; DOI: 10.2991/icmmcce-17.2017.247.
(49) Kosmala, T.; Palczynski, P.; Amati, M.; Gregoratti, L.; Sezen, H.; Mattevi, C.; Agnoli, S.; Granozzi, G. Strain Induced Phase Transition of WS_2 by Local Dewetting of Au/Mica Film upon Annealing. *Surfaces* **2021**, *4* (1), 1−8.
(50) Zhou, P.; Xu, Q.; Li, H.; Wang, Y.; Yan, B.; Zhou, Y.; Chen, J.; Zhang, J.; Wang, K. Fabrication of Two-Dimensional Lateral Heterostructures of WS_2/WO_3·H_2O through Selective Oxidation of Monolayer WS_2. *Angew. Chem., Int. Ed.* **2015**, *54* (50), 15226−15230.
(51) Gao, J.; Li, B.; Tan, J.; Chow, P.; Lu, T.-M.; Koratkar, N. Aging of Transition Metal Dichalcogenide Monolayers. *ACS Nano* **2016**, *10* (2), 2628−2635.
(52) Rong, Y.; He, K.; Pacios, M.; Robertson, A. W.; Bhaskaran, H.; Warner, J. H. Controlled Preferential Oxidation of Grain Boundaries in Monolayer Tungsten Disulfide for Direct Optical Imaging. *ACS Nano* **2015**, *9* (4), 3695−3703.
(53) Perrozzi, F.; Emamjomeh, S. M.; Paolucci, V.; Taglieri, G.; Ottaviano, L.; Cantalini, C. Thermal Stability of WS_2 Flakes and Gas Sensing Properties of WS_2/WO_3 Composite to H_2, NH_3 and NO_2. *Sens. Actuators, B* **2017**, *243* (2), 812−822.
(54) Liu, Q.; Wang, F.; Lin, H.; Xie, Y.; Tong, N.; Lin, J.; Zhang, X.; Zhang, Z.; Wang, X. Surface Oxygen Vacancy and Defect Engineering of WO_3 for Improved Visible Light Photocatalytic Performance. *Catal. Sci. Technol.* **2018**, *8* (17), 4399−4406.
(55) Dupin, J.-C.; Gonbeau, D.; Vinatier, P.; Levasseur, A. Systematic XPS Studies of Metal Oxides, Hydroxides and Peroxides. *Phys. Chem. Chem. Phys.* **2000**, *2* (6), 1319−1324.
(56) Warren, A.; Nylund, A.; Olefjord, I. Oxidation of Tungsten and Tungsten Carbide in Dry and Humid Atmospheres. *Int. J. Refract. Met. Hard Mater.* **1996**, *14* (5−6), 345−353.
(57) Tomašević-Ilić, T.; Jovanović, Đ.; Popov, I.; Fandan, R.; Pedrós, J.; Spasenović, M.; Gajić, R. Reducing Sheet Resistance of Self-Assembled Transparent Graphene Films by Defect Patching and Doping with UV/Ozone Treatment. *Appl. Surf. Sci.* **2018**, *458*, 446−453.

(58) Chow, P. K.; Singh, E.; Viana, B. C.; Gao, J.; Luo, J.; Li, J.; Lin, Z.; Elías, A. L.; Shi, Y.; Wang, Z.; Terrones, M.; Koratkar, N. Wetting of Mono and Few-Layered WS_2 and MoS_2 Films Supported on Si/SiO_2 Substrates. *ACS Nano* **2015**, *9* (3), 3023−3031.
(59) Huang, G.; Liu, H.; Wang, S.; Yang, X.; Liu, B.; Chen, H.; Xu, M. Hierarchical Architecture of WS_2 Nanosheets on Graphene Frameworks with Enhanced Electrochemical Properties for Lithium Storage and Hydrogen Evolution. *J. Mater. Chem. A* **2015**, *3* (47), 24128−24138.
(60) Han, G.-F.; Li, F.; Zou, W.; Karamad, M.; Jeon, J.-P.; Kim, S.-W.; Kim, S.-J.; Bu, Y.; Fu, Z.; Lu, Y.; Siahrostami, S.; Baek, J.-B. Building and Identifying Highly Active Oxygenated Groups in Carbon Materials for Oxygen Reduction to H_2O_2. *Nat. Commun.* **2020**, *11* (1), 2209.
(61) Kerber, S. J.; Bruckner, J. J.; Wozniak, K.; Seal, S.; Hardcastle, S.; Barr, T. L. The Nature of Hydrogen in X-ray Photoelectron Spectroscopy: General Patterns from Hydroxides to Hydrogen Bonding. *J. Vac. Sci. Technol., A* **1996**, *14* (3), 1314−1320.
(62) Universitaria, C.; Jardines, C.; Manuel, D. S. Structural Properties of WO_3 Dependent of the Annealing Temperature Deposited by Hot-Filament Metal Oxide Deposition. *Rev. Mex. Fis.* **2012**, *58* (6), 504−509.
(63) Albanese, E.; Di Valentin, C.; Pacchioni, G. H_2O Adsorption on WO_3 and WO_{3-x} (001) Surfaces. *ACS Appl. Mater. Interfaces* **2017**, *9* (27), 23212−23221.
(64) Jones, T. E.; Rocha, T. C. R.; Knop-Gericke, A.; Stampfl, C.; Schlögl, R.; Piccinin, S. Insights into the Electronic Structure of the Oxygen Species Active in Alkene Epoxidation on Silver. *ACS Catal.* **2015**, *5* (10), 5846−5850.

https://doi.org/10.1021/acs.langmuir.3c00107
Langmuir 2023, 39, 8055−8064

Experimental and theoretical cross sections for elastic electron scattering from zinc

B. P. Marinković, R. Panajotović, and D. Šević
Institute of Physics Belgrade, University of Belgrade, Pregrevica 118, 11080 Belgrade, Serbia

R. P. McEachran
Plasma Research Laboratories, Research School of Physics and Engineering, Australian National University, Canberra, ACT 0200, Australia

G. García
Instituto de Física Fundamental, CSIC, Serrano 113-bis, E-28006 Madrid, Spain

F. Blanco
Departamento de Estructura de la Materia, Física Térmica y Electrónica, Universidad Complutense de Madrid, Avenida Complutense, E-28040 Madrid, Spain

M. J. Brunger*
College of Science and Engineering, Flinders University, G.P.O. Box 2100, Adelaide, South Australia 5001, Australia

(Received 11 March 2019; published 10 June 2019)

We report on experimental elastic differential and integral cross sections for electron scattering from zinc. The energy range of these measurements is 10–100 eV, while the scattered electron angular range in the differential cross-section data is 10°–150°. We also supplement our measured data with applications of our optical potential and relativistic optical potential approaches to this problem. Where possible, the present results are compared against those from earlier B-spline R-matrix [O. Zatsarinny and K. Bartschat, Phys. Rev. A **71**, 022716 (2005)] and convergent close coupling [D. V. Fursa, I. Bray, R. Panajotović, D. Šević, V. Pejčev, D. M. Filipović, and B. P. Marinković, Phys. Rev. A **72**, 012706 (2005)] computations. Good overall qualitative accord is typically observed.

DOI: 10.1103/PhysRevA.99.062702

I. INTRODUCTION

There appear to be two main reasons for why studies of electron-zinc (Zn) scattering processes are important. The first is fundamental, in that Zn represents a quasi-two-electron atom for which a target description of a [core]ns^2 configuration has been previously quite successful in describing scattering phenomena from similar targets such as helium [1], beryllium [2], and magnesium [3]. As a consequence, testing this representation on a heavier atom, where relativistic effects might be important, is a valid rationale for its study. The second reason is applied, and largely stems from the work of Born [4,5], who suggested that Zn might be an attractive replacement for mercury in making high-pressure gas discharge lamps more environmentally friendly. More recently, studies on the emission dynamics of an expanding ultrafast laser-produced Zn plasma have been reported [6,7]. In the latter of those studies, Gupta *et al.* [7] detailed a collisional radiative model, using relativistic distorted wave (RDW) cross-section calculation results, in order to interpret the data of Smijesh and Philip. [6]. That collisional radiative model included the RDW elastic integral cross section (ICS), as well as the ICSs for discrete inelastic processes, to ensure that the sum of their individual ICSs was consistent with the total cross section and therefore that their [7] cross-section data base was self-consistent. As a consequence of the Born [4,5] work, White *et al.* [8] conducted an initial multiterm simulation study looking at the transport characteristics of a swarm of electrons drifting through a background Zn vapor under the influence of an external electric field. That work of White *et al.* [8] demonstrated that anisotropic scattering, through incorporation of the elastic momentum transfer cross section [8] of Zn, was necessary for accurately describing the electron transport characteristics in Zn under the influence of such an applied (external) electric field.

Previous studies into electron-zinc scattering, particularly in regard to measurements, have been somewhat limited. Experimental excitation cross sections, for the $4\,^1P$ and $5\,^1P$ states in Zn, have been reported by Williams and Bozinis [9], Panajotović *et al.* [10], and Fursa *et al.* [11]. Measurements of coherence and correlation parameters for the $4\,^1P$ state have also been published by Piwiński *et al.* [12]. To the best of our knowledge, only a limited study of elastic cross sections for scattering from the $4\,^1S$ state of Zn is available in the literature [9] and improving that situation thus forms an important rationale for the current investigation. Having said that, we do also note two early conference papers from Trajmar and Williams

*Corresponding author: michael.brunger@flinders.edu.au

[13] and Predojević *et al.* [14]. The situation with respect to theory is a little better, with earlier elastic computations from Childs and Massey [15], McGarrah *et al.* [16], and Kumar *et al.* [17] being noted. As those earlier computations have been largely superseded, we do not discuss them further. More recently, a R-matrix result (incorporating 23 target states) [8], a B-spline R-matrix (BSR) approach [18] (incorporating 49 target states), and a convergent close-coupling (CCC) method [11] (incorporating 206 target states) have become available in the literature. While the CCC results were only reported in Fursa *et al.* [11] for the $4\,^1P$ and $5\,^1P$ states, elastic results were also obtained as a part of that computation. Nonetheless, with an eye to ultimately formulating a recommended database for electron-Zn scattering [19], further calculations in the form of our optical potential (OP) and relativistic optical potential (ROP) methods have been undertaken here. Broadening of the available theoretical results was thus another important rationale for the present paper.

It is well known in the electron-scattering community that the pioneering electron-metal vapor measurements, made at the Jet Propulsion Laboratory (JPL) from the early 1970's to the early 1980's, for both elastic and discrete inelastic processes, have not stood the test of time and are inaccurate. This has been confirmed by both independent measurements from other groups and by theory, with examples for sodium [20], magnesium [21–23], and lead [24], to name but a few systems, being given here in support of our assertion. The review of Bartschat [25] might also be consulted. Therefore, a further rationale of the present paper was to explicitly check this for elastic scattering in zinc [9] and, just as importantly, to extend the available cross-section data to energies beyond 40 eV, which is presently the only energy available in the literature. This is crucial for providing a serious benchmark to test theory against.

The atomic, molecular, and optical physics scattering community has, for some time now, been endeavoring to compile accurate and complete cross-section data bases [26] for scattering systems relevant to simulating charged-particle behavior in, for example, electron swarm systems [27–29] and radiation damage in matter [30–32], and for understanding the role of electron-driven processes in planetary atmospheres [33,34]. The importance of elastic-scattering cross sections, which do not deposit energy in the background medium or excite states leading to photon emission that can be analyzed for diagnostic purposes [35], has probably been somewhat undervalued by that community. In fact, by allowing for anisotropy in electron swarm transport through the momentum transfer cross section [27–29] and, through the elastic differential cross sections (DCSs) [30–32], looking at the dispersion of the electrons as they travel through the body, the elastic-scattering process is crucial for a quantitative description of those phenomena. This forms a further allied rationale for this paper.

The remainder of this paper is structured as follows. In the next section we present a brief discussion of our experimental apparatus and methods, while in Sec. III details of our OP and ROP calculations are provided. Our results and a discussion of those results are given in Sec. IV, with some conclusions from the present investigation thereafter being drawn.

II. EXPERIMENTAL DETAILS

The apparatus is the same as that used in our earlier inelastic electron-Zn measurements [10,11], so that only a brief description is needed here. It consists of a conventional crossed-beam spectrometer, with hemispherical energy selectors in both the monochromator and analyzer. Note that both these selectors were fabricated from molybdenum. The electron beam was transported and focused by a series of cylindrical-symmetry lenses, that were made of gold-plated oxygen-free high thermal conductivity copper. A "zoom" lens was situated at the exit of the monochromator, in order to provide a stable focus at the interaction region for the electron energy range of interest to this paper, specifically, for incident electron energies between 10 and 100 eV. Note that the incident electron-beam current was in the range 1–10 nA for the present experiments, as measured using a standard Faraday cup configuration, while the current energy resolution was ∼40-meV full width at half maximum (FWHM).

In all crossed-beam scattering experiments it is crucial to minimize the value of the Earth's magnetic field in the system, and particularly at the interaction region. This is to ensure that the paraxial focusing properties of the incident and scattered electron beams are maintained. In this case the residual magnetic field in the interaction region was measured to be less than 0.1 μT, with this being achieved by utilizing double μ-metal shielding.

The energy scale was calibrated by measuring the position of the well-known [36,37] $(4s4p^2)\,^2D$ resonance in the elastic channel, located at 4.25 eV [37]. Due, at least in part, to the asymmetry of this feature, we estimate the uncertainty on this calibration to be $\sim \pm 300$ meV. The position of the true zero-scattering angle was determined before each angular distribution measurement, by checking the symmetry of the scattered electron signal at positive and negative angles with respect to the unscattered electrons. The uncertainty in the angular scale was $\pm 0.5^\circ$, while the overall angular resolution of the present experimental configuration was 1.5° (FWHM). Note that the analyzer could be rotated from -30° to $+150^\circ$ with respect to the primary electron beam.

The atomic zinc beam, formed from ultrapure zinc granules, was produced using a resistively heated oven made of titanium. The oven nozzle aspect ratio was 0.075, a small enough value that should assist in minimizing any possible effective-path-length correction factor effects on the measured angular distributions even for a single-tube capillary such as here [38,39]. Nonetheless, when required, the appropriate effective path-length correction factor for our scattering geometry, from Brinkman and Trajmar [38], was employed. Monitoring of the temperature at both the top and bottom of the crucible was necessary in order to provide stable conditions for the target Zn beam. A higher temperature at the top of the crucible ensured the nozzle did not clog, while a somewhat lower, but constant, temperature (∼670 K) at the bottom provided the effusive flow of the atomic beam. The corresponding metal vapor pressure was approximately 10 Pa, while the background pressure in the chamber was better than 5 mPa.

Irrespective of the incident electron energy ($E_0 = 10$, 15, 20, 25, 40, 60, 80, or 100 eV), our elastic angular distribution measurements were only undertaken when stable

TABLE I. Present measured $4\,^1S$(EL)/$4\,^1P$(4P) ratios at 10° and 20° scattering angles and for energies between 10 and 100 eV. Also shown are the relevant $4\,^1P$ DCSs from [10,11] and our corresponding OP and ROP theory results. Note that EL denotes the elastic channel.

Scattering angle / DCS	20°					10°			
	10 eV	15 eV	20 eV	25 eV	40 eV	40 eV	60 eV	80 eV	100 eV
4P [10,11] (10^{-16} cm^2/sr)	2.1	2.64	2.52	1.92	0.644	13.7	6.69	5.92	3.61
EL/4P experiment	8.3 ± 1.9	3.5 ± 0.5	2.15 ± 0.25	1.77 ± 0.42	1.8 ± 0.7	0.76 ± 0.16	0.58 ± 0.07	0.86 ± 0.10	1.06 ± 0.07
EL experiment (10^{-16} cm^2/sr)	17.4 ± 5.9	9.24 ± 2.09	5.41 ± 1.21	3.40 ± 0.99	1.15 ± 0.52	10.5 ± 4.7	3.88 ± 1.11	5.07 ± 1.48	3.82 ± 1.04
EL OP (10^{-16} cm^2/sr)	10.8	7.81	5.74	4.31	2.39	10.8	9.41	8.82	8.42
EL ROP (10^{-16} cm^2/sr)	15.3	10.2	6.93	4.87	2.07	14.3	10.8	8.92	7.82

electron-beam and zinc-beam operating conditions were achieved. The angular distributions for elastic scattering, i.e., when the energy loss of the incident beam after scattering was equal to 0 eV, at each energy, were measured by recording the number of true elastic-scattering events as a function of the scattered electron angle. Note that background electron scattering from the residual gas in our scattering chamber was carefully monitored, and was found to be very small across most of the scattered electron angular range of this investigation. Further note that those relative angular distribution data were corrected for the effective path-length factor [38] before normalization. Due to interference from the primary electron beam, in practice the minimum scattered electron angle that we could access was $\theta = 20°$ for $E_0 \leqslant 25$ eV and $\theta = 10°$ for 40 eV $\leqslant E_0 \leqslant 100$ eV. On the other hand, the maximum scattered electron angle we could measure, at all energies studied, was $\theta = 150°$. In this case the restriction was caused by the physical size of the monochromator and analyzer and their associated electron-optic lens elements. The present angular distributions, again at each energy, were subsequently placed on an absolute scale, from energy-loss measurements that encompassed the elastic ($4\,^1S$) and inelastic ($4\,^1P$) peaks at certain specific normalization angles. From the ratio of the elastic to inelastic intensities, in the energy-loss spectrum, at the normalization angle, and a knowledge of the absolute $4\,^1P$ DCSs from Fursa *et al.* [11], our angular distribution measurement at the given energy could now be placed on an absolute scale. Examples for this approach, at scattered electron angles of 10° and 20° and for all our incident electron energies between 10 and 100 eV, are given in Table I. Also included in this table are the relevant $4\,^1P$ DCSs from [10,11] and our corresponding OP and ROP theoretical results (see later).

The only concern with this approach, particularly at the lower incident electron energies, is the behavior of the analyzer transmission as a function of the scattered electron energy. This follows as the energy gap between the $4\,^1S$ and $4\,^1P$ states is ∼5.8 eV [18], so that for a 15-eV incident electron the outgoing scattered electron energies will vary from 15 eV ($4\,^1S$ state) to 9.2 eV ($4\,^1P$ state) across our energy-loss spectrum. However, our analyzer electron optics were specifically designed to cope with such situations so that we believe our transmission function is uniform to better than 23% at 10 eV and 7% at 100 eV.

An alternative approach, at each energy, that we employed here was to measure energy-loss spectra at each scattered electron angle and, in the manner just discussed, determine the elastic DCS directly from those energy-loss spectra. The beauty here is that the effective path-length correction factor cancels out in taking the ratio, and is thus of no concern with that approach. However, the analyzer transmission function issue (as just discussed) remains open. In any event, the elastic DCSs we determined from these two approaches, irrespective of the incident electron energy, were always consistent to within the uncertainties we cite. This gives us some confidence in the efficacy of our experimental measurement techniques and procedures. A summary of the present measured elastic DCSs and their uncertainties is given in Table II, with plots of those results and our new OP and ROP computations being found in Figs. 1 and 2. Having obtained our elastic DCSs, we now wish to extrapolate them to 0° and 180°, perform an interpolation, and then undertake the usual integration in order to derive elastic ICSs at each energy. To accomplish this in the least subjective manner possible, we applied the complex phase-shift analysis approach originally developed by Allen and coworkers [40,41]. Full details of this method can be found in [40,41], but essentially the user inputs the relevant beam energy and the dipole polarizability of zinc ($38.8\,a_0^3$ [42] in this case), the number of complex phase shifts (e.g., *s*, *p*, and *d* waves) to be varied in order to minimize the difference between the measured and simulated DCSs, and finally the maximum value of the partial waves to be employed in the Born expansion that accounts for the higher-order partial waves. In all cases the functional form of Allen and coworkers [40,41] produced an excellent representation of the measured DCSs, so that we are confident in the validity of the ICSs we have derived from this approach. The present experimental and theoretical elastic ICSs can be found in Table III and Fig. 3. The uncertainties on our measured DCSs stem from several contributions. The stabilities of the electron and atomic beams are both better than 2% over the lifetime of a given experimental run. Despite the large dynamic range of the elastic intensity over the scattered electron angles we probed (see Table II), the statistical uncertainties in our angular distributions were rarely worse than 30% and only then at the higher scattering angles. To place the angular distributions on

TABLE II. Experimental differential cross sections and absolute uncertainties (in parentheses) in units of 10^{-16} cm^2/sr for elastic electron scattering from the ground state of zinc. Uncertainties are at the one standard deviation level.

Angle	10 eV	15 eV	20 eV	25 eV	40 eV	60 eV	80 eV	100 eV
10					10.5(4.7)	3.88(1.11)	5.07(1.48)	3.82(1.04)
15	19.5(9.9)		11.1(2.5)	8.46(2.48)	3.61(1.62)			
20	17.4(5.9)	9.24(2.09)	5.41(1.21)	3.40(0.99)	1.15(0.52)	0.606(0.190)	0.646(0.210)	0.532(0.157)
25			2.46(0.55)	1.35(0.40)	0.343(0.154)			
30	6.02(2.03)	2.41(0.54)	1.05(0.24)	0.530(0.155)	0.096(0.043)	0.065(0.025)	0.074(0.030)	0.090(0.031)
35			0.447(0.099)	0.198(0.058)	0.020(0.009)			
38					0.0075(0.0035)			
40	2.05(0.69)	0.618(0.140)	0.184(0.041)	0.055(0.017)	0.0087(0.0040)	0.031(0.014)	0.064(0.027)	0.056(0.020)
45		0.261(0.059)	0.067(0.015)	0.0071(0.0025)	0.026(0.012)			
48				0.0037(0.0013)				
50	0.668(0.226)	0.106(0.024)	0.011(0.003)	0.0045(0.0016)	0.047(0.021)	0.056(0.023)	0.092(0.037)	0.064(0.023)
55	0.365(0.124)	0.043(0.010)	0.0053(0.0013)	0.020(0.006)	0.059(0.026)			
60	0.163(0.056)	0.016(0.004)	0.011(0.002)	0.034(0.010)	0.062(0.028)	0.071(0.028)	0.075(0.031)	0.044(0.017)
65	0.074(0.026)	0.0063(0.0017)	0.017(0.004)	0.043(0.013)	0.060(0.027)			
70	0.029(0.011)	0.0040(0.0013)	0.023(0.005)	0.044(0.013)	0.050(0.022)	0.022(0.010)	0.026(0.012)	0.019(0.008)
75		0.0040(0.0012)	0.026(0.006)	0.038(0.012)				
80	0.011(0.005)	0.0060(0.0017)	0.026(0.006)	0.031(0.009)	0.024(0.011)	0.015(0.008)	0.0061(0.0032)	0.0052(0.0025)
85	0.018(0.007)	0.0082(0.0022)	0.027(0.005)	0.026(0.008)				
90	0.031(0.011)	0.0099(0.0026)	0.020(0.005)	0.019(0.006)	0.0093(0.0043)	0.0066(0.0039)	0.0094(0.0046)	0.0070(0.0032)
95			0.017(0.004)	0.013(0.004)				
100	0.055(0.020)	0.017(0.004)	0.015(0.003)	0.0088(0.0029)	0.0062(0.0029)	0.018(0.009)	0.023(0.010)	0.016(0.007)
105			0.012(0.003)	0.0058(0.0020)				
110	0.090(0.031)	0.026(0.006)	0.014(0.003)	0.0047(0.0016)	0.0089(0.0041)	0.024(0.011)	0.031(0.013)	0.025(0.010)
115			0.017(0.004)	0.0070(0.0023)				
120	0.112(0.039)	0.041(0.010)	0.022(0.005)	0.0092(0.0029)	0.012(0.006)	0.027(0.012)	0.042(0.017)	0.023(0.010)
125			0.031(0.007)	0.013(0.004)				
130	0.148(0.051)	0.064(0.015)	0.043(0.010)	0.019(0.006)	0.011(0.005)	0.025(0.011)	0.023(0.010)	0.013(0.006)
135			0.060(0.013)	0.030(0.009)				
140	0.184(0.063)	0.095(0.022)	0.082(0.018)	0.043(0.013)	0.016(0.007)	0.010(0.006)	0.0070(0.0035)	0.0062(0.0028)
145			0.110(0.025)	0.061(0.018)				
150	0.253(0.086)	0.143(0.033)	0.145(0.032)	0.085(0.025)	0.035(0.016)	0.0077(0.0043)	0.0032(0.0019)	0.0013(0.0008)

an absolute scale, we carry over the intrinsic uncertainty on the 4 ^1P DCS at the normalization angle, the uncertainty in our effective path-length correction factor (<5%), the uncertainty of ∼10% in our energy and angular calibrations, and the uncertainty of 23% at 10 eV decreasing to 7% at 100 eV on our analyzer transmission function associated with the energy-loss measurements and our determination of the elastic to inelastic ratios. When combining all these contributions in quadrature, we found that the overall uncertainties on our elastic DCSs lay in the range ∼22–62%, with the exact uncertainties being found in Table II. For our elastic ICSs we estimate their uncertainties to be a conservative ±35%.

TABLE III. Present elastic ICS ($\times 10^{-16}$ cm^2), as derived from our measured DCS, for electron scattering from Zn. Estimated uncertainties in our data are ±35%, and are at the one standard deviation level. Note that our overall estimated uncertainty includes an "extrapolation uncertainty" due to the application of our phase-shift analysis approach [40,41].

E_0 (eV)	ICS (10^{-16} cm^2)	Absolute error (10^{-16} cm^2)
10	19.22	6.73
15	13.30	4.65
20	8.61	3.01
25	6.82	2.39
40	4.27	1.49
60	2.23	0.78
80	3.28	1.15
100	2.63	0.92

III. THEORETICAL METHODS

As already mentioned above we have employed two different theoretical approaches to calculate the elastic differential and integral cross sections of this investigation. These are now briefly detailed below.

A. OP approximation

We have recently described, in some detail, our optical potential approach as applied to the electron-beryllium [2] and electron-magnesium [3] scattering systems. All the generic details of our atomic OP method, that we gave in these papers, are equally applicable here and so as a consequence we do not repeat them. Rather, we simply highlight that when our OP method was benchmarked against a sophisticated BSR calculation [43], for elastic electron scattering from iodine,

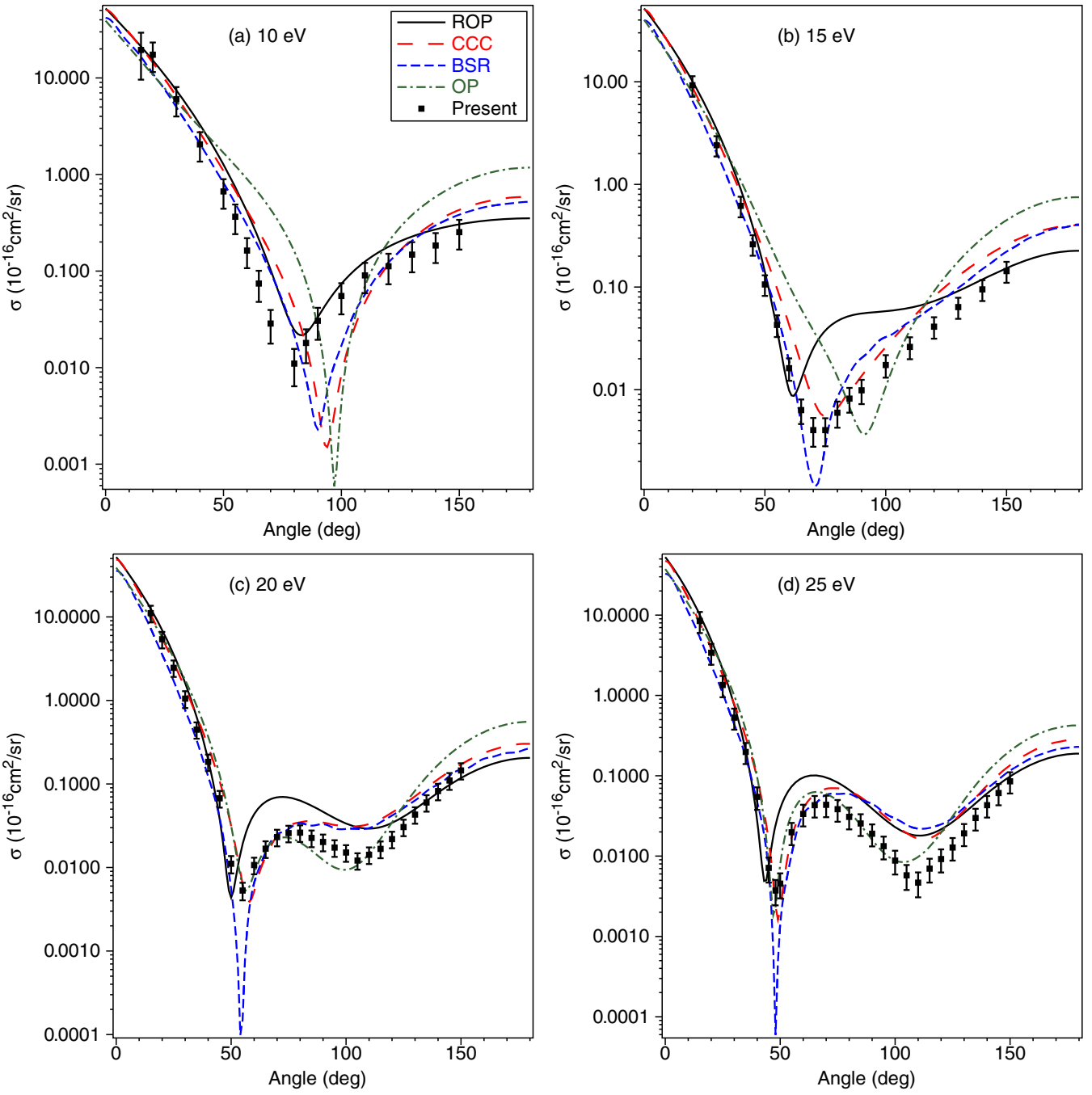

FIG. 1. Differential elastic cross sections ($\times 10^{-16}$ cm^2/sr) for electron scattering from zinc at (a) 10 eV, (b) 15 eV, (c) 20 eV, and (d) 25 eV. The present measurements (■) and OP (– · – · –) and ROP (——) calculations are compared against earlier CCC (– –) [11] and BSR (- - - -) [18] theory results. See also the inset.

very good agreement was found between them. We therefore anticipate that it will provide a good description for the elastic-scattering process in Zn as well.

B. ROP theory

We also gave a detailed synopsis of our relativistic optical potential calculations in [2,3], so we do not repeat them again now. In this case, however, there are some details pertaining specifically to the relativistic optical potential employed for Zn, which we now provide. In this paper the elastic and absorption cross sections were calculated using a complex relativistic optical potential (ROP) method in a similar manner, as just noted, to that outlined in the recent papers [2,3] for Be and Mg. A complete description of the ROP method is given in [44]; this paper will be referred to as paper I hereafter.

The ROP method is based upon the solution of the Dirac scattering equations which contain both static and polarization potentials, the exchange terms, and a nonlocal absorption potential to account for excitation and ionization processes. The ground- and excited-state wave functions of zinc were determined in a single configuration calculation using the

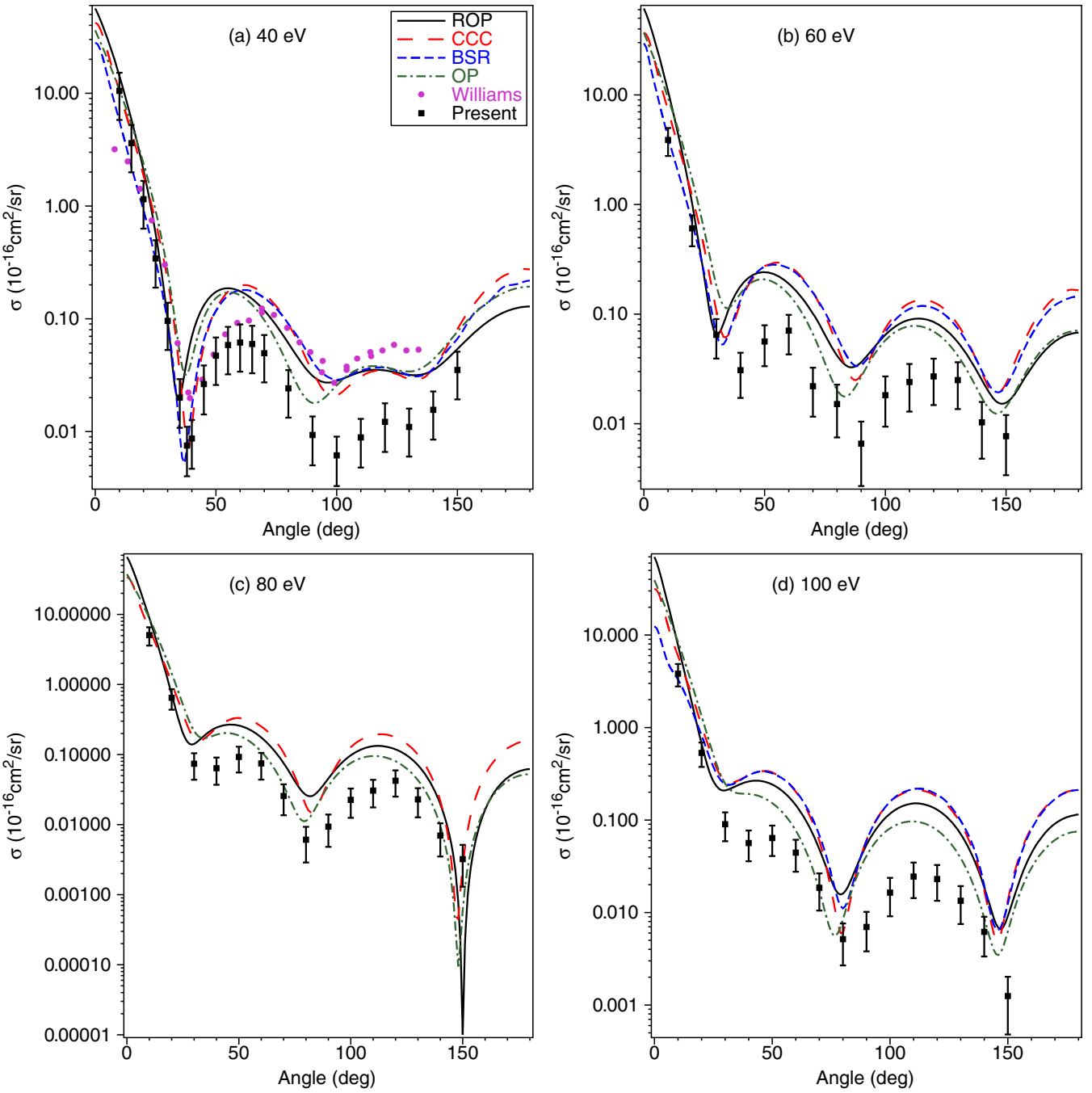

FIG. 2. Differential elastic cross sections ($\times 10^{-16}$ cm^2/sr) for electron scattering from zinc at (a) 40 eV, (b) 60 eV, (c) 80 eV, and (d) 100 eV. The present measurements (■) and OP (– · – · –) and ROP (——) calculations are compared against earlier CCC (– –) [11] and BSR (- - - -) [18] theory results. Also plotted is the measurement of Williams and Bozinis (●) [9] at 40 eV. See also the inset.

multiconfiguration Dirac-Fock program of Grant *et al.* [45]. The static potential was determined in the usual manner from the ground-state Dirac-Fock orbitals of zinc, while the nonlocal exchange interaction was included by antisymmetrizing the total scattering wave function. The polarization potential was determined by the polarized-orbital method of McEachran *et al.* [46,47] and included the first seven multipole potentials plus the corresponding dynamic polarization potential [48]. Thus, asymptotically the polarization potential contained all terms up to and including those corresponding to r^{-14}.

The nonlocal absorption potential was determined as an expansion over the inelastic channels of the target atom. These inelastic channels include both excitation of the higher-lying bound states as well as the single ionization of the target as given by Eq. (21b) of paper I. Also included were those channels which correspond to the ionization of $3p$ and $3d$ electrons at approximately 17 and 75 eV, respectively. For the excited bound states of zinc, which were used in the absorption potential, we included those eight states where one of the electrons in the outer $3s$ valence shell was excited to a higher-lying $np^{1,3}P$ state with $n = 4$ to 7 inclusive.

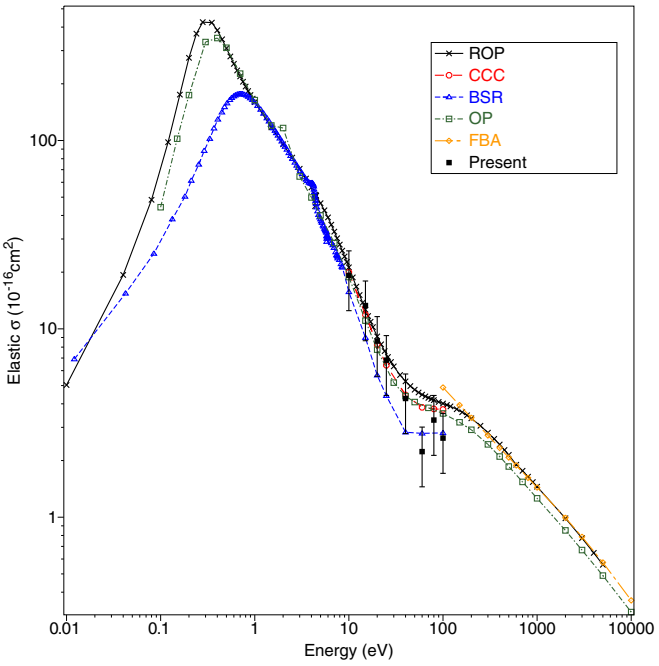

FIG. 3. Integral elastic cross sections ($\times 10^{-16}$ cm^2) for electron scattering from zinc. The present measurements (■) and OP (□) and ROP (×) calculations are compared against earlier CCC (○) [11], BSR (△) [18], and FBA (◇) [51] theory results. See also the inset.

For the case of ionization, we included those continuum states which correspond to an orbital angular momentum of zero to four; this gives rise to up to 71 ionization channels depending on the total angular momentum of the incident electron.

All the present OP and ROP results are converged and so have an intrinsic uncertainty of less than 1%. However, in terms of their ability to accurately reproduce benchmarked data or sophisticated CCC and BSR results, our experience [2,3,43] suggests an uncertainty of ∼10% for energies above about 1 eV and an uncertainty of up to ∼50% for energies below 1 eV. That larger uncertainty at those lower energies is due to the existence of the low-energy resonance (see Fig. 3), which can only be approximately represented in the OP and ROP methods. For these optical potential methods to compete with results from CC methods here, we would need to include the excited states involved in the resonance, in momentum space, and treat it as we do the ground state. The large basis sets in the BSR and CCC methods should give a good representation of both states involved in the resonance, as well as give a good representation of the polarization interaction. Therefore, large basis set BSR and/or CCC calculations, if available, should be preferred below ∼0.5 eV.

IV. RESULTS AND DISCUSSION

In Table II and Figs. 1 and 2 we show the results from our experimental differential cross-section measurements for elastic scattering from the $4\,^1S$ ground state of Zn. Also shown in Figs. 1 and 2 are the results from our present optical potential and relativistic optical potential DCS computations, and the earlier theoretical CCC and BSR calculations. As noted by Bartschat [49], the BSR results of Zatsarinny and Bartschat [18] focused on the lower-energy scattering phenomena. As a consequence, at higher energies some convergence problems (recall this is only a 49-state calculation) might be anticipated to be encountered. This is indeed the case; several of the higher-energy BSR elastic differential cross sections exhibit unphysical (although subtle) oscillations in their angular distributions. All the experimental and theoretical angular distributions exhibit a strong forward peaking (i.e., at smaller scattering angles) in their absolute elastic cross-section magnitudes (see Figs. 1 and 2) with this degree of forward peaking increasing as the incident electron energy increases. This behavior is consistent with the important role that zinc's strong dipole polarizability [42] plays in the scattering dynamics of this collisional system. Also of general note is that the number of local minima in the DCSs increases as the incident electron energy increases. Specifically, at 10 and 15 eV we observe one local cross-section minimum, while at 20 and 25 eV there are two local minima in the DCS and for energies of 40 eV and above there are three local minima. In this case the oscillatory behavior in the angular distributions, both experimental and theoretical, is physical and reflects the interference between the various phase shifts that describe elastic scattering in this system at a given energy. It is worthy of note that the positions of these minima in the angular distributions, although not necessarily their depths, are probably best described by the CCC and our OP theories (again see Figs. 1 and 2). Finally, in a general sense, we note that electron exchange also plays an important role, particularly at the lower energies, in this system. The best way to ascertain this is to "turn off" exchange in our computations, and to observe the effect that this unphysical action has on the calculated DCS (not explicitly shown in Figs. 1 and 2). As just noted, that effect was important at the lower energies of this paper.

Considering Fig. 1(a) in more detail we see that the present ROP result probably best describes the measured data, in terms of the shape, magnitude, and angular position of the DCS minimum. Nonetheless, it is fair to note that all the computations at least qualitatively reproduce the gross features of this elastic DCS. At 15 eV, however, the situation has changed a little with the CCC result [11] now best representing the measured DCS [see Fig. 1(b)]. However, we would again characterize the level of accord between the available theories and our data as being fair overall. By 20 eV [see Fig. 1(c)] best agreement between the measured data and theory is probably afforded by our OP result, although both the CCC [11] and ROP theories also do reasonable jobs in reproducing the qualitative features of this elastic DCS. Only the BSR computation [18], which predicts a far deeper cross-section minimum than any of the other theories or experiments at this energy, has significant problems here. This may reflect some issues with their convergence, as Bartschat noted [49], and indeed if we look closely at Fig. 1(c) we can see some small (unphysical) oscillations in their [18] angular distribution. A similar story to that just outlined at 20 eV can be found in Fig. 1(d) for 25 eV. Hence we do not consider that energy further.

At 40 eV, in Fig. 2(a), there is an earlier elastic DCS measurement from Williams and Bozinis [9] available in

the literature. When we compare that result to the present measurements we find, to within their stated uncertainties, very good agreement between them for scattered electron angles less than about 70°. Above 70°, however, the data of Williams and Bozinis [9] are significantly higher in magnitude than the present DCS, and in better accord with all the theory results. As noted previously, electron-metal vapor measurements made at JPL from the early 1970's to the early 1980's are now known to be inaccurate. Hence our observations regarding the level of agreement between our 40-eV measurements and those of Williams and Bozinis [9], in Fig. 2(a), are not particularly surprising, but were important to confirm. Figure 2(a) also indicates that it is the CCC result [11] that is probably in best overall agreement with our measured DCS, although our OP calculation also does a fair job in qualitatively reproducing the features of the 40-eV angular distribution. Once again, we find some suggestion of convergence problems with the BSR computation [18,49]. In Fig. 2(b) we present our 60-eV results. At this energy all the theories well reproduce the angular structure in this elastic DCS, although in terms of the cross-section magnitude for scattering angles greater than about 30° they are all much stronger in magnitude than our measured data. A similar story to that just outlined for 60 eV is also found at 80 eV [Fig. 2(c)] and 100 eV [Fig. 2(d)]. Indeed it is fair to say that for incident electron energies greater than 25 eV all the DCSs found in various theories are larger in magnitude than our measured results at middle and backward scattered electron angles. This observation is not new to us, having been seen in all our recent electron-molecule scattering studies [50]. In essence it is indicative of the "flux competition" between the open elastic, discrete inelastic, and ionization channels at a given incident electron energy. Assuming our measured DCSs are in fact correct, then Figs. 1(d) and 2(a)–2(d) suggest that more flux is going into the elastic channel, compared to the discrete inelastic and ionization channels, than should be the case. However, it is worth noting that the DCSs at all these energies have magnitudes that are very small at middle and backward electron-scattering energies. Therefore it would only require a very small misapportionment of the flux into the elastic channel to lead to what we find in Figs. 1(d) and 2(a)– 2(d). This highlights just how challenging these computations are, so that the level of accord that we achieve between theory and experiment in Figs. 1 and 2 is actually pretty good.

In Table III and Fig. 3 we present our derived elastic ICS for electron scattering from zinc. Also plotted in Fig. 3 are the results of our OP and ROP calculations, and corresponding CCC [11] and BSR [9] elastic ICSs. Additionally, a first Born approximation (FBA) level [26,51] calculation is also plotted in Fig. 3. The first point we can glean from Fig. 3 is the existence of a strong low-energy *p*-wave resonance feature in the elastic ICS, which is predicted by both our OP and ROP computations and the earlier BSR [18] calculation. This resonance was first observed experimentally in the electron transmission spectra (ETS) work of Burrow *et al.* [36], at an energy of 0.49 eV, with it being originally found in a semiempirical calculation by Zollweg [52] although at a slightly higher energy of 0.67 eV. The present OP calculation predicts the resonance peak at 0.4 eV, in good accord with that of Burrow *et al.* [36], while our ROP finds the peak to be in the range 0.28–0.35 eV, which is still in fair accord with the ETS result. The 49-state BSR calculation places the peak at 0.71 eV, in better accord with the semiempirical result of Zollweg [52]. It is well known that close-coupling-type calculations, when predicting the position and peak magnitudes of these low-energy resonance features, are very sensitive to the number of channels incorporated into their computation [53]. Therefore it would be desirable if a larger basis BSR calculation were to be performed on this system. Similarly, it would be very interesting to see the CCC results [11] for incident electron energies below 10 eV and extending down to about 0.01 eV. At this stage it appears that more work needs to be done in this low-energy regime (0.01–1 eV), in order to get a better handle on the true peak energy and magnitude of this cross section. Above 1 eV, however, the situation is clearer. As can be seen in Fig. 3, for energies between 1 and 10 eV the present OP and ROP elastic ICSs are in quite good accord with the BSR result [18]. Above 10 eV, the BSR cross section becomes lower in magnitude than all of the OP, ROP, and CCC results. This observation we believe, at least in part, reflects some of the convergence issues with the BSR calculation, at the higher energies, that we discussed previously. The OP and CCC results, between 10 and 100 eV, are in excellent agreement with one another, while our ROP result, which is a little higher in magnitude in that energy range, possibly due to it incorporating relativistic effects which neither the OP or CCC computations can account for, nonetheless remains in fair accord with the OP and CCC cross sections. Finally, for energies greater than 100 eV, we note the elastic ICSs from our OP and ROP calculations and the FBA calculation [51] all exhibit the same energy dependence and are in fair accord in terms of their magnitude. It would thus be relatively easy to construct a recommended data base in that energy range by simply taking an average of the OP, ROP, and FBA ICSs.

The other major highlight in Fig. 3 is the comparison between our derived elastic ICS and the available theories, including our own, between 10 and 100 eV. Here we find a very good level of agreement between the experimental ICSs and the theoretical results from the OP, ROP, and CCC calculations, for incident electron energies between 10 and 40 eV. While this might appear a little counterintuitive, given our previous discussions of the DCSs at those energies, it can be understood as follows. Most of the contribution to the integrand of the ICSs, even allowing for the $\sin\theta$ weighting factor, comes from the more forward electron-scattering angles of the DCSs and this is precisely where, between 10 and 40 eV, the experimental DCSs are in good accord, in the main, with those corresponding OP, ROP, and CCC computations. At higher energies (60–100 eV), however, the measured (derived) ICSs are lower in magnitude than the OP, ROP, and CCC results (see Fig. 3), and in better accord with the BSR calculated ICS. Given our previous discussion in relation to some possible convergence problems with the BSR at higher energies, that agreement between our experimental ICS and the BSR ICS must be considered to be a little serendipitous. Again, this ICS behavior at higher energies fully reflects the higher-energy DCS results (see Fig. 2). Specifically, the forward angle DCSs at those energies (except in part at 80 eV) are all a little lower in magnitude than the OP, ROP, and CCC cross sections

with this observation then being carried through, as one would expect, to the ICS level results (see Fig. 3).

V. CONCLUSIONS

We have reported on original differential cross-section measurements for elastic electron scattering from zinc. The energy range of those experiments was 10–100 eV, with the scattered electron angular range being 10°–150°. From those data we employed our phase-shift analysis procedure to derive corresponding integral cross sections. In addition, theoretical results from our optical potential and relativistic optical potential computations were also reported. On the basis of the work of McEachran and Stauffer [54] and Bartsch *et al.* [55], with polarized electrons, we had anticipated relativistic effects in Zn (Z=30) to be modest but nonetheless observable. Unfortunately, perhaps due to the slightly different representations of polarization, exchange, and the absorption interaction between our OP and ROP formalisms, no such effects were quantified in this investigation. This suggests that for a target even with Z=30 it may be too light to elucidate relativistic effects with unpolarized electrons. Where possible the present DCS and ICS experimental and theoretical data were compared against those from earlier CCC and BSR calculations. At the DCS level we found good qualitative accord between our measurements and the available calculations, although at the higher (40–100 eV) incident electron energies the theories tended to be systematically higher in magnitude than our measured results at middle and backward angles. This we believe was due to a small misapportionment of flux in the theory between the elastic channel and the discrete inelastic and ionization channels (i.e., flux competition). In particular, the results embodied in Figs. 1 and 2 indicate just how difficult it is for theory to describe a scattering process where the cross sections vary by four to five orders of magnitude over the scattered electron angular range from 0° to 180°, the treatment of the continuum by theory being somewhat problematic in that endeavour. Nonetheless, it would be both interesting and instructive if the BSR and CCC methods were to reprise their calculations with the larger basis sets they now routinely employ with the computational power now available to them. Agreement at the elastic integral cross-section level, between theory and our measurements, was quite good across the common energy range. At lower energy ($\leqslant$ 40 eV), to within our stated uncertainties, the experimental ICSs were largely consistent with the CCC, BSR, OP, and ROP computations, while at higher energies, although there is a degree of good fortune here due to their convergence problems at these higher energies, the BSR cross sections are in best accord with our experimental data. While a large basis BSR calculation and an extension of the existing CCC result to lower energies ($\sim$0.01 eV) would be desirable, to better define the magnitude and peak energy of the p-wave resonance cross section, we nonetheless believe a plausible (recommended) elastic ICS could now be established for this scattering system and for ultimate use in simulating electron transport in gaseous zinc.

ACKNOWLEDGMENTS

This work was financially supported, in part, by the Spanish Ministerio de Ciencia, Innovacion y Universidades (Project No. FIS2016-80440), the Australian Research Council (Projects No. DP160102787 and No. DP180101655), and the Ministry of Education, Science, and Technological Development (Project No. OI171020) of the Republic of Serbia. We thank Dr. L. Campbell for his help with some aspects of this paper, and we acknowledge helpful conversations with Prof. K. Bartschat. Finally, we also thank Dr. O. Zatsarinny and Prof. K. Bartschat for providing us tables of their BSR data and Prof. I. Bray and Prof. D. Fursa for the CCC data.

[1] D. V. Fursa and I. Bray, J. Phys. B **30**, 757 (1997).
[2] R. P. McEachran, F. Blanco, G. García, and M. J. Brunger, J. Phys. Chem. Ref. Data **47**, 033103 (2018).
[3] R. P. McEachran, F. Blanco, G. García, P. W. Stokes, R. D. White, and M. J. Brunger, J. Phys. Chem. Ref. Data **47**, 043104 (2018).
[4] M. Born, J. Phys. D **34**, 909 (2001).
[5] M. Born, Plasma Sources Sci. Technol. **11**, A55 (2002).
[6] N. Smijesh and R. Philip, J. Appl. Phys. **114**, 093301 (2013).
[7] S. Gupta, R. K. Gangwar, and R. Srivastava, Proceedings of the International Conference on Atomic Processes in Plasmas Conference, 2019 (unpublished); (private communication).
[8] R. D. White, R. P. McEachran, R. E. Robson, M. T. Elford, and K. Bartschat, J. Phys. D **37**, 3185 (2004).
[9] W. Williams and D. Bozinis, Phys. Rev. A **12**, 57 (1975).
[10] R. Panajotović, D. Šević, V. Pejčev, D. M. Filipović, and B. P. Marinković, Int. J. Mass Spectrom. **233**, 253 (2004).
[11] D. V. Fursa, I. Bray, R. Panajotović, D. Šević, V. Pejčev, D. M. Filipović, and B. P. Marinković, Phys. Rev. A **72**, 012706 (2005).
[12] M. Piwiński, Ł. Kłosowski, D. Dziczek, S. Chwirot, T. Das, R. Srivastava, A. D. Stauffer, C. J. Bostock, D. V. Fursa, and I. Bray, Phys. Rev. A **86**, 052706 (2012).
[13] S. Trajmar and W. Williams, Proceedings of the Eighth Symposium on the Physics of Ionized Gases, 1976 (unpublished), p. 199.
[14] B. Predojević, D. Šević, R. Panajotović, V. Pejčev, D. M. Filipović, and B. P. Marinković, Proceedings of the 20th Symposium on the Physics of Ionized Gases, 2000 (unpublished), p. 35.
[15] E. C. Childs and H. S. W. Massey, Proc. R. Soc. A **142**, 509 (1933).
[16] D. B. McGarrah, A. J. Antolak, and W. Williamson, J. Appl. Phys. **69**, 6812 (1991).
[17] P. Kumar, A. K. Jain, A. N. Tripathi, and S. N. Nahar, Phys. Rev. A **49**, 899 (1994).
[18] O. Zatsarinny and K. Bartschat, Phys. Rev. A **71**, 022716 (2005).
[19] L. C. Pitchford, L. L. Alves, K. Bartschat, S. F. Biagi, M.-C. Bordage, I. Bray, C. E. Brion, M. J. Brunger,

L. Campbell *et al.*, Plasma Process. Polym. **14**, 1600098 (2017).
[20] P. J. O. Teubner, J. L. Riley, M. J. Brunger, and S. J. Buckman, J. Phys. B **19**, 3313 (1986).
[21] M. J. Brunger, J. L. Riley, R. E. Scholten, and P. J. O. Teubner, J. Phys. B **21**, 1639 (1988).
[22] D. O. Brown, D. Cvejanović, and A. Crowe, J. Phys. B **36**, 3411 (2003).
[23] B. Predojević, V. Pejčev, D. M. Filipović, D. Šević, and B. P. Marinković, J. Phys. B **40**, 1853 (2007).
[24] S. D. Tošić, M. S. Rabasović, D. Šević, V. Pejčev, D. M. Filipović, L. Sharma, A. N. Tripathi, R. S. Srivastava, and B. P. Marinković, Phys. Rev. A **77**, 012725 (2008).
[25] K. Bartschat, Phys. Rept. **180**, 1 (1989).
[26] H. Tanaka, M. J. Brunger, L. Campbell, H. Kato, M. Hoshino, and A. R. P. Rau, Rev. Mod. Phys. **88**, 025004 (2016).
[27] R. D. White, D. Cocks, G. Boyle, M. Casey, N. Garland, D. Konovalov, B. Philippa, P. Stokes, J. de Urquijo, O. González-Magaña, R. P. McEachran, S. J. Buckman, M. J. Brunger, G. Garciá, S. Dujko, and Z. Lj. Petrović, Plasma Sources Sci. Technol. **27**, 053001 (2018).
[28] Ž. Mladenovic, S. Gocić, D. Marić, and Z. L. Petrović, Eur. Phys. J. Plus **133**, 344 (2018).
[29] N. Škoro, N. Puač, S. Živković, D. Krstić-Milasević, U. Cvelbar, G. Malović, and Z. L. Petrović, Eur. Phys. J. D **72**, 2 (2018).
[30] M. C. Fuss, L. Ellis-Gibbings, D. B. Jones, M. J. Brunger, F. Blanco, A. Muñoz, P. Limão-Vieira, and G. García, J. Appl. Phys. **117**, 214701 (2015).
[31] P. J. Bruggeman, M. J. Kushner, B. R. Locke, J. G. E. Gardeniers, W. G. Graham, D. B. Graves *et al.*, Plasma Sources Sci. Technol. **25**, 053002 (2016).
[32] I. Adamovich *et al.*, J. Phys. D **50**, 323001 (2017).
[33] I. A. Mironova, K. L. Aplin, F. Arnold, G. A. Bazilevskaya, R. G. Harrison, A. A. Krivolutsky, K. A. Nicoll, E. V. Rozanov, E. Turunen, and I. G. Usoskin, Space Sci. Rev. **194**, 1 (2015).
[34] L. Campbell and M. J. Brunger, Int. Rev. Phys. Chem. **35**, 297 (2016).
[35] M. A. Ridenti, J. Amorim Filho, M. J. Brunger, R. F. da Costa, M. T. do N. Varella, M. H. F. Bettega, and M. A. P. Lima, Eur. Phys. J. D **70**, 161 (2016).
[36] P. D. Burrow, J. A. Michejda, and J. Comer, J. Phys. B **9**, 3225 (1976).
[37] J. P. Sullivan, P. D. Burrow, D. S. Newman, K. Bartschat, J. A. Michejda, R. Panajotović, R. P. McEachran, and S. J. Buckman, New J. Phys. **5**, 159 (2003).
[38] R. T. Brinkman and S. Trajmar, J. Phys. E **14**, 245 (1981).
[39] M. J. Brunger and S. J. Buckman, Phys. Rep. **357**, 215 (2002).
[40] L. J. Allen, M. J. Brunger, I. E. McCarthy, and P. J. O. Teubner, J. Phys. B **20**, 4861 (1987).
[41] M. J. Brunger, S. J. Buckman, L. J. Allen, I. E. McCarthy, and K. Ratnavelu, J. Phys. B **25**, 1823 (1992).
[42] D. Goebel, U. Hohm, and G. Maroulis, Phys. Rev. A **54**, 1973 (1996).
[43] O. Zatsarinny, K. Bartschat, G. Garciá, F. Blanco, L. R. Hargreaves, D. B. Jones, R. Murrie, J. R. Brunton, M. J. Brunger, M. Hoshino, and S. J. Buckman, Phys. Rev. A **83**, 042702 (2011).
[44] S. Chen, R. P. McEachran, and A. D. Stauffer, J. Phys. B **41**, 025201 (2008).
[45] I. P. Grant, B. J. McKenzie, P. H. Norrington, D. F. Mayer, and N. C. Pyper, Comput. Phys. Commun. **21**, 207 (1980).
[46] R. P. McEachran, D. L. Morgan, A. G. Ryman, and A. D. Stauffer, J. Phys. B **10**, 663 (1977).
[47] R. P. McEachran, D. L. Morgan, A. G. Ryman, and A. D. Stauffer, J. Phys. B **11**, 951 (1978).
[48] R. P. McEachran and A. D. Stauffer, J. Phys. B **23**, 4605 (1990).
[49] K. Bartschat (private communication).
[50] M. J. Brunger, Int. Rev. Phys. Chem. **36**, 333 (2017).
[51] S. T. Perkins, D. E. Cullen, and S. M. Seltzer, LLNL Evaluated Electron Data Library, UCRL-50400 Vol. 31 (Lawrence Livermore National Laboratory, Livermore, California, 1991).
[52] R. J. Zollweg, J. Chem. Phys. **50**, 4251 (1969).
[53] K. Bartschat, O. Zatsarinny, I. Bray, D. V. Fursa, and A. T. Stelbovics, J. Phys. B **37**, 2617 (2004).
[54] R. P. McEachran and A. D. Stauffer, J. Phys. B **25**, 1527 (1992).
[55] M. Bartsch, H. Geesman, G. F. Hanne, and J. Kessler, J. Phys. B **25**, 1511 (1992).

Croat Med J. 2019;60:78-86
https://doi.org/10.3325/cmj.2019.60.78

Raman microspectroscopy: toward a better distinction and profiling of different populations of dental stem cells

Jelena Simonović[1], Boško Toljić[1], Božidar Rašković[2], Vladimir Jovanović[3], Miloš Lazarević[1], Maja Milošević[1], Nadja Nikolić[1], Radmila Panajotović[4], Jelena Milašin[1]

[1]School of Dental Medicine, University of Belgrade, Belgrade, Serbia

[2]Faculty of Agriculture, Institute of Animal Sciences, University of Belgrade, Belgrade, Serbia

[3]Institute for Multidisciplinary Research, University of Belgrade, Belgrade, Serbia

[4]Institute of Physics, University of Belgrade, Belgrade, Serbia

Aim To characterize stem cells originating from different dental tissues (apical papilla [SCAP], dental follicle [DFSC], and pulp [DPSC]) and test the capacity of Raman microspectroscopy to distinguish between the three dental stem cell types.

Methods SCAP, DFSC, and DPSC cultures were generated from three immature wisdom teeth originating from three patients. Cell stemness was confirmed by inducing neuro-, osteo-, chondro-, and adipo-differentiaton and by mesenchymal marker expression analysis by flow-cytometry and real-time polymerase chain reaction. Cellular components were then evaluated by Raman microspectroscopy.

Results We found differences between SCAP, DFSC, and DPSC Raman spectra. The ratio between proteins and nucleic acids (748/770), a parameter for discriminating more differentiated from less differentiated cells, showed significant differences between the three cell types. All cells also displayed a fingerprint region in the 600-700 cm^{-1} range, and characteristic lipid peaks at positions 1440 cm^{-1} and 1650 cm^{-1}.

Conclusion Although different dental stem cells exhibited similar Raman spectra, the method enabled us to make subtle distinction between them.

Received: February 14, 2019

Accepted: April 13, 2019

Correspondence to:
Jelena Milašin
School of Dental Medicine,
University of Belgrade
Dr Subotića 8
11000 Belgrade, Serbia
jelena.milasin@stomf.bg.ac.rs

Dental tissues contain stem cells with high proliferation and differentiation potential, showing great promise for use in regenerative and reparative dentistry, and medicine in general (1,2). Although dental stem cells are multipotent, adult, mesenchymal stem cells (MSCs), originating from the neural crest (3-5), it is difficult to make a precise distinction among the increasing number of newly discovered subpopulations. They rapidly emerge as an attractive biomaterial due to their accessibility and easy isolation compared with embryonic stem cells (ESCs). Dental stem cells (DSCs) can be obtained from several dental tissues, including apical papilla (SCAP), dental pulp of permanent teeth (DPSC), and dental follicle (DFSC) (6).

SCAP can easily be collected after the extraction of immature third molar, from a soft, developing tissue called the apical papilla present at the end of incompletely formed roots. DFSCs are isolated from dental follicle, a sac surrounding the enamel organ and the dental papilla of the developing tooth germ prior to eruption, while DPSC are isolated from the permanent tooth pulp. Although there is a marked resemblance between the three types of cells, they also show some differences in their stemness potential (7-10). An accurate method that would precisely assess stem cell characteristics and help in determining the most appropriate type of cell source for a given regenerative procedure, ie, for the application in different and specific clinical settings, has not yet been established (11).

Raman spectromicroscopy (RS) has been widely used to characterize dental mineral tissues (12-14), showing no apparent negative effects on cells (cellular morphology, proliferation, and other features) due to laser exposure (15-17).

RS has been previously applied to discriminate MSCs from ESCs based on the amount of intracellular lipids (18); to identify various stages of mesenchymal and embryonic murine stem cell differentiation (18-20); and before transplantation, to discriminate normal from abnormal stem cells in *ex vivo* cultures (21). Considering numerous advantages of adult stem cells over ESC, and the growing importance of dental stem cells, we compared DSCs in terms of their structural fingerprint, ie, their biochemical characteristics, by means of Raman spectromicroscopy (RS). The aim of this study was to assess the ability of Raman spectroscopy to discriminate between SCAP, DPSC, and DFSC.

MATERIAL AND METHODS

Isolation of SCAP, DFSCs and DPSCs

The material was obtained from three immature wisdom teeth (Figure 1), obtained from three patients aged between 14 and 15 years (one tooth per patient). Atraumatical teeth extraction was performed at the Clinic for Oral Surgery, School of Dental Medicine, University of Belgrade, in 2016, after having obtained a written informed consent from the patients' parents. The study was approved by the

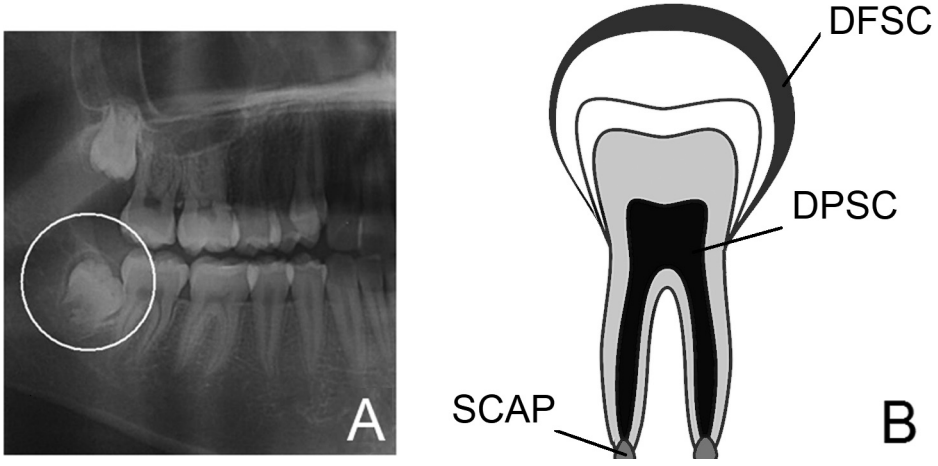

FIGURE 1. Orthopantomograph of the impacted third molar (**A**) and schematic representation of the three types of tissues used in the analysis: DFSC – dental follicle stem cells; DPSC – dental pulp stem cells; SCAP – apical papilla stem cells (**B**).

Ethics Committee of the School of Dental Medicine, University of Belgrade.

Teeth were immediately transported to the laboratory and further processed under sterile conditions. Tooth surfaces were thoroughly rinsed with Dulbecco's phosphate buffered saline solution (DPBS, Thermo Fisher Scientific, Waltham, MA, USA), and dental tissues were isolated as previously described (22-24). Briefly, the apical papilla was gently scrapped from the root apex, the dental follicle was separated from the tooth crown with a surgical blade, and the dental pulp tissue was extracted with an endodontic instrument, after having exposed the pulp chamber by crushing the tooth with a sterile clamp. Stem cells were derived without enzymatic digestion (25). Tissues were cut into 1 mm^3 pieces and separately transferred into Dulbecco's Modified Eagle Medium (DMEM) supplemented with 10% fetal bovine serum (FBS) and 1% antibiotic-antimycotic solution (all from Thermo Fisher Scientific, Waltham, MA, USA), and cultivated under standard conditions at 37°C and 5% CO_2. Cell cultures were passaged after reaching 80% confluence. The experiments were done on fifth-passage cells.

Cell differentiation capacity

To induce neurogenic differentiation, cells were seeded onto T-25 tissue culture flasks in standard culture medium at the density of 1.5×10^5 cells. Control cells were incubated in standard culture medium. After 24 hours, neural preinduction medium and DMEM with 100 mM beta-mercaptoethanol were added, and cells were incubated for 4 hours. Cell differentiation was continued in a neural induction medium containing recombinant human basic fibroblast growth factor, neural growth factor, and B27 supplement (all from Thermo Fisher Scientific) in DMEM. After 7 days, cell morphology was analyzed under inverted microscope (Primovert Zeiss, Jena, Germany). To induce osteogenic differentiation, cells were seeded in six-well plates with the seeding density of 5×10^3 and cultivated for 28 days in osteogenic differentiation medium (StemPro, Thermo Fisher Scientific). To induce chondrogenic differentiation, cells were seeded in the form of micromass at a total number of 1.6×10^6 and cultivated in a medium for chondrogenic differentiation (StemPro) for 21 days. To induce adipo-differentiation, cells were seeded in six-well plates 1×10^4 cells/cm^2 and cultivated for 28 days in adipogenic medium (StemPro). To determine successful differentiation, appropriate staining protocols were used. Osteogenic differentiation was confirmed by the presence of mineralization fields stained with 2% Alizarin Red S solution (Centrohem, Belgrade, Serbia); adipogenic differentiation by the presence of neutral lipids stained with 0.5% Oil Red O solution (Sigma Aldrich, Munich, Germany); and chondro-differentiation by the presence of proteoglycan molecules stained with 0.1% Safranin O solution (Centrohem). After staining, the cells were rinsed with DPBS, fixed for 30 minutes with 4% paraformaldehyde, observed under inverted microscope, and photographed.

Flow cytometry analyses

The markers used for flow-cytometry were fluorescein-isothiocyanate (FITC)-labeled monoclonal antibodies against CD90, CD105, CD34, and phycoerythrin (PE)-labeled mouse monoclonal antibodies against CD73 and CD45. After trypsinization, cells were resuspended in 10% FBS in DPBS (about 1×10^6 cells for every sample). Antibody concentrations were recommended by the manufacturer (Exbio, Prague, Czech Republic). Cells were incubated in the dark for 45 minutes at 4°C with the appropriate combination of antibodies: CD34 (FITC) and CD73 (PE), CD45 (PE) and CD105 (FITC). CD90 (FITC) was added separately. After incubation, cells were rinsed twice with DPBS and analyzed on a multi-laser flow cytometer system (Partec, Munster, Germany).

Real-time polymerase chain reaction (PCR)

The expression of cell surface mesenchymal markers was assessed by using real-time PCR (qPCR). RNA was isolated by using TRIzol Reagent (Thermo Fisher Scientific), according to manufacturers' recommendation. Subsequent reverse transcription from 1 µg of total RNA was performed using RevertAid First Strand cDNA Synthesis Kit (Thermo Fisher Scientific) in order to obtain cDNA for qPCR analysis. The list of specific primers (for CD73, CD90, CD45, CD133, and housekeeping gene *GAPDH*) is given in Table 1.

TABLE 1. List of primers used for quantitative polymerase chain reaction

Cell marker	Sequence of primers (5'→3')
CD73	Forward: GAGTGGGTGGTCAGAAAATA Reverse: TGCACACTGTTTTTAAGGTG
CD90	Forward: TAACAGTCTTGCAGGTCTCC Reverse: AAGGCGGATAAGTAGAGGAC
CD45	Forward: GCAAAGATGCCCAGTGTTCCACTT Reverse: ATCTGAGGTGTTCGCTGTGATGGT
CD133	Forward: ACTTGGCTCAGACTGGTAAA Reverse: GTTCTGAGCAAAATCCAGAG
GAPDH	Forward: TCATGACCACAGTCCATGCCATCA Reverse: CCCTGTTGCTGTAGCCAAATTCGT

The results obtained from each qPCR run were threshold cycle (Ct) values. The relative expression level was assessed using the ΔΔCt method. The relative mRNA expression levels for mesenchymal and hematopoietic markers for each sample were calculated as the ratio between the expression of the gene of interest and the expression of the selected housekeeping gene (*GAPDH*).

Raman microspectroscopy sample preparation

Cells from the fifth passage were cultivated in growth medium until confluent. After passaging and cell counting, the cells were brought to a concentration of 1×10^6 per mL of the medium. After centrifugation at 300 g for 6 minutes at room temperature, cell pellets were transferred to a golden plate for Raman spectromicroscopy, without fixation.

Spectroscopic measurements

The Raman spectra of pellets were recorded in the range from 400-2600 cm^{-1} with a Horiba Jobin Yvon Xplora device (Horiba Jobin Yvon S.A.S., Villeneuve-d'Ascq, France) equipped with a BX51 microscope (Olympus, Tokyo, Japan). Raman scattering was excited by a laser diode at the wavelength of 785 nm, with a laser power of 90 mW incident on the pellets and the spot size of around 2 µm. Before spectra acquisition was started, the pellet upper surface was visualized and focused by using a microscope with a lens of 100× magnification. Each pellet was measured by the Raman device at 25 different spots by using a random movement in order to obtain mean spectra of the sample. The acquisition time per spectrum was 100 s. The dispersive spectrometer had an entrance slit of 100 µm and a focal length of 200 mm, grating of 600 lines/mm, and average spectral resolution of 2.5 cm^{-1}. The Raman-scattered light was detected by a thermoelectrically cooled CCD camera (Syncerity, Horiba Scientific, Edison, NJ, USA) operating at 213 K. The spectral acquisition was performed by using LabSpec 6 software (Horiba Scientific, Villeneuve-d'Ascq). For the calibration procedure, the spectra of an aspirin (4-acetylsalicylic acid) were measured daily as a reference control and for subsequent data processing. The achieved signal-to-noise ratio was at least 20.

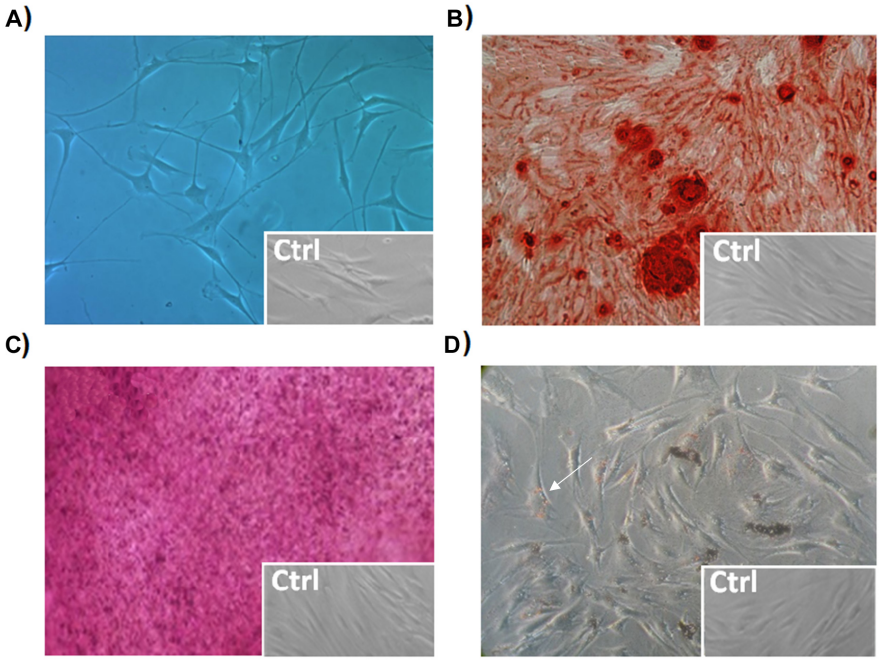

FIGURE 2. Representative examples of dental stem cell (apical papilla) differentiation into four different lineages (magnification 100×). Slender projections indicated neuro-differentiation (**A**); Alizarin Red S stained extracellular mineral deposits indicated osteogenic differentiation (**B**); Safranin O stained areas with proteoglycan presence indicated chondrogenic differentiation (**C**); and positive Oil Red O staining indicated lipid droplets accumulation, ie, adipogenic differentiation (**D**). Ctrl – control.

Data processing

Each Raman spectrum (250 spectra in total, around 25 spectra per cell type per patient) was first corrected by subtracting its baseline, determined as a 4th order polynomial fitted through several characteristic points (at around 425, 615, 1700, 2100, and 2500 cm^{-1}) of the spectrum. Peaks in Raman spectra due to cosmic rays were removed. Then, all spectra were smoothed by Savitzky-Golay filter, using a second-order polynomial. After smoothing, vector normalization was applied to all spectra between 400 and 1800 cm^{-1}. Mean and standard deviation was determined for normalized spectra for each cell type (around 75 spectra per cell type): SCAP, DFSC and DPSC.

Statistical analysis

The normality of distribution was assessed by using Kolmogorov-Smirnov test. The differences between Raman spectra intensities were determined by one way analysis of variance (ANOVA) or Kruskal-Wallis' H-test, followed by Tukey's post-hoc analysis or Bonferroni corrected Mann-Whitney U test, where appropriate. The level of significance was set at $P=0.05$. For Bonferroni corrected Mann-Whitney U test we used a stricter probability value (less than 0.017). Statistical analysis was performed using the SPSS 17.0 statistical package (SPSS, Chicago, IL, USA).

RESULTS

Multilineage differentiation

Specific cell morphology confirmed neurogenic differentiation; Alizarin Red S staining of mineralized nodules around cells confirmed osteogenic differentiation; the presence of Oil Red O staining showed intracellular lipid accumulation; and the presence of Safranin O clusters of proteoglycans characteristic for cartilage cells confirmed chondro-differentiation (Figure 2). Cells of all the three origins displayed comparable behavior when induced toward a specific lineage. In the control group (non-induced cells) there were no stained cells.

Cell surface markers detection by flow-cytometry

SCAP, DFSC, and DPSCs were strongly positive for CD90, CD73, and CD105 (cell surface markers of mesenchymal

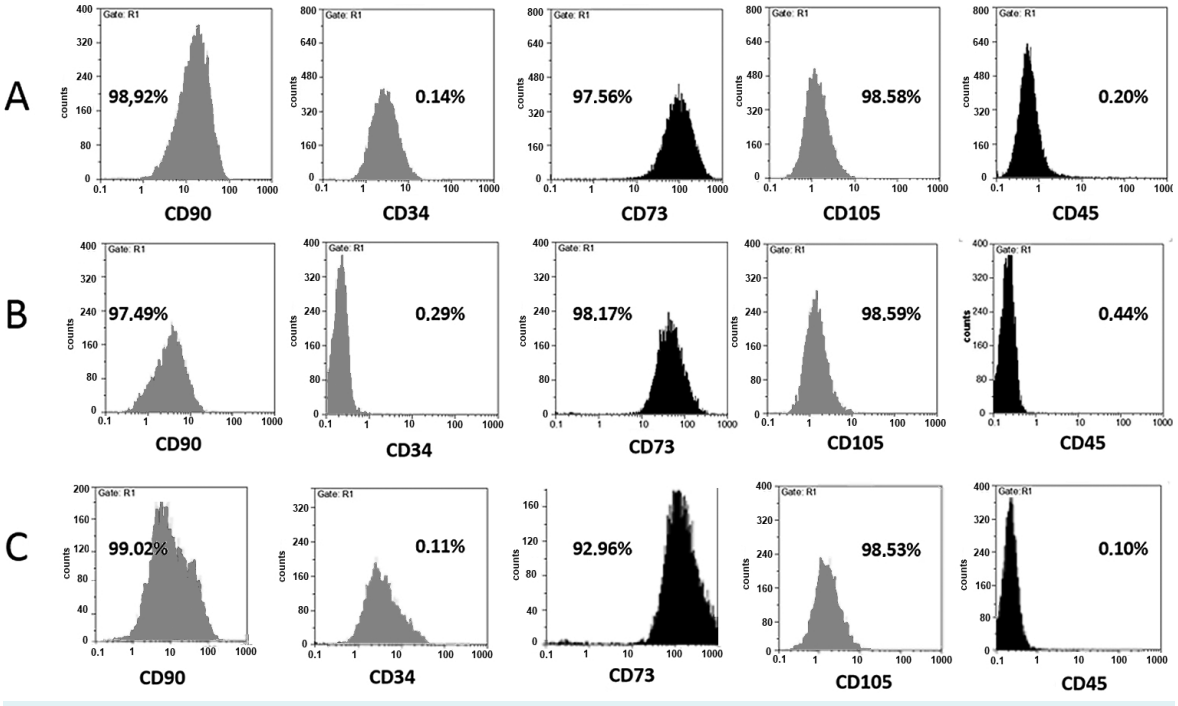

FIGURE 3. Immunophenotypic profile of mesenchymal stem cells derived from (**A**) dental pulp, (**B**) dental follicle, and (**C**) apical papilla, all strongly positive for CD90, CD73, and CD105 (markers associated with mesenchymal stem cells) and negative for CD45 and CD34 (markers of hematopoietic cells).

stem cells) and negative for CD45 and CD34 (cell surface markers of hematopoietic cells) (Figure 3). No significant difference was observed between different cell types based on flow-cytometry.

Gene expression analysis by real-time PCR

The main mesenchymal markers expression was confirmed in all three cell groups, without significant differ-

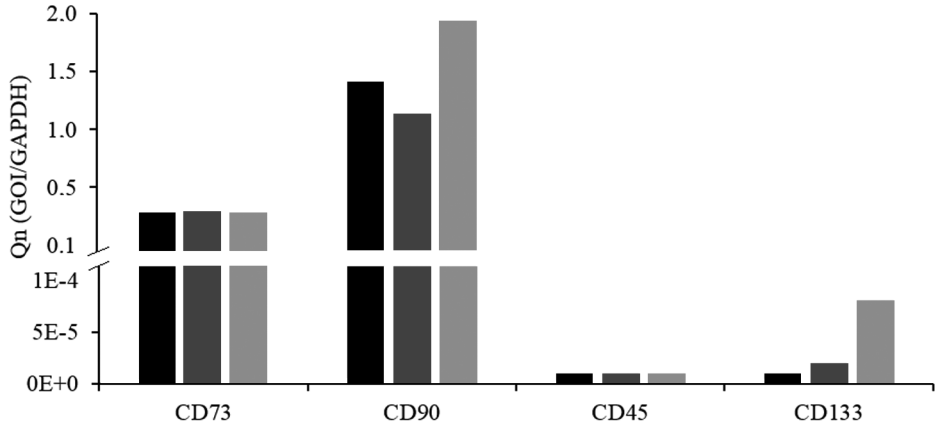

FIGURE 4. Relative gene expression of mesenchymal (CD73 and CD90) and hematopoietic markers (CD45 and CD133) of stem cells isolated from dental pulp (DPSC, black), apical papilla (SCAP, dark gray), and dental follicle (DFSC, light gray).

TABLE 2. Biochemical differences between apical papilla (SCAP), dental follicle (DFSC), and pulp stem cells (DPSC) determined by Raman spectroscopy and vector-normalized

	Raman intensity peaks in			*P*-values		
Wavenumber (cm^{-1})/ assignment	SCAP	DFSC	DPSC	SCAP vs DFSC	SCAP vs DPSC	DFSC vs DPSC
471 glycogen*	-0.043 (0.021)	-0.047 (0.012)	-0.047 (0.038)	0.008	0.501	0.166
612 C-C stretch	-0.046 ± 0.002	-0.048 ± 0.002	-0.047 ± 0.002	<0.001	0.001	0.376
706 lipids*	-0.013 (0.011)	-0.013 (0.012)	-0.014 (0.013)	NS	NS	NS
748 protein	-0.017 ± 0.003	-0.018 ± 0.004	-0.017 ± 0.004	NS	NS	NS
770 DNA-RNA	-0.026 ± 0.004	-0.018 ± 0.005	-0.017 ± 0.003	<0.001	<0.001	0.950
843 glycoprotein	0.040 ± 0.006	0.037 ± 0.009	0.044 ± 0.010	0.079	0.002	<0.001
929 glycoprotein	0.042 ± 0.008	0.038 ± 0.008	0.044 ± 0.012	0.010	0.267	<0.001
990 tryptophan	0.078 ± 0.007	0.074 ± 0.008	0.077 ± 0.011	0.004	0.392	0.131
1023 proteins	0.032 ± 0.005	0.030 ± 0.006	0.034 ± 0.007	0.111	0.024	<0.001
1074 lipids	0.053 ± 0.005	0.051 ± 0.006	0.055 ± 0.009	0.194	0.041	<0.001
1094 DNA*	0.045 (0.020)	0.045 (0.006)	0.046 (0.012)	0.108	0.164	0.006
1116 protein*	0.046 (0.010)	0.043 (0.010)	0.045 (0.020)	0.016	0.495	0.002
1198 nucleic acid*	0.033 (0.010)	0.035 (0.010)	0.031 (0.000)	0.028	0.004	<0.001
1252 lipids	0.078 ± 0.006	0.081 ± 0.008	0.075 ± 0.008	0.010	0.163	<0.001
1293 lipids*	0.080 (0.010)	0.081 (0.010)	0.079 (0.010)	0.086	0.194	0.004
1329 guanine	0.070 ± 0.004	0.068 ± 0.004	0.070 ± 0.006	0.043	0.978	0.023
1440 lipids, proteins*	0.100 (0.010)	0.096 (0.020)	0.100 (0.020)	NS	NS	NS
1546 nucleic acid	0.091 ± 0.004	0.090 ± 0.006	0.089 ± 0.008	<0.001	0.269	<0.001
1650 proteins	0.026 ± 0.008	0.025 ± 0.008	0.022 ± 0.010	0.816	0.020	0.088
748/770	0.809 ± 0.168	0.888 ± 0.204	0.972 ± 0.176	0.018	<0.001	0.009

*Data are presented as mean ± standard deviation or median (inter-quartile range). *P* values represent differences between groups determined by one-way analysis of variance (ANOVA) or Kruskal-Wallis' H-test*, followed by Tukey's post-hoc analysis or Mann-Whitney U test, where appropriate. Bonfferoni's correction was applied after Kruskal-Wallis' H-test.

ence between the cells, while the expression of hematopoetic markers was negligible in all samples (Figure 4).

Raman spectromicroscopy

Cell spectra of the three patients, when averaged, showed obvious similarities (Figure 5). However, there were significant differences between SCAP, DFSC, and DPSC (Table 2). Generally speaking, the most important differences were noticed between DFSC and DPSC; namely, out of 20 prominent peaks, 11 showed significant differences. Significant differences between SCAP and DFSC were observed in 8 peaks, while significant differences between SCAP and DPSC were observed only in 4 peaks. The parameter R4 (the ratio between proteins and nucleic acids, 748/770), which is considered to be a reliable parameter for the discrimination between more and less differentiated cells (15), showed a significant difference between the three cell types (SCAP vs DFSC, $P=0.018$; SCAP vs DPSC, $P<0.001$; DFSC vs DPSC, $P=0.009$). From the R4 values it can tentatively be concluded that the decreasing potency of the analyzed cells was: SCAP>DFSC>DPSC.

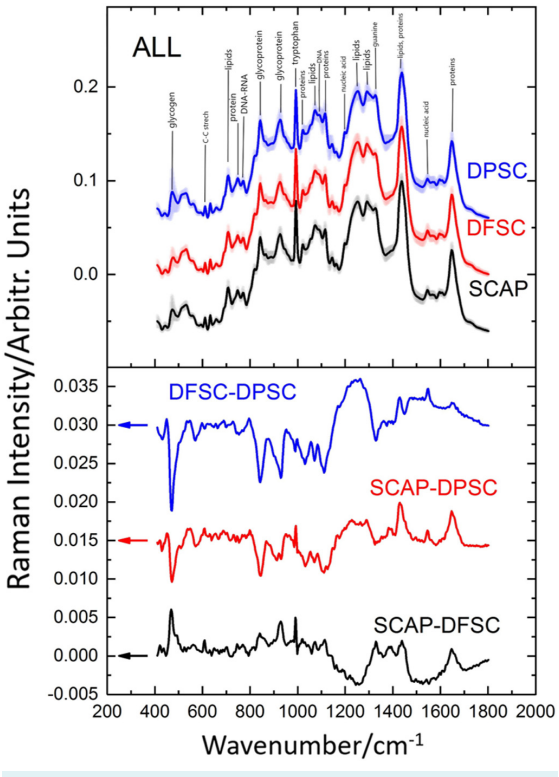

FIGURE 5. Raman spectra of different cell types averaged over all three subjects (75 spectra per cell type), offset for clarity. Shaded regions mark the standard deviation of spectra (upper panel); spectra subtracted from each other to emphasize the differences (lower panel).

DISCUSSION

In the present study, the use of standard methodologies for quantitative and qualitative estimation of stemness characteristics of dental tissue cells suggested that SCAP, DFSC, and DPSC exhibited very similar phenotypic characteristics during cultivation and differentiation. Although different dental stem cells exhibited similar Raman spectra, the method enabled us to make a subtle distinction between them.

Several cellular components are closely related to stemness characteristics. Stem cells must constantly maintain a fine balance between anabolism and catabolism, and metabolic plasticity is seen as a crucial phenomenon in the regulation of stem cell transition from self-renewal to lineage specification (26). For instance, glycogen is considered a regulator of potency and cellular differentiation capacity. Although the function of increased storage and production of glycogen in human stem cells is not fully understood, glycogen synthesis seems to be crucial for self-renewal, cell survival, growth rates, shorter doubling time, and differentiation (27,28). High glycogen accumulation is also typically observed in human embryonic stem cells, though its level has not been fully investigated in other stem cells types (29). These findings are in line with the present study, as Raman peaks for glycogen/glycoproteins at 470, 841, and 927 cm^{-1} showed substantial intensities in all cell types.

Lipids are also considered to be closely linked to stem cells potency (20,30), and lipid metabolism has a pivotal role in stem cell fate determination (31,32). Namely, inhibition of the eicosanoid pathway is associated with the maintenance of the pluripotent state in murine ESC (32). The eicosanoid pathway promotes the hydrolysis of membrane phospholipids by releasing lipid messengers into the cytoplasm (32), and their level progressively decreases during differentiation (18). In our study, all three cell types in all patients exhibited substantial lipid levels as judged by the very characteristic peaks at 1440 and 1650 cm^{-1}.

Nucleic acids content could also be considered as a marker of stemness (33,34), as well as the ratio between protein (tryptophan) and nucleic acids. While proteins have more prominent peaks in differentiated cells, nucleic acids quanti-

ty, on the contrary, decreases during differentiation, ie, there is a dominance-reversal in differentiated cells. Tryptophan (protein) peak vs nucleic acid peak (748 vs 770 cm^{-1}) ratio is therefore considered as a differentiation status indicator (18,35). In the present study, highly significant differences in this ratio were obtained between the three cell types. As judged by R4, the decreasing differentiation potential of the three types of cells was as follows: SCAP>DFSC>DPSC. This result, however, must be interpreted with caution, since it can probably vary depending on the patient's age and the stage of tooth development. Further studies, on a larger sample and on other cell populations would also be necessary for final conclusions to be drawn.

New cell subpopulations are emerging, especially in the orofacial region (36), necessitating the use of different techniques that are able to distinguish among them in order to better understand their lineage relationships. Raman microspectroscopy can provide a rapid, non-invasive, and label-free tool for uncovering subtle biochemical differences that can be used to distinguish more potent from less potent stem cells. The present study brings new insights into dental stem cell characteristics, enhancing the possibility of their clinical application.

Acknowledgments We thank Dr Djordje Miljkovic from the Institute of Biological Research, University of Belgrade, for the flow-cytometry analyses.

Funding This work was supported by grant No. 175075 of the Ministry of Education, Science and Technological Development of Serbia.

Ethical approval given by the Ethics Committee of the School of Dental Medicine, University of Belgrade.

Declaration of authorship JS conceived and designed the study; all authors acquired, analyzed and interpreted the data; JS, ML, and MM drafted the manuscript; all authors gave approval of the version to be submitted; agree to be accountable for all aspects of the work.

Competing interests All authors have completed the Unified Competing Interest form at www.icmje.org/coi_disclosure.pdf (available on request from the corresponding author) and declare: no support from any organization for the submitted work; no financial relationships with any organizations that might have an interest in the submitted work in the previous 3 years; no other relationships or activities that could appear to have influenced the submitted work.

References

1 La Noce M, Paino F, Spina A, Naddeo P, Montella R, Desiderio V, et al. Dental pulp stem cells: state of the art and suggestions for a true translation of research into therapy. J Dent. 2014;42:761-8. Medline:24589847 doi:10.1016/j.jdent.2014.02.018

2 Neel E, Chrzanowski W. Salih Vm, Kim H-W, Knowles J. Tissue engineering in dentistry. J Dent. 2014;42:915-28. Medline:24880036 doi:10.1016/j.jdent.2014.05.008

3 Le Blanc K, Davies L. MSCs—cells with many sides. Cytotherapy. 2018;20:273-8. Medline:29434007 doi:10.1016/j.jcyt.2018.01.009

4 Anitua E, Troya M, Zalduendo M. Progress in the use of dental pulp stem cells in regenerative medicine. Cytotherapy. 2018;20:479-98. Medline:29449086 doi:10.1016/j.jcyt.2017.12.011

5 Nuti N, Corallo C. Chan Bm, Ferrari M, Gerami-Naini B. Multipotent differentiation of human dental pulp stem cells: a literature review. Stem Cell Rev. 2016;12:511-23. Medline:27240827 doi:10.1007/s12015-016-9661-9

6 Suchánek J, Browne K, Kleplová T, Mazurová Y. Protocols for dental-related stem cells isolation, amplification and differentiation. In: Dental stem cells: regenerative potential. Berlin: Springer; 2016. p. 27-56.

7 Huang G, Sonoyama W, Liu Y, Liu H, Wang S, Shi S. The hidden treasure in apical papilla: the potential role in pulp/dentin regeneration and bioroot engineering. J Endod. 2008;34:645-51. Medline:18498881 doi:10.1016/j.joen.2008.03.001

8 Sonoyama W, Liu Y, Yamaza T, Tuan R, Wang S, Shi S, et al. Characterization of the apical papilla and its residing stem cells from human immature permanent teeth: a pilot study. J Endod. 2008;34:166-71. Medline:18215674 doi:10.1016/j.joen.2007.11.021

9 Sonoyama W, Liu Y, Fang D, Yamaza T, Seo BM, Zhang C, et al. Mesenchymal stem cell-mediated functional tooth regeneration in swine. PLoS One. 2006;1:e79. Medline:17183711 doi:10.1371/journal.pone.0000079

10 Egusa H, Sonoyama W, Nishimura M, Atsuta I, Akiyama K. Stem cells in dentistry–part I: stem cell sources. J Prosthodont Res. 2012;56:151-65. Medline:22796367 doi:10.1016/j.jpor.2012.06.001

1 Saito M, Silvério K, Casati M, Sallum E, Nociti F. Tooth-derived stem cells: Update and perspectives. World J Stem Cells. 2015;7:399-407. Medline:25815123 doi:10.4252/wjsc.v7.i2.399

12 Santini A, Miletic V. Quantitative micro-Raman assessment of dentine demineralization, adhesive penetration, and degree of conversion of three dentine bonding systems. Eur J Oral Sci. 2008;116:177-83. Medline:18353013 doi:10.1111/j.1600-0722.2008.00525.x

13 Levallois B, Terrer E, Panayotov Y, Salehi H, Tassery H, Tramini P, et al. Molecular structural analysis of carious lesions using micro-Raman spectroscopy. Eur J Oral Sci. 2012;120:444-51. Medline:22985003 doi:10.1111/j.1600-0722.2012.00988.x

14 Kuramochi E, Iizuka J, Mukai Y. Influences of bicarbonate on processes of enamel subsurface remineralization and demineralization: assessment using micro-Raman spectroscopy and transverse microradiography. Eur J Oral Sci. 2016;124:554-8. Medline:27699866 doi:10.1111/eos.12301

15 Schulze H, Konorov S, Caron N, Piret J, Blades M, Turner R. Assessing differentiation status of human embryonic stem cells noninvasively using Raman microspectroscopy. Anal Chem. 2010;82:5020-7. Medline:20481517 doi:10.1021/ac902697q

16 Puppels G, De Mul F, Otto C, Greve J, Robert-Nicoud M, Arndt-Jovin D, et al. Studying single living cells and chromosomes by confocal Raman microspectroscopy. Nature. 1990;347:301-3. Medline:2205805 doi:10.1038/347301a0

17 Konorov S, Glover C, Piret J, Bryan J, Schulze H, Blades M, et al. In situ analysis of living embryonic stem cells by coherent anti-stokes Raman microscopy. Anal Chem. 2007;79:7221-5. Medline:17691751 doi:10.1021/ac070544k

18 Pijanka J, Kumar D, Dale T, Yousef I, Parkes G, Untereiner V, et al. Vibrational spectroscopy differentiates between multipotent and pluripotent stem cells. Analyst. 2010;135:3126-32. Medline:20953512 doi:10.1039/c0an00525h

19 Notingher I, Bisson I, Bishop A, Randle W, Polak J, Hench L. In situ spectral monitoring of mRNA translation in embryonic stem cells during differentiation in vitro. Anal Chem. 2004;76:3185-93. Medline:15167800 doi:10.1021/ac0498720

20 Heraud P, Ng E, Caine S, Yu Q, Hirst C, Mayberry R, et al. Fourier transform infrared microspectroscopy identifies early lineage commitment in differentiating human embryonic stem cells. Stem Cell Res. 2010;4:140-7. Medline:20060373 doi:10.1016/j.scr.2009.11.002

21 Harkness L, Novikov S, Beermann J, Bozhevolnyi S, Kassem M. Identification of abnormal stem cells using Raman spectroscopy. Stem Cells Dev. 2012;21:2152-9. Medline:22251070 doi:10.1089/scd.2011.0600

22 Cortes O, Garcia C, Perez L, Boj J, Alcaina A. Pulp cell cultures obtained with two different methods for in vitro cytotoxicity tests. Eur Arch Paediatr Dent. 2006;7:96-9. Medline:17140535 doi:10.1007/BF03320822

23 Mori G, Ballini A, Carbone C, Oranger A, Brunetti G, Di Benedetto A, et al. Osteogenic differentiation of dental follicle stem cells. Int J Med Sci. 2012;9:480-7. Medline:22927773 doi:10.7150/ijms.4583

24 Wang L, Yan M, Wang Y, Lei G, Yu Y, Zhao C, et al. Proliferation and osteo/odontoblastic differentiation of stem cells from dental apical papilla in mineralization-inducing medium containing additional KH(2)PO(4). Cell Prolif. 2013;46:214-22. Medline:23510476 doi:10.1111/cpr.12016

25 Kerkis I, Caplan A. Stem cells in dental pulp of deciduous teeth. Tissue Eng Part B Rev. 2012;18:129-38. Medline:22032258 doi:10.1089/ten.teb.2011.0327

26 Folmes C, Dzeja P, Nelson T, Terzic A. Metabolic plasticity in stem cell homeostasis and differentiation. Cell Stem Cell. 2012;11:596-606. Medline:23122287 doi:10.1016/j.stem.2012.10.002

27 Chen R, Zhang G, Garfield S, Shi Y, Chen K, Robey P, et al. Variations in glycogen synthesis in human pluripotent stem cells with altered pluripotent states. PLoS One. 2015;10:e0142554. Medline:26565809 doi:10.1371/journal.pone.0142554

28 Tan Y, Konorov S, Schulze H, Piret J, Blades M, Turner R. Comparative study using Raman microspectroscopy reveals spectral signatures of human induced pluripotent cells more closely resemble those from human embryonic stem cells than those from differentiated cells. Analyst. 2012;137:4509-15. Medline:22888493 doi:10.1039/c2an35507h

29 Konorov S, Schulze H, Atkins C, Piret J, Aparicio S, Turner R, et al. Absolute quantification of intracellular glycogen content in human embryonic stem cells with Raman microspectroscopy. Anal Chem. 2011;83:6254-8. Medline:21702506 doi:10.1021/ac201581e

30 Folmes C, Park S, Terzic A. Lipid metabolism greases the stem cell engine. Cell Metab. 2013;17:153-5. Medline:23395162 doi:10.1016/j.cmet.2013.01.010

31 Yanes O, Clark J, Wong D, Patti G, Sánchez-Ruiz A, Benton H, et al. Metabolic oxidation regulates embryonic stem cell differentiation. Nat Chem Biol. 2010;6:411-7. Medline:20436487 doi:10.1038/nchembio.364

32 Notingher I, Verrier S, Haque S, Polak J, Hench L. Spectroscopic study of human lung epithelial cells (A549) in culture: living cells versus dead cells. Biopolymers. 2003;72:230-40. Medline:12833477 doi:10.1002/bip.10378

33 Cai J, Weiss M, Rao M. In search of "stemness". Exp Hematol. 2004;32:585-98. Medline:15246154 doi:10.1016/j.exphem.2004.03.013

34 Kelly G, Gatie M. Mechanisms regulating stemness and differentiation in embryonal carcinoma cells. Stem Cells Int. 2017;2017:3684178. Medline:28373885 doi:10.1155/2017/3684178

35 Ji M, Lewis S, Camelo-Piragua S, Ramkissoon S, Snuderl M, Venneti S, et al. Detection of human brain tumor infiltration with quantitative stimulated Raman scattering microscopy. Sci Transl Med. 2015;7:309ra163. Medline:26468325 doi:10.1126/scitranslmed.aab0195

36 Alajbeg I, Alić I, Andabak-Rogulj A, Brailo V, Mitrečić D. Oral Dis. Human- and mouse-derived neurons can be simultaneously obtained by co-cultures of human oral mucosal stem cells and mouse neural stem cells. Oral Dis. 2018;24:5-10. Medline:29480641 doi:10.1111/odi.12776

nanomaterials

MDPI

Article

The Effect of Liquid-Phase Exfoliated Graphene Film on Neurodifferentiation of Stem Cells from Apical Papilla

Jelena Simonovic [1], Bosko Toljic [1], Milos Lazarevic [1], Maja Milosevic Markovic [1], Mina Peric [2], Jasna Vujin [3], Radmila Panajotovic [3] and Jelena Milasin [1,*]

[1] School of Dental Medicine, University of Belgrade, 11000 Belgrade, Serbia
[2] Center for Laser Microscopy, Faculty of Biology, University of Belgrade, 11000 Belgrade, Serbia
[3] Graphene Laboratory, Center for Solid State Physics and New Materials, Institute of Physics, University of Belgrade, 11000 Belgrade, Serbia
* Correspondence: jelena.milasin@stomf.bg.ac.rs

Abstract: Background: Dental stem cells, which originate from the neural crest, due to their easy accessibility might be good candidates in neuro-regenerative procedures, along with graphene-based nanomaterials shown to promote neurogenesis *in vitro*. We aimed to explore the potential of liquid-phase exfoliated graphene (LPEG) film to stimulate the neuro-differentiation of stem cells from apical papilla (SCAP). Methods: The experimental procedure was structured as follows: (1) fabrication of graphene film; (2) isolation, cultivation and SCAP stemness characterization by flowcytometry, multilineage differentiation (osteo, chondro and adipo) and quantitative PCR (qPCR); (3) SCAP neuro-induction by cultivation on polyethylene terephthalate (PET) coated with graphene film; (4) evaluation of neural differentiation by means of several microscopy techniques (light, confocal, atomic force and scanning electron microscopy), followed by neural marker gene expression analysis using qPCR. Results: SCAP demonstrated exceptional stemness, as judged by mesenchymal markers' expression (CD73, CD90 and CD105), and by multilineage differentiation capacity (osteo, chondro and adipo-differentiation). Neuro-induction of SCAP grown on PET coated with graphene film resulted in neuron-like cellular phenotype observed under different microscopes. This was corroborated by the high gene expression of all examined key neuronal markers (Ngn2, NF-M, Nestin, MAP2, MASH1). Conclusions: The ability of SCAPs to differentiate toward neural lineages was markedly enhanced by graphene film.

Keywords: graphene; dental stem cells; stem cells from apical papilla; neurogenic differentiation

Citation: Simonovic, J.; Toljic, B.; Lazarevic, M.; Markovic, M.M.; Peric, M.; Vujin, J.; Panajotovic, R.; Milasin, J. The Effect of Liquid-Phase Exfoliated Graphene Film on Neurodifferentiation of Stem Cells from Apical Papilla. *Nanomaterials* **2022**, *12*, 3116. https://doi.org/10.3390/nano12183116

Academic Editors: Jinfeng Zhang, Minhuan Lan and Huiqing Peng

Received: 3 August 2022
Accepted: 5 September 2022
Published: 8 September 2022

1. Introduction

Regenerative medicine aims at replacing damaged human cells, tissues or organs and restoring their normal architecture and functions [1]. Stem cells (SCs) emerged as a promising tool in regenerative therapies due to their ability to differentiate into numerous cell lineages, high self-renewal capacity and immunosuppressive activity. A variety of new materials and new devices, enhancing cell migration, proliferation, and differentiation, have been developed as well [2,3].

Since SC research has dramatically evolved over the past years, it is possible now to isolate SCs from almost any tissue [4–7]. Yet, in many instances, the most appropriate and matching source of stem cells for a given regenerative therapy remains to be identified.

Dental SCs share a similar origin as neuronal stem cells, as they originate from the neural crest, and due to their accessibility and absence of ethical issues, they might be a good candidate for neuro-regeneration. Apical papilla is a soft tissue at the apex of a not fully formed tooth, containing more than 95% of mesenchymal SCs (stem cells from apical papilla, SCAP) [8,9]. SCAP express some early neural markers even without neural induction and can be transformed into different cell types belonging to neural lineage [10],

making them suitable for potential therapeutic applications in different clinical settings necessitating neuro-repair. SCAP differentiation potential has been extensively tested, but mainly in experiments of osteogenesis and odontogenesis. Only a few studies have dealt with the use of SCAP in neurodifferentiation. For instance, it was shown that fibrin gels [11] and hypoxia [12] stimulate SCAP neurogenesis.

Graphene, an allotrope of carbon, owing to its physico-chemical and biological properties, is also becoming increasingly popular in bioengineering [13–17]. Graphene and graphene-based nanomaterials (GBN), especially graphene oxide, improve cell adhesion during proliferation and differentiation and, due to their electrical conductivity, have the ability to promote the process of differentiation towards neural cells [18–26]. Furthermore, a colloidal dispersion of graphene demonstrated excellent biocompatibility, nontoxicity and remarkable support for cell proliferation [27–31].

As already stated, in numerous studies focusing on tissue engineering, graphene-based materials have been used in conjunction with different dental stem cells, such as dental pulp stem cells, periodontal ligament stem cells and dental follicle stem cells (reviewed by Guazzo et al. [32]). However, differentiation experiments involving graphene derivatives and stem cells from apical papilla are extremely scarce.

Given the lack of studies on SCAP biological behavior when in contact with graphene film, we sought to explore, by means of different microscopy techniquesand real-time gene expression analyses, the potential of liquid-phase exfoliated graphene (LPEG) film to induce and stimulate the neuro-differentiation of SCAP.

2. Materials and Methods

The experimental procedure was structured into four phases: phase 1—fabrication of graphene film; phase 2—isolation, cultivation and characterization of stem cells derived from apical papilla; phase 3—seeding stem cells on graphene film and PET; phase 4—evaluation of neural differentiation (Figure 1).

2.1. Fabrication of Graphene Film

2.1.1. Preparation of Graphene Dispersion

The graphene dispersion utilized in this study was prepared by the liquid-phase exfoliation method (LPE) [33]. Following the procedure described in our previous work [34], the mixture was made by adding the graphite powder (Sigma Aldrich-332461) in N-Methyl-2-pyrrolidone (NMP, Sigma Aldrich-328634). The initial concentration was 18 mg/mL. The solution was exposed to ultrasound (Sonic bath, Bransonic CPXH, Emerson, St. Louis, MO, USA) for 14 h and immediately after the sonication, the graphene dispersion was centrifuged for 60 min at 3000 rpm. The resulting graphene dispersion collected as the top 80% of the supernatant was characterized by UV-VIS spectroscopy (Beckman Coulter DU 720 UV/VIS Spectrophotometer, Brea, CA, USA) [33]. The concentration of LPE graphene dispersion was calculated by Lambert–Beer law [33] and it was 355 μg mL^{-1} (Figure 2).

2.1.2. Liquid-Phase Exfoliated Graphene Film Fabrication

Langmuir–Blodgett technique was applied to transfer graphene thin films from the liquid–gas interface to the solid support substrate [33]. Adding a small amount of liquid-phase exfoliation (LPE) graphene dispersion into the water–air interface, the graphene nanosheets were self-organized into a close-packed film [33]. The thin and transparent film was intently scooped onto the polyethylene terephthalate (PET) substrate. After deposition, the LPE graphene film was left to dry for 20 min in ambient conditions. For the optical characterization of the liquid-phase exfoliated graphene (LPEG) films, UV-VIS spectroscopy (Beckman Coulter DU 720 UV/VIS Spectrophotometer, Brea, CA, USA) was used. The transparence of 80% was estimated for the obtained LPEG film. The transparence of the obtained LPEG film at 550 nm was estimated at 80%, which is consistent with the previously reported study [35].

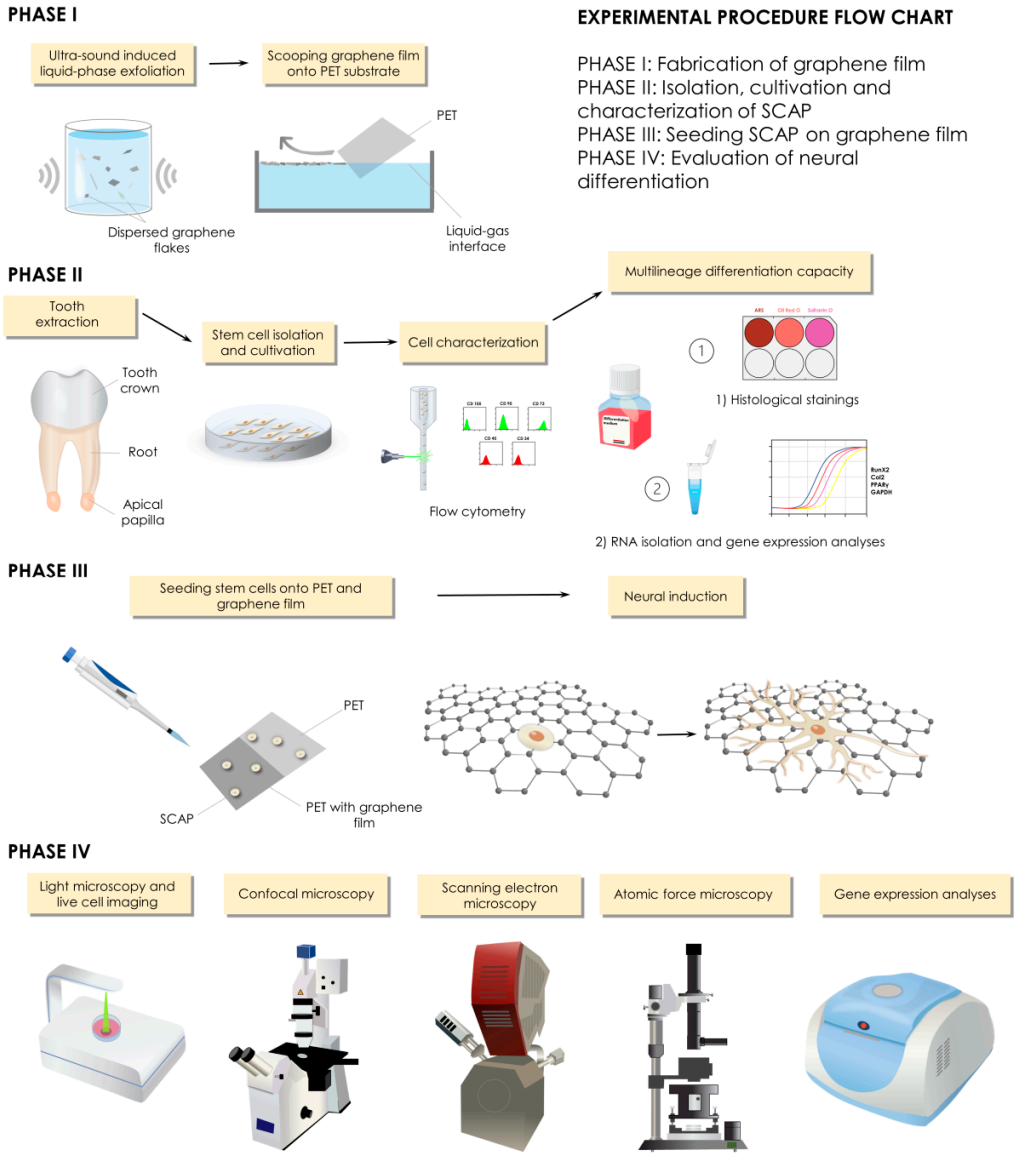

Figure 1. Study design and experimental procedures.

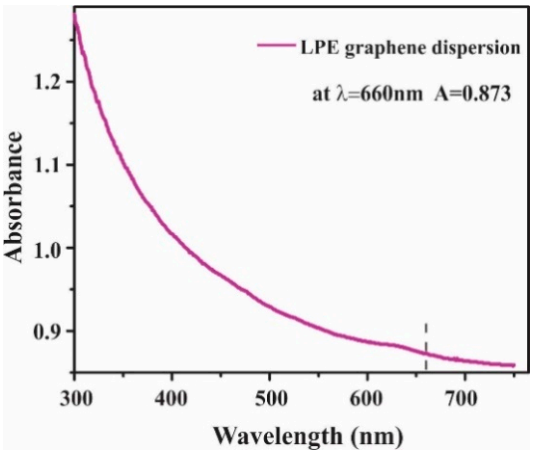

Figure 2. UV-VIS absorption spectrum of LPE graphene dispersion.

2.2. Graphene Film Characterization

2.2.1. Raman Spectroscopy of Graphene Film

Raman spectroscopy, as a noninvasive technique, has been used to provide essential information in the characterization of graphene-based materials [18,19]. Raman spectra were collected with the Micro-Raman Tri Vista 557 triple spectrometer using Nd:YAG laser (λ = 532 nm) and kept the power below 20 mW to avoid chemical damage of the film induced by the laser heating. The measurements were performed at room temperature and the acquisition time for spectra was 240 s.

2.2.2. Scanning Electron Microscopy (SEM) of Graphene Film

The morphology of the LBA graphene films was characterized with scanning electron microscopy (SEM). SEM mages were obtained by Tescan MIRA3 field emission gun SEM working at 20 kV acceleration (Tescan), and SiO2/Si wafer was used as a substrate.

2.2.3. Atomic Force Microscopy (AFM) of Graphene Film

Graphene film was characterized on an atomic force microscope (AFM), NTEGRA Spectra (NT-MDT). An NT MDT gold-plated tip with a nominal radius of about 30 nm was used. Scans were performed in ambient conditions, RH: 40–50%, t: 23–26 °C in semi-contact mode, with a scan frequency of 0.5 Hz and with 512 × 512 dots in the scan (10 × 10 µm surface). AFM image analysis has been performed using Gwyddionopen sourcesoftware package ver. 2.60 (Prague, Czech Republic). Thickness has been estimated at the edge of the film using profile function and statistical function in the software.

2.3. Cell Cultures

The study was approved by the Ethical Committee of the School of Dental Medicine, University of Belgrade (No 36/19). Immature, impacted third lower molar was extracted from a teenage patient at the Clinic for Oral Surgery (Figure 3), School of Dental Medicine, University of Belgrade, after signing the informed consents by patient's parents. Stem cells from apical papilla were isolated as previously described [34]. Briefly, extracted tooth was rinsed with Dulbecco's Phosphate-Buffered Saline (DPBS, Thermo Fisher Scientific, Waltham, MA, USA), and apical papilla was separated from the root apex and transferred into T-25 flasks after mincing. The tissues were grown in cell complete medium (DMEM supplemented with 10% fetal bovine serum and 1% antibiotic-antimycotic solution). Cells were cultured under standard conditions (37 °C, 95% air–5% CO_2 atmosphere, 95% humidity) and growth medium was changed every third day. All following experiments were carried out with the cells from the fourth and fifth passage.

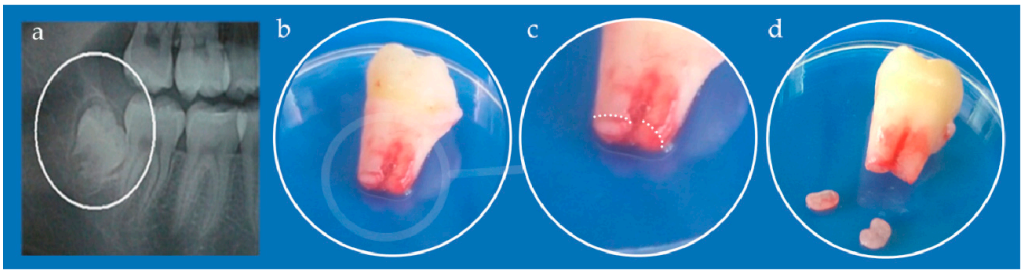

Figure 3. (**a**) Orthopantomogram of right mandibular impacted third molar (encircled); (**b**) Extracted tooth; (**c**) Detail from (**b**) white dotted line depicts border between apical papilla (lower parts) and tooth root (upper part); (**d**) Kidney-shaped apical papilla tissues separated from the tooth.

2.4. SCAP Characterization

2.4.1. Flow Cytometry

Flow cytometry analyses were performed in order to assess the expression of specific mesenchymal markers of SCAP. The markers used for these analyses were: fluorescein-

isothiocyanate-labeled mouse monoclonal antibodies against CD90, CD105, and CD34; phycoerythrin-labeled mouse monoclonal antibodies against CD73 and CD45 (all antibodies were purchased from Exbio, Vestec, Czech Republic). Cells were harvested with TrypLE™ Express solution, washed with DPBS supplemented with 10% FBS, and finally counted on automated cell counter Countess™ (Invitrogen, Waltham, MA, USA). One million of the cells were resuspended in 1 mLof 10% FBS solution in DPBS and incubated with adequate antibodies for 45 min in the refrigerator. After incubation, cells were fixed with 4% paraformaldehyde (PFA) for 20 min and finally rinsed 2 times with DPBS. Cells were analyzed on a tabletop flow cytometer (Partec, Munster, Germany) and results were processed by software (FloMax 2.82, Partec, Munster, Germany).

2.4.2. Multilineage Differentiation Capacity

To evaluate the stemness characteristics of SCAP, their potential of differentiation into multiple lineages (osteo-, chondro- and adipo-) was tested. Cells were seeded onto 6-well plates either on PET alone or on PET coated with LPEG film, at density of $5 \times 10^3/cm^2$, and grown in the respective differentiation medium, which was changed every 2 days. After the required differentiation period of time elapsed, cells from one well were used for RNA isolation for gene expression analysis.

Osteo-Differentiation

After 28 days of culturing in osteo-differentiation medium (StemPro™ Osteogenesis Differentiation Kit, Thermo Fisher Scientific, Waltham, MA, USA) according to manufacturers' recommendations, cells were subjected to histological staining method using Alizarin Red S, as previously described [34]. Briefly, after rinsing with DPBS and fixating with 4% PFA for 30 min, cells were stained with 2% Alizarin Red S (Centrohem, Belgrade, Serbia) solution, at pH 4.2. After 30 min of incubation, dye was removed, and cells were rinsed twice with distilled water. Stained cultures were observed using inverted light microscopy (Primovert, Zeiss, Oberkochen, Germany) and photographed.

Chondro-Differentiation

For the chondro-induction, cells were seeded in a form of micromass at total number of 1.5×10^6 and grown on 6-well plates in commercially available chondrogenesis media (StemPro™ Chondrogenesis Differentiation Kit, Thermo Fisher Scientific, Waltham, MA, USA) for 21 days. Chondrogenesis was confirmed by 0.1% solution Safranin O (Centrohem, Belgrade, Serbia) positive staining. Stained cells were observed using inverted light microscopy and photographed.

Adipo-Differentiation

Adipogenic stimulation lasted 28 days in commercially available adipogenesis media (StemPro™ Adipogenesis Differentiation Kit, Thermo Fisher Scientific, Waltham, MA, USA) at seeding density of 1×10^4 cells/cm^2 onto 6-well plates. In order to confirm adipo-differentiation, Oil Red O (Centrohem, Belgrade, Serbia) staining was used to visualize intracellular lipid accumulation as lipid vacuoles. Stained cells were observed using inverted light microscopy and photographed.

2.5. LPEG Neuro-Induction

To induce neurogenic differentiation, cells (1.5×10^5) were seeded onto T-25 tissue culture flasks in standard culture medium. After 24 h, neural pre-induction medium and DMEM with 100 mM beta-mercaptoethanol were added, and cells were incubated for 4 h. Then, cell differentiation was continued in a neural induction medium containing recombinant human basic fibroblast growth factor, neural growth factor, and B27 supplement (all from Thermo Fisher Scientific, Waltham, MA, USA) in DMEM either on PET alone or on PET coated with LPEG film. After 7 days of cultivation, cell morphology was observed under inverted microscope. Control cells were incubated in standard culture medium.

2.6. Cell Morphology Analysis Following LPEG Neuro-Induction

2.6.1. Light Microscopy

Cell morphology was observed under inverted microscope (Primovert, Zeiss, Oberkochen, Germany) and photographed. Between days 3 and 7 of neurogenic culture, the cells showed a transition from fibroblast-like to neuron-like cell bodies with long processes, suggesting that the stem cells differentiated into neurons/neuron-like cells. At that point they were subjected to RNA isolation, gene expression and immunocytochemistry analysis. In addition, the growth and morphology of the cells during 5 days of LPEG neuro-induction was recorded with CytoSMART Lux 2 camera (CytoSmart Technologies BV, Eindhoven, The Netherlands).

2.6.2. Confocal Microscopy

For the immunocytochemical analyses, cells were seeded onto 25 mm diameter round glass coverslips at density of $5 \times 10^3/cm^2$ and subjected to neuro-differentiation protocol as described. On the 7th day of neural induction, cells were rinsed 3 times in DPBS, fixed with 4% PFA solution for 20 min, rinsed three times with DPBS and incubated at room temperature for 45 min in blocking and permeabilization buffer (10% Bovine serum albumin and 0.1% Triton X-100 in DPBS). For immunofluorescent detection of neuronal cell marker expression, cells were incubated with the following primary antibodies: rabbit anti-β III-tubulin (B3T, 1:400, Cell Signaling, Danvers, MA, USA), rabbit anti-MAP2 (MAP 1:400, Millipore, Germany) and rabbit anti-neuronal nuclei (NeuN, 1:250, Millipore, Taufkirchen, Germany). Primary antibodies were incubated at 4 °C overnight and subsequently washed 3 times with DPBS. Cell samples were incubated with secondary antibodies—donkey anti-mouse Alexa Fluor 488 (1:200, Invitrogen, Waltham, MA, USA), donkey anti-rabbit Alexa Flour 555 (1:200, Invitrogen, Waltham, MA, USA) and donkey anti-rabbit Alexa Flour 657 (1:200, Invitrogen, Waltham, MA, USA) for 2 h in dark at room temperature. Cells were washed 3 times in DPBS and stained with 4-, 6- diamidino- 2-phenylindole (1:4000, DAPI, Molecular Probes, Eugene, OR, USA) for 10 min in dark at room temperature. After washing in DPBS cell samples were mounted with Mowiol(Sigma Aldrich, St. Louis, MO, USA) on microscope slides. Immunofluorescence microscopy images were obtained by confocal laser-scanning microscope (LSM 510, Carl Zeiss GmbH, Jena, Germany) equipped with Ar 488 and HeNe 543 and 633 laser lines. Micrographs were analyzed using Fiji-Image J softwarever 1.46 (NIH, Bethesda, MD, USA).

2.6.3. AFM of Neuron-like Cells

For the purposes of atomic force microscopy, cells had to be seeded on SiO_2 slides coated with a 2 × 2 cm graphene monolayer at a concentration of 200 cells in 10 µL of complete growth medium. The slides were placed in the wells of the 6-well plate. One hour after seeding, 740 µL of complete medium was added to the cells. After 24 h from seeding, neuro-differentiation was performed by the protocol described above.

Seven days after neuro-induction, the medium was aspirated from the well, and the plates were washed twice with DPBS, then the cells were fixed with 4% PFA solution for 20 min. Any excess fixation solution was removed by rinsing twice more with DPBS.

The morphology of the obtained cells after LPEG neuro-differentiation was characterized by microscopy on an atomic force microscope, using the same device and experimental conditions as for the graphene film characterization.

2.6.4. SEM of Neuron-like Cells

After neuro-induction, cell morphology was observed by SEM using a high-resolution electron microscope, MIRA3 FEG-SEM (Tescan, Brno—Kohoutovice, Czech Republic), at a voltage acceleration of 20 kV. Cell fixation using the increscent concentrations of ethanol was done as previously described [36]. In preparation, the sample surface was coated with an ultrathin layer of gold using an SC7620 mini atomizer (Quorum Technologies, Laughton, East Sussex, UK) to prevent the accumulation of static field electricity.

2.7. RNA Isolation and Gene Expression

The expression of different markers was assessed by real-time PCR (qPCR) analysis. RNA was isolated using TRIzol Reagent (Thermo Fisher Scientific, Waltham, MA, USA), according to manufacturers' recommendation. Subsequent reverse transcription from 1 µg of total RNA was performed using RevertAid First Strand cDNA Synthesis Kit (Thermo Fisher Scientific, Waltham, MA, USA)in order to obtain cDNA for qPCR analysis. The list of specific primers is given in Table 1. The results obtained from each qPCR run were threshold cycle (Ct) values. The relative expression level was assessed using the ΔΔCt method [37]. The relative mRNA expression levels for each sample were calculated as the ratio between the expression of the gene of interest and the expression of the housekeeping gene (GAPDH).

Table 1. Primers with corresponding sequences used in the study.

Primer Name		Sequences (5′→3′)
Runx2	Forward Reverse	ACAAACAACCACAGAACCACAAGT GTCTCGGTGGCTGGTAGTGA
Col2	Forward Reverse	TTCAGCTATGGAGATGACAATC AGAGTCCTAGAGTGACTGAG
PPARG	Forward Reverse	GCTGTGCAGGAGATCACAGA GGCTCCATAAAGTCACCAA
Ngn2	Forward Reverse	CCTGGAAACCATCTCACTTCA TACCCAAAGCCAAGAAATGC
NF-M	Forward Reverse	TGGGAAATGGCTCGTCATTT CTTCATGGAAACGGCCAA
Nestin	Forward Reverse	AACAGCGACGGAGGTCTCTA TTCTCTTGTCCCGCAGACTT
MAP2	Forward Reverse	AACCCTTTGAGAACACGACA TCTTTCCGTTCATCTGCCA
MASH1	Forward Reverse	CCAGTTGTACTTCAGCACC TGCCACTTTGAGTTTGGAC
GAPDH	Forward Reverse	TCATGACCACAGTCCATGCCATCA CCCTGTTGCTGTAGCCAAATTCGT

2.8. Statistical Analysis

GraphPad Prism ver. 9 was used for the analyses (GraphPad Software, Inc., San Diego, CA, USA). After examination of the distribution normality by Kolmogorov–Smirnov normality test, independent sample T tests were performed. The values are presented as mean ± SD. Statistical significance was set at $p < 0.05$. The experiments were performed in triplicate, repeated at least two times.

3. Results

3.1. Graphene Film Characterization

3.1.1. Raman Spectroscopy of Graphene Film

Raman spectroscopy has been applied to verify the exfoliation of the pristine graphite powder, as bulk material, into few-layer graphene nanosheets. Figure 4 represents the Raman spectra of LPEG thin films and pristine graphite powder as a reference.

D (~1352) and G (~1582) peaks are noted in the same position at both Raman spectra. The changes of shape and Raman shift of 2D peak at Raman spectra of graphene film are evident. A well-defined and sharp shape of the 2D peak, as well as a considerable shift to lower wavenumbers (by 12 cm^{-1}) compared to graphite, are characteristics of a few-layer graphene nanoflakes [24]. D′ peak (~1618 cm^{-1}), visible as the shoulder of G peak in the graphene film, together with D peak, confirms the presence of defects and some amount of

disorder in the graphene lattice. The combinations of the main peaks can be also observed: D + D′ (~2939 cm^{-1}) and D + D″ (~2452 cm^{-1}), where the D″ peak is known as a weak defect induced one phonon process.

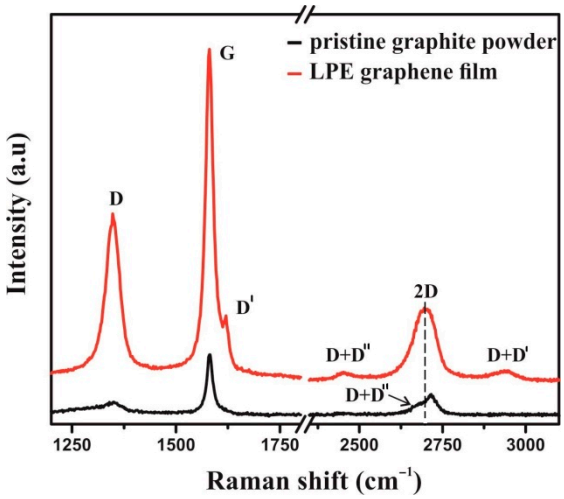

Figure 4. Raman spectrum of LPE graphene film (red line) and pristine graphite powder (black line).

3.1.2. SEM Characterization of Graphene Film

Information about the morphology and film structure was obtained by SEM (Figure 5). The overlapping of the graphene nanosheets and the formation of a closed packed film can be noticed in Figure 5a. Based on the measurement of lateral size, the average diameter of graphene nanosheets was estimated to be in the range of 125 ± 10 nm (Figure 5b).

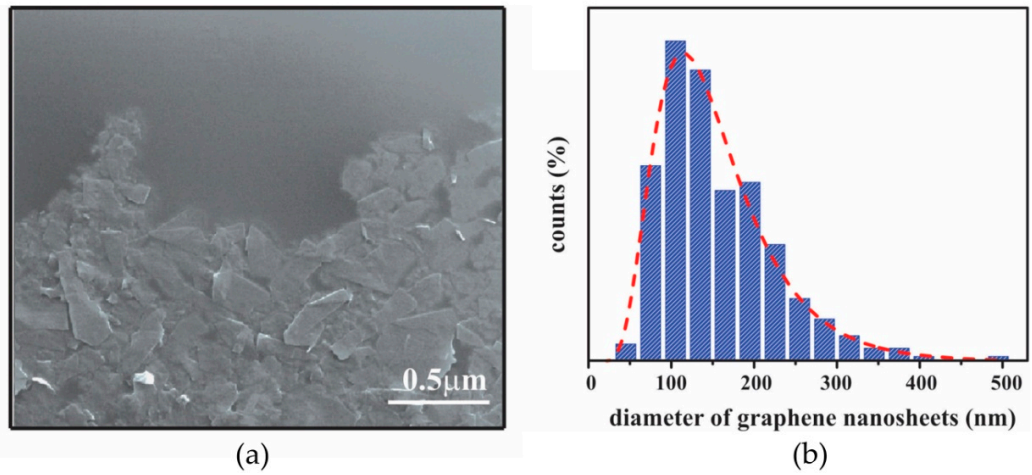

Figure 5. (**a**) SEM image of graphene film; (**b**) Histograms of lateral size of graphene nanosheets obtained from six 3 × 3 μm^2 SEM images (~1800 flakes); The red dashed line represents a log-normal fit.

3.1.3. AFM Characterization of Graphene Film

AFM scans of graphene film along with their characteristics are given in Figure 6. Both 2D (a) and 3D (b) images are shown for a scan area of 20 × 20 μm (512 × 512 lines), as well as for a scan area of 5 × 5 μm—2D image (c), 3D image (d) and phase image (e). Height distribution for the area of 20 × 20 μm and average height profile across the film are given in Figure 6f,g, respectively.

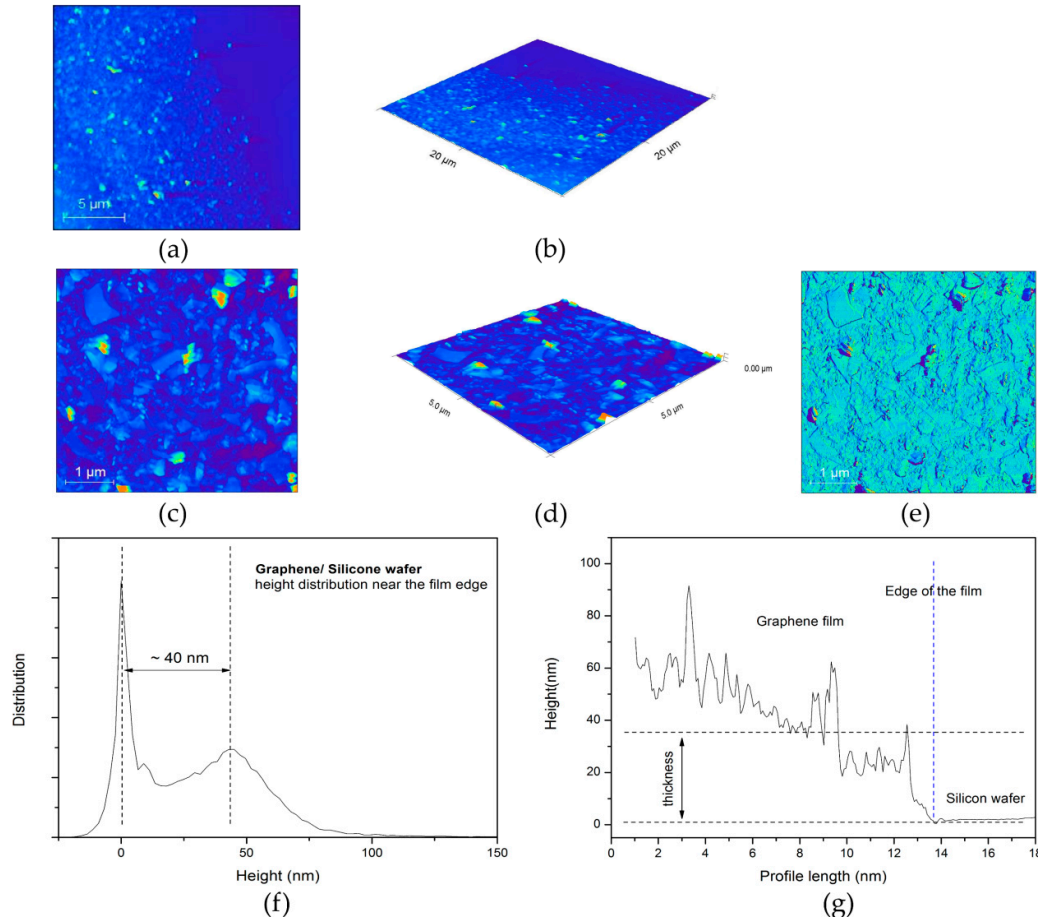

Figure 6. Graphene film near the edge. (**a**) 2D and (**b**) 3D image of the scan area 20 × 20 µm; (**c**) 2D, (**d**) 3D and (**e**) phase image of the scan area 5 × 5 µm; Thickness of graphene film. (**f**) Height distribution near the edge of the film measured for the area 20 × 20 µm and (**g**) average height profile across the edge of the film.

3.2. SCAP Characterization

3.2.1. Flow Cytometry Analysis

Flowcytometry analyses were performed on P5 (fifth passage) stem cell from apical papilla. Flowcytometry revealed the expression of mesenchymal stem cell markers CD73, CD90 and CD105 (99%, 91.3% and 96%, respectively), and the absence of hematopoietic markers CD34 (0.34%) and CD45 (0.01%).

3.2.2. Multilineage Differentiation Capacity

Alizarin Red S staining of mineralized nodules around cells confirmed osteogenic differentiation (Figure 7a); the presence of Safranin O clusters of proteoglycans characteristic for cartilage cells confirmed chondro-differentiation (Figure 7b); the presence of Oil Red O staining was indicative of intracellular lipid accumulation (Figure 7c). In the control group (non-induced cells) there were no stained cells (Figure 7d).

3.2.3. Gene Expression Analysis of Multilineage Differentiation

Real-time PCR analysis of gene expression confirmed successful SCAP differentiation, both when cells were grown on graphene film and when they were grown on PET only (control), thus confirming SCAP stemness. Differentiated cells grown on graphene film showed several times higher expression of Runx2—marker of bone tissue (9.59-fold increase), Col2—marker of cartilage tissue (62.90-fold increase) and PPARG—marker of

adipose tissue (17.48-fold increase) compared to the control group (Figure 8), pointing to the positive effect of graphene in terms of its multilineage induction capacity.

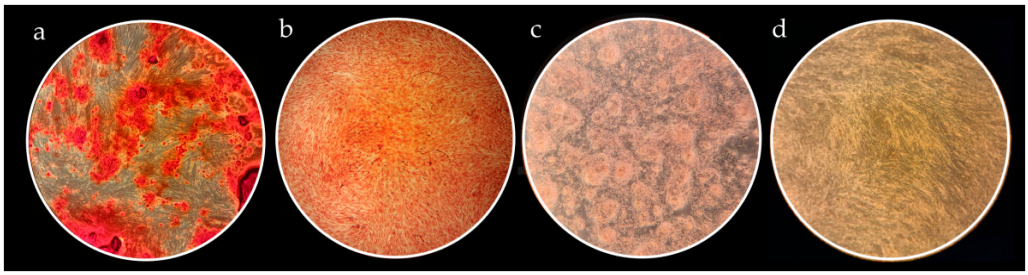

Figure 7. Histological evaluation ofSCAP multilineage differentiation capacity. All micrographs were taken at 40× magnification. (**a**) Alizarin Red S staining of calcium deposits showing osteogenic potential of SCAP; (**b**) Safranin O staining of proteoglycan aggregates evidencing successful SCAP chondrogenic potential; (**c**) Oil Red O positive staining of intracellular lipid droplets as a sign of SCAP adipogenicdifferention; (**d**) Representative image of unstained controls.

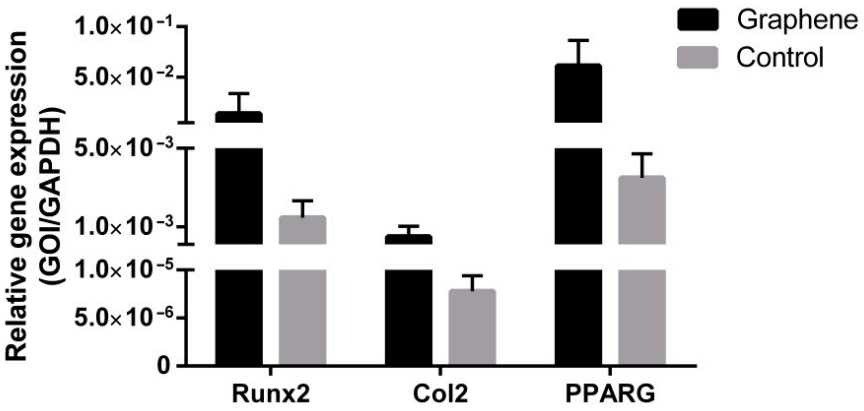

Figure 8. Gene expression evaluation of SCAP osteogenic (Runx2), chondrogenic (Col2) and adipogenic (PPARG) differentiation potential.

3.3. LPEG Neuro-Induction of SCAP

3.3.1. Light Microscopy

After 3–5 days of neuro-induction, cells grown on LPEG film reshaped into polygonal structures with long, slender cytoplasmatic processes that were mainly in contact with adjacent cells. Representative light microscopy images of those neuron-like cells are given in Figure 9a–c. While SCAPs on LPEG film gradually changed their morphology into multipolar cells, similar to neurons, cells grown on PET showed minor changes in cell shape (Figure 9d). The growth and morphology of cells during LPEG film neuro-induction were recorded with a CytoSMART Lux 2 camera (CytoSmart Technologies BV, Eindhoven, the Netherlands). A graphical representation of the time-dependent extension of cytoplasmic processes (in µm) is shown in Figure 9e, along with 6 htime frames that were extracted from the video (Figure 9f). The real-time recording of cell morphology changes can be also viewed (Video S1).

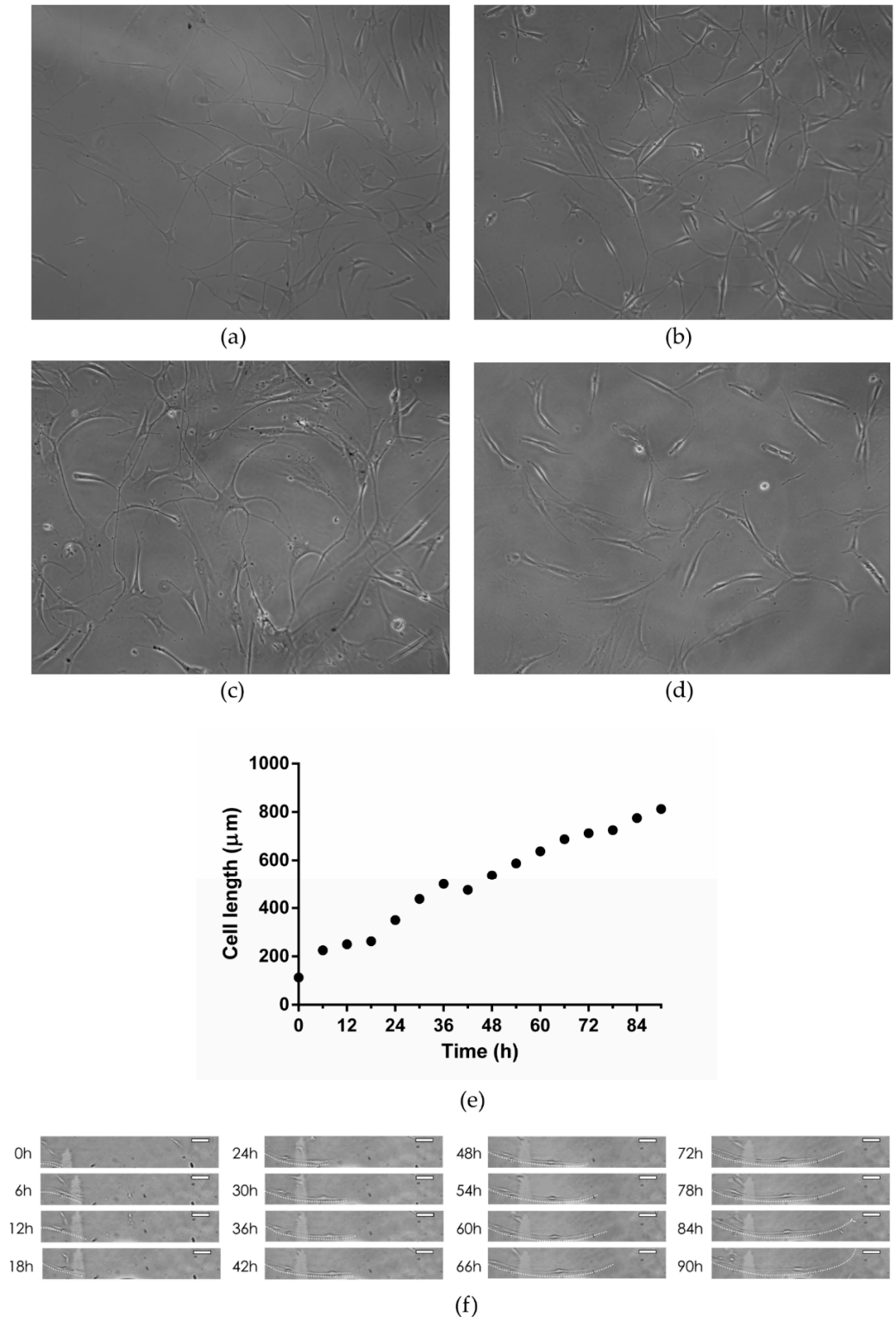

Figure 9. (**a**–**c**) Representative light micrographs of SCAP grown on graphene film; (**d**) Representative light micrograph of SCAP grown on PET; (**e**) Time-dependent changes in major axis length of SCAP grown on graphene film; (**f**) Time-lapse light micrographs of SCAP grown on graphene film (dotted white line represents cell extension pathway; white scale bar represents 100 μm).

3.3.2. Confocal Microscopy

Confocal microscopy showed the increased expression of three major neural cell markers (NeuN, MAP2 and β-3 tubulin) in SCAPs grown on graphene, compared to cells grown on PET alone (control) (Figure 10).

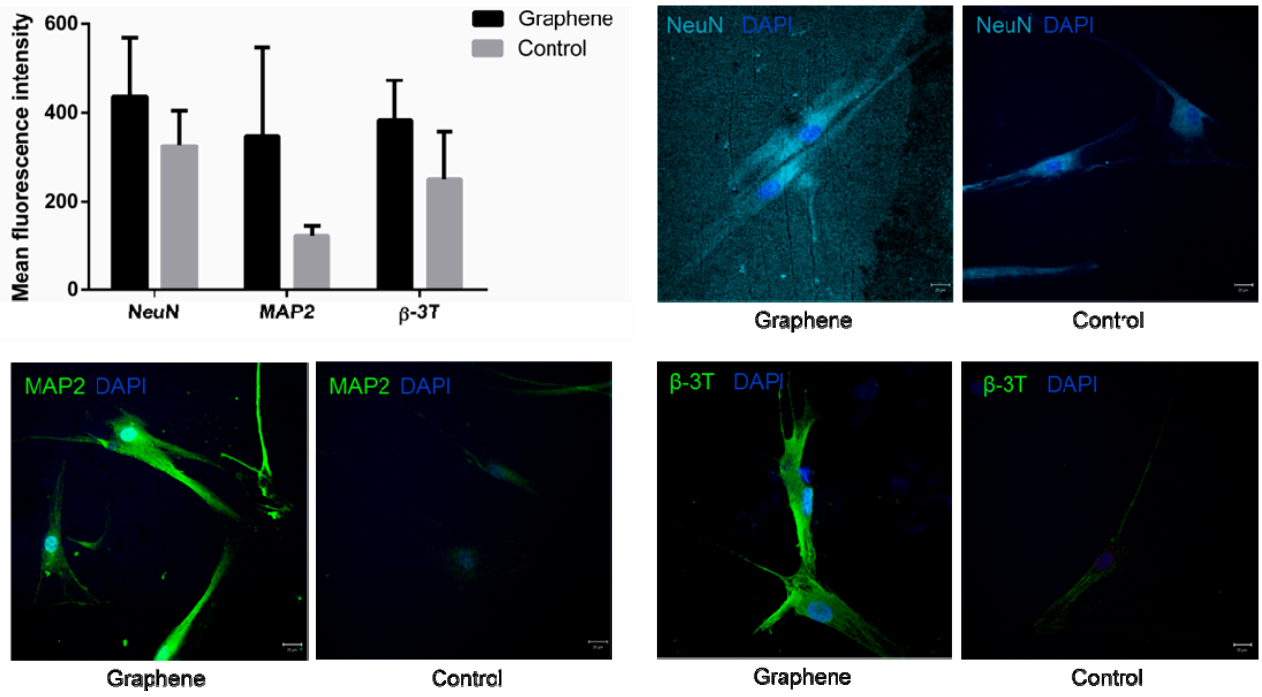

Figure 10. Mean fluorescence intensities and laser confocal micrographs of SCAP immunolabeled for neuronal markers NeuN, MAP2 and β3-tubulin (nuclei are labeled with DAPI).

3.3.3. AFM of Neuron-like Cells

Atomic force microscopy (AFM) revealed subtle surface topography and morphological differences between stem cells grown on graphene film compared to those placed over PET. SCAP grown on graphene were polygonal in shape (Figure 11a,b) with multiple long-distance, slender cytoplasmatic projections emerging from cell body (Figure 11c,d) compared to the less complex cell morphology of SCAP grown on PET (Figure 11e,f). Note that AFM height panel also revealed numerous globular protrusions on the surface of the cell bodies, which were more present on SCAP grown on graphene.

3.3.4. SEM of Neuron-like Cells

Scanning electron microscopy (SEM) of SCAP grown on graphene film depicted a triangular cell body with long, slender projections (Figure 12a). The endings of these projections were in close proximity or direct contact with cytoplasmatic projections of surrounding cells forming a connected cell population (Figure 12b).

3.3.5. Gene Expression Analysis after LPEG Neuro-Induction

Gene expression analysis of key neural differentiation markers of SCAP grown on LPEG film and control material is presented in Figure 13. All examined markers showed higher expression in cells grown on graphene film compared to those on non-coated PET (control).

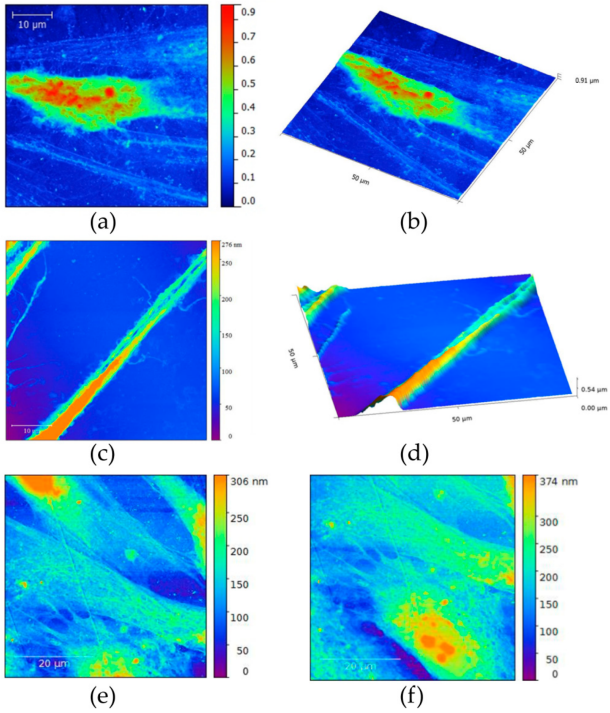

Figure 11. (**a**,**b**) Atomic force micrographs of SCAP grown on graphene film; (**c**,**d**) Long, slender projections of SCAP cell membrane covering graphene film; (**e**,**f**) AFMs of control SCAP grown on PET (control).

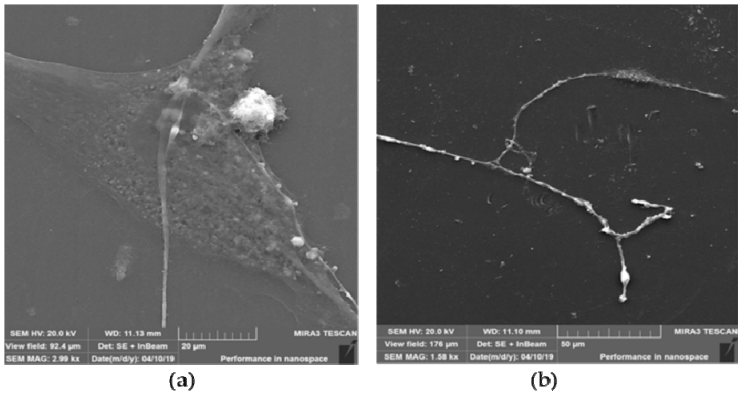

Figure 12. SEM of SCAP grown on graphene film. (**a**) Triangular cell body with arising long-distance membrane projections; (**b**) Slender cell projections synapsing with adjacent cell.

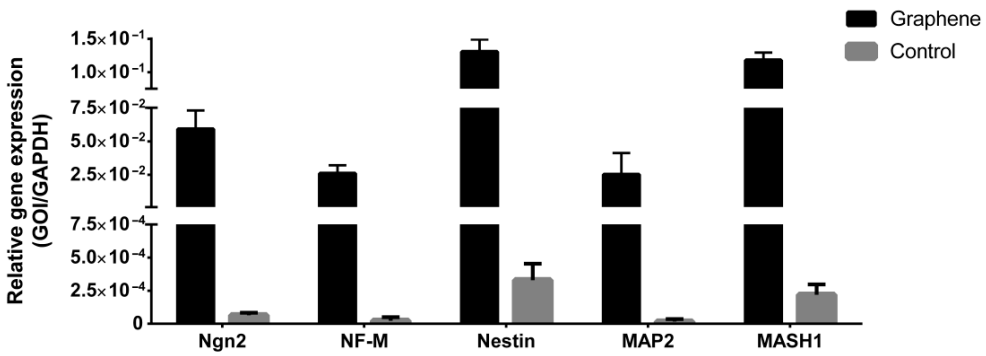

Figure 13. Gene expression analyses of neuronal markers of SCAP grown on graphene film and PET (control).

4. Discussion

Many dental tissues are precious niches of mesenchymal stem cells that are becoming increasingly appealing in regenerative medicine due to their easy accessibility and lack of health risks for the donor. They are especially attractive for the field of neuro-regeneration given that they originate from the neural crest and possess the capacity of differentiation into diverse neural cell types. Apical papilla, the soft tissue at the apex of a not fully formed tooth, contains a very high percentage of MSCs characterized by great plasticity, proliferation rate and differentiation ability. Previous studies, based on immunophenotyping, gene expression analyses, and patch clamping, have reported that SCAP grown under neural inductive conditions could give rise to a variety of neural cell phenotypes, from neuroprogenitors to mature neurons [10,34].

The number of novel materials used as cell carriers/scaffolds, tested for tissue engineering application, is constantly increasing, especially in the field of neuro-repair and regeneration. Great emphasis has been put on carbon nanostructured scaffolds that may display suitable characteristics for neural differentiation [13,34,38,39]. Graphene nanomaterials are carbon crystal allotropes with a two-dimensional structure and, according to data from the literature, have proven to be an excellent nanomaterial for neurodifferentiation due to their unique organization, chemical stability, exceptional mechanical properties, bactericidal potential, and biocompatibility [40,41]. This monoatomic layer of carbon shows the ability to absorb growth factors and exhibits electrical conductivity, which is of particular interest for the field of neuroscience. For instance, Lee et al. have convincingly demonstrated, on a neuroblastoma cell line, that graphene substrate enhanced neurite outgrowth, both in terms of length and number [42]. Rodrigues-Losada et al. also showed that different graphene materials (graphene oxide and reduced derivatives) promoted the differentiation, proliferation and maturation of dopaminergic neurons [43]. Importantly, graphene-based materials also exert stimulating effect on cell differentiation towards neurons rather than glial cells [44]. In neural regeneration, the induction of stem cell differentiation in favor of neurons against glial cells is highly desirable, making graphene-based nanomaterials a promising agent in neuroregenerative therapies. In addition to graphene oxide, the most studied graphene nanomaterial, there are other forms of graphene that are non-toxic and biocompatible, such as fully reduced or partially reduced graphene oxide, in the form of powder or film, but their positive effects in terms of neurodifferentiation have not yet been sufficiently investigated. This is the case with liquid-phase exfoliated graphene (LPEG) film that was the subject of this research. In the present study, Raman spectroscopy has been applied to verify the exfoliation of the pristine graphite powder, as bulk material, into graphene nanosheets. Indeed, the obtained closed packed film was made of few-layer graphene nanoflakes, as seen on SEM. The changes of shape and Raman shift of the 2D peak at Raman spectra of graphene film are evident. A well-defined and sharp shape of the 2D peak as well as a considerable shift to lower wave number compared to graphite are characteristics of few-layer graphene nanoflakes [45]. Edge defects, as the dominant type of defect in graphene film, are the result of the cavitation process at the liquid phase exfoliated technique [46]. Generally, the Raman spectra as well as the average diameter of the nanosheets and their height were in agreement with some previous reports [47].

In the present study, the mandatory characterization of SCAP cultures has shown a highly predominant presence of cells displaying mesenchymal stem cell markers (between 91 and 99% of cells in the culture expressed a given mesenchymal marker). Concomitantly, a negligible percentage of cells expressed hematopoietic stem cell markers (only 0.01% and 0.34% of cells expressed CD45 and CD34, respectively), as determined by flowcytometry, pointing to the fact that cell cultures contained principally MSCs. Similarly, stemness characterization by means of multiple lineages induction showed a successful osteo-, chondro- and adipo-differentiation of SCAPs. The specific osteo-, chondro- and adipo cellular phenotypes, assessed by appropriate staining procedures, were also confirmed by high mRNA levels of selected markers (Runx2, Col2 and PPARG, for osteo-, chondro- and adipo-differentiation, respectively). These findings are in general agreement with some

previous reports [48–50]. Interestingly, the three examined processes of differentiation also appeared to be enhanced in the presence of graphene (especially chondrogenesis) but more markers specific for osteo-, chondro- and adipo- lineages should be evaluated in order to confirm that positive effect of graphene film. This is in line with some previous studies. Namely, it was found that graphene derivatives exhibit great stimulatory effects on adipogenesis and osteogenesis [19,51–53], pointing to the possibility of their use in composite tissue cultures when more than one cell type is needed. This is of utmost importance in regenerative medicine and dentistry when huge defects require complex reconstructions. The classical example is the surgical removal of a portion of maxilla or mandible in cases of oral cancer, resulting in massive bone, muscle and nerve defects, which necessitate multiple tissues' replacement.

Regarding neurogenesis, the present study showed for the first time that LPEG films can have strong stimulatory effects on SCAPs' induction towards neural lineage. Namely, cells cultured in neurodifferentiation medium on graphene film demonstrated increased levels of all neural markers (studied either by confocal microscopy or by quantitative PCR), compared to cells grown in neurodifferentiation medium only. The levels of ngn-2, an inhibitor of glial cell transcription factor, were very high, indicative of LPEG capacity to suppress gliogenesis, thus favoring neurogenesis [54]. Gene expression of Nestin, a marker of neuroepithelial and radial cells, was, as well, increased in cells grown on graphene film compared to those seeded over the non-coated substrate. This protein has a crucial role in assembling and disassembling intermediate filaments and thus maintains the structure and regulates the growth of developing neural cells [55]. Similarly, a higher expression of Mash-1, a marker of intermediate progenitors, was also noted. Mash-1, as one of the early markers that determine cellular fate, is involved in the differentiation of neuroblasts, as well as in cell protection mechanisms that prevent cell damage and apoptosis. βIII-tubulin, a neuronal microtubule protein that is particularly expressed during neurogenesis and is thought to be responsible for axon growth, was upregulated in the presence of graphene. The level of MAP2, a cytoskeletal element essential for the binding and stabilization of neuronal microtubules with major impact on neuronal development, was also higher in cells grown on graphene film [56]. Another neural marker of mature neurons that has never been found in glial cells—NeuN—was more expressed in SCAP stimulated by LPEG compared to the control condition. This marker was detected, both in the cell nucleus and perinuclear cytoplasm. Unlike the nuclear form, which binds to DNA and most probably has an important role in the regulation of neurogenesis, the role of the cytoplasmatic variant is still unclear. It is assumed that, together with Synapsin I, cytoplasmaticNeuN regulates the mobility of synaptic vesicles and release of neurotransmitters, thus playing a potential role in synaptogenesis and establishing neural circuits [57]. The last examined, final stage marker of neural development, along with MAP2 and NeuN, was Neurofilament Medium (NF-M) and, again, its expression was higher in cells grown on graphene. In agreement with our findings, which showed positive effects of graphene film on neurogenesis, a previous study that examined several types of graphene material established that the morphology of the film and the species of graphene influenced the behavior of neurons, but generally film species exhibited higher biocompatibility than powder materials [43]. Our results support the central concept of graphene substrates' beneficial effects on the neural induction of several types of mesenchymal stem cells [58].

Future studies testing the neuroinductive capacity of graphene should use films with different physico-chemical characteristics along with other stem cells of dental origin, such as pulp or follicle cells, combined with different culture media. In addition, markers' quantification at the protein level should rely on ELISA or Westernblot analyses as more precise than immunofluorescence quantification, thus overcoming some limitations of this study.

5. Conclusions

The predisposition of SCAPs to differentiate toward neural lineages, as well as the neuroinductive properties of graphene film, should warrant further studies of dental stem cells in conjunction with this nanomaterial, with the aim of finding an optimal solution for autologous neuroregenerative therapy.

Supplementary Materials: The following supporting information can be downloaded at: https://www.mdpi.com/article/10.3390/nano12183116/s1, Video S1: Time-dependent changes in morphology of SCAP grown on LPEG film.

Author Contributions: Conceptualization, J.S. and J.M.; methodology, J.S., R.P. and J.M.; validation, J.M.; formal analysis, J.S., B.T., M.L. and M.M.M.; investigation, J.S., B.T., M.L., M.M.M., M.P. and J.V.; resources, R.P. and J.M.; data curation, J.S., M.P. and J.V.; writing—original draft preparation, J.S.; writing—review and editing, M.L., M.M.M. and J.M.; visualization, B.T. and M.L.; supervision, J.M.; project administration, J.M.; funding acquisition, J.M. All authors have read and agreed to the published version of the manuscript.

Funding: This research was supported by the Ministry of Education, Science and Technological Development of the Republic of Serbia grant number 451-03-9/2021-14/200129 and by the Science Fund of the Republic of Serbia, #GRANT No 7750038, ORAL CANCER—NEW APPROACHES IN PREVENTION, CONTROL AND POST-OPERATIVE REGENERATION—AN IN VIVO STUDY—ORCA-PCR.

Institutional Review Board Statement: The study was conducted in accordance with the Declaration of Helsinki, and approved by the Ethics Committee of the School of Dental Medicine, University of Belgrade (No 36/19, 19.04.2016).

Informed Consent Statement: Informed consent was obtained from all subjects involved in the study.

Data Availability Statement: Not applicable.

Acknowledgments: We extend our appreciation to Djordje Miljkovic from the Institute of Biological Research Sinisa Stankovic, University of Belgrade, for the flowcytometry analyses.

Conflicts of Interest: The authors declare no conflict of interest. The funders had no role in the design of the study; in the collection, analyses, or interpretation of data; in the writing of the manuscript; or in the decision to publish the results.

References

1. Mitrečić, D.; Hribljan, V.; Jagečić, D.; Isaković, J.; Lamberto, F.; Horánszky, A.; Zana, M.; Foldes, G.; Zavan, B.; Pivoriūnas, A.; et al. Regenerative Neurology and Regenerative Cardiology: Shared Hurdles and Achievements. *Int. J. Mol. Sci.* **2022**, *23*, 855. [CrossRef]
2. Liu, A.; Long, Y.; Li, J.; Gu, L.; Karim, A.; Wang, X.; Gibson, A.L.F. Accelerated complete human skin architecture restoration after wounding by nanogenerator-driven electrostimulation. *J. Nanobiotechnol.* **2021**, *19*, 280. [CrossRef] [PubMed]
3. Long, Y.; Wei, H.; Li, J.; Yao, G.; Yu, B.; Ni, D.; Gibson, A.L.; Lan, X.; Jiang, Y.; Cai, W.; et al. Effective Wound Healing Enabled by Discrete Alternative Electric Fields from Wearable Nanogenerators. *ACS Nano* **2018**, *12*, 12533–12540. [CrossRef] [PubMed]
4. Vishwakarma, A.; Sharpe, P.; Shi, S.; Ramalingam, M. (Eds.) *Stem Cell Biology and Tissue Engineering in Dental Sciences*; Elsevier: Amsterdam, The Netherlands, 2014.
5. Egusa, H.; Iida, K.; Kobayashi, M.; Lin, T.Y.; Zhu, M.; Zuk, P.A.; Wang, C.J.; Thakor, D.K.; Hedrick, M.H.; Nishimura, I. Downregulation of extracellular matrix-related gene clusters during osteogenic differentiation of human bone marrow- and adipose tissue-derived stromal cells. *Tissue Eng.* **2007**, *13*, 2589–2600. [CrossRef] [PubMed]
6. Ding, D.C.; Shyu, W.C.; Lin, S.Z. Mesenchymal stem cells. *Cell Transplant.* **2011**, *20*, 5–14. [CrossRef]
7. Fernandes, K.J.; McKenzie, I.A.; Mill, P.; Smith, K.M.; Akhavan, M.; Barnabé-Heider, F.; Biernaskie, J.; Junek, A.; Kobayashi, N.R.; Toma, J.G.; et al. A dermal niche for multipotent adult skin-derived precursor cells. *Nat. Cell Biol.* **2004**, *6*, 1082–1093. [CrossRef]
8. Sonoyama, W.; Liu, Y.; Fang, D.; Yamaza, T.; Seo, B.M.; Zhang, C.; Liu, H.; Gronthos, S.; Wang, C.Y.; Wang, S.; et al. Mesenchymal stem cell-mediated functional tooth regeneration in swine. *PLoS ONE* **2006**, *1*, e79. [CrossRef]
9. Huang, G.T.; Sonoyama, W.; Liu, Y.; Liu, H.; Wang, S.; Shi, S. The hidden treasure in apical papilla: The potential role in pulp/dentin regeneration and bioroot engineering. *J. Endod.* **2008**, *34*, 645–651. [CrossRef]
10. Abe, S.; Yamaguchi, S.; Amagasa, T. Multilineage Cells from Apical Pulp of Human Tooth with Immature Apex. *Oral. Sci. Int.* **2007**, *4*, 45–48. [CrossRef]

11. Germain, L.; De Berdt, P.; Vanacker, J.; Leprince, J.; Diogenes, A.; Jacobs, D.; Vandermeulen, G.; Bouzin, C.; Préat, V.; Dupont-Gillain, C.; et al. Fibrin hydrogels to deliver dental stem cells of the apical papilla for regenerative medicine. *Regen. Med.* **2015**, *10*, 153–167. [CrossRef]
12. Vanacker, J.; Viswanath, A.; De Berdt, P.; Everard, A.; Cani, P.D.; Bouzin, C.; Feron, O.; Diogenes, A.; Leprince, J.G.; des Rieux, A. Hypoxia modulates the differentiation potential of stem cells of the apical papilla. *J. Endod.* **2014**, *40*, 1410–1418. [CrossRef] [PubMed]
13. Wang, Y.; Li, Z.; Wang, J.; Li, J.; Lin, Y. Graphene and graphene oxide: Biofunctionalization and applications in biotechnology. *Trends Biotechnol.* **2011**, *29*, 205–212. [CrossRef] [PubMed]
14. Lee, W.C.; Lim, C.H.; Shi, H.; Tang, L.A.; Wang, Y.; Lim, C.T.; Loh, K.P. Origin of enhanced stem cell growth and differentiation on graphene and graphene oxide. *ACS Nano* **2011**, *5*, 7334–7341. [CrossRef] [PubMed]
15. La, W.G.; Park, S.; Yoon, H.H.; Jeong, G.J.; Lee, T.J.; Bhang, S.H.; Han, J.Y.; Char, K.; Kim, B.S. Delivery of a therapeutic protein for bone regeneration from a substrate coated with graphene oxide. *Small* **2013**, *9*, 4051–4060. [CrossRef] [PubMed]
16. Lee, Y.J.; Seo, T.H.; Lee, S.; Jang, W.; Kim, M.J.; Sung, J.S. Neuronal differentiation of human mesenchymal stem cells in response to the domain size of graphene substrates. *J. Biomed. Mater. Res. A* **2018**, *106*, 43–51. [CrossRef]
17. Mousavi, S.M.; Yousefi, K.; Hashemi, S.A.; Afsa, M.; Bahrani, S.; Gholami, A.; Ghahramani, Y.; Alizadeh, A.; Chiang, W.H. Renewable Carbon Nanomaterials: Novel Resources for Dental Tissue Engineering. *Nanomaterials* **2021**, *11*, 2800. [CrossRef]
18. Bressan, E.; Ferroni, L.; Gardin, C.; Sbricoli, L.; Gobbato, L.; Ludovichetti, F.S.; Tocco, I.; Carraro, A.; Piattelli, A.; Zavan, B. Graphene based scaffolds effects on stem cells commitment. *J. Transl. Med.* **2014**, *12*, 296. [CrossRef] [PubMed]
19. Park, S.Y.; Park, J.; Sim, S.H.; Sung, M.G.; Kim, K.S.; Hong, B.H.; Hong, S. Enhanced differentiation of human neural stem cells into neurons on graphene. *Adv. Mater.* **2011**, *23*, 263–267. [CrossRef]
20. Wang, Y.; Lee, W.C.; Manga, K.K.; Ang, P.K.; Lu, J.; Liu, Y.P.; Lim, C.T.; Loh, K.P. Fluorinated graphene for promoting neuro-induction of stem cells. *Adv. Mater.* **2012**, *24*, 4285–4290. [CrossRef]
21. Tang, M.; Song, Q.; Li, N.; Jiang, Z.; Huang, R.; Cheng, G. Enhancement of electrical signaling in neural networks on graphene films. *Biomaterials* **2013**, *34*, 6402–6411. [CrossRef]
22. Hong, S.W.; Lee, J.H.; Kang, S.H.; Hwang, E.Y.; Hwang, Y.S.; Lee, M.H.; Han, D.W.; Park, J.C. Enhanced neural cell adhesion and neurite outgrowth on graphene-based biomimetic substrates. *Biomed. Res. Int.* **2014**, *2014*, 212149. [CrossRef] [PubMed]
23. Bellet, P.; Gasparotto, M.; Pressi, S.; Fortunato, A.; Scapin, G.; Mba, M.; Menna, E.; Filippini, F. Graphene-Based Scaffolds for Regenerative Medicine. *Nanomaterials* **2021**, *11*, 404. [CrossRef] [PubMed]
24. Zare, P.; Aleemardani, M.; Seifalian, A.; Bagher, Z.; Seifalian, A.M. Graphene Oxide: Opportunities and Challenges in Biomedicine. *Nanomaterials* **2021**, *11*, 1083. [CrossRef] [PubMed]
25. Sanchez, V.C.; Jachak, A.; Hurt, R.H.; Kane, A.B. Biological interactions of graphene-family nanomaterials: An interdisciplinary review. *Chem. Res. Toxicol.* **2012**, *25*, 15–34. [CrossRef] [PubMed]
26. Kemppainen, J.M.; Hollister, S.J. Tailoring the mechanical properties of 3D-designed poly (glycerol sebacate) scaffolds for cartilage applications. *J. Biomed. Mater. Res. A* **2010**, *94*, 9–18. [CrossRef]
27. Nair, M.; Nancy, D.; Krishnan, A.G.; Anjusree, G.S.; Vadukumpully, S.; Nair, S.V. Graphene oxide nanoflakes incorporated gelatin-hydroxyapatite scaffolds enhance osteogenic differentiation of human mesenchymal stem cells. *Nanotechnology* **2015**, *26*, 161001. [CrossRef]
28. Lee, T.J.; Park, S.; Bhang, S.H.; Yoon, J.K.; Jo, I.; Jeong, G.J.; Hong, B.H.; Kim, B.S. Graphene enhances the cardiomyogenic differentiation of human embryonic stem cells. *Biochem. Biophys. Res. Commun.* **2014**, *452*, 174–180. [CrossRef]
29. Chaudhuri, B.; Bhadra, D.; Moroni, L.; Pramanik, K. Myoblast differentiation of human mesenchymal stem cells on graphene oxide and electrospun graphene oxide-polymer composite fibrous meshes: Importance of graphene oxide conductivity and dielectric constant on their biocompatibility. *Biofabrication* **2015**, *7*, 015009. [CrossRef]
30. Ayán-Varela, M.; Villar-Rodil, S.; Paredes, J.I.; Munuera, J.M.; Pagán, A.; Lozano-Pérez, A.A.; Cenis, J.L.; Martínez-Alonso, A.; Tascón, J.M. Investigating the Dispersion Behavior in Solvents, Biocompatibility, and Use as Support for Highly Efficient Metal Catalysts of Exfoliated Graphitic Carbon Nitride. *ACS Appl. Mater. Interfaces* **2015**, *7*, 24032–24045. [CrossRef]
31. Gopinathan, J.; Quigley, A.F.; Bhattacharyya, A.; Padhye, R.; Kapsa, R.M.; Nayak, R.; Shanks, R.A.; Houshyar, S. Preparation, characterisation, and in vitro evaluation of electrically conducting poly(ε-caprolactone)-based nanocomposite scaffolds using PC12 cells. *J. Biomed. Mater. Res. A* **2016**, *104*, 853–865. [CrossRef]
32. Guazzo, R.; Gardin, C.; Bellin, G.; Sbricoli, L.; Ferroni, L.; Ludovichetti, F.S.; Piattelli, A.; Antoniac, I.; Bressan, E.; Zavan, B. Graphene-Based Nanomaterials for Tissue Engineering in the Dental Field. *Nanomaterials* **2018**, *8*, 349. [CrossRef]
33. Matković, A.; Milošević, I.; Milićević, M.; Tomašević-Ilić, T.; Pešić, J.; Musić, M.; Spasenović, M.; Jovanović, Đ.; Vasić, B.; Deeks, C.; et al. Enhanced sheet conductivity of Langmuir–Blodgett assembled graphene thin films by chemical doping. *2D Mater.* **2016**, *3*, 015002. [CrossRef]
34. Simonovic, J.; Toljic, B.; Nikolic, N.; Peric, M.; Vujin, J.; Panajotovic, R.; Gajic, R.; Bekyarova, E.; Cataldi, A.; Parpura, V.; et al. Differentiation of stem cells from apical papilla into neural lineage using graphene dispersion and single walled carbon nanotubes. *J. Biomed. Mater. Res. A* **2018**, *106*, 2653–2661. [CrossRef] [PubMed]
35. Milošević, I.R.; Vasić, B.; Matković, A.; Vujin, J.; Aškrabić, S.; Kratzer, M.; Griesser, T.; Teichert, C.; Gajić, R. Single-step fabrication and work function engineering of Langmuir-Blodgett assembled few-layer graphene films with Li and Au salts. *Sci. Rep.* **2020**, *10*, 8476. [CrossRef] [PubMed]

36. Shehadat, S.A.; Gorduysus, M.O.; Hamid, S.S.A.; Abdullah, N.A.; Samsudin, A.R.; Ahmad, A. Optimization of scanning electron microscope technique for amniotic membrane investigation: A preliminary study. *Eur. J. Dent.* **2018**, *12*, 574–578. [CrossRef]
37. Livak, K.J.; Schmittgen, T.D. Analysis of relative gene expression data using real-time quantitative PCR and the 2(-Delta Delta C(T)) Method. *Methods* **2001**, *25*, 402–408. [CrossRef]
38. Han, F.; Ma, X.; Zhai, Y.; Cui, L.; Yang, L.; Zhu, Z.; Hao, Y.; Cheng, G. Strategy for Designing a Cell Scaffold to Enable Wireless Electrical Stimulation for Enhanced Neuronal Differentiation of Stem Cells. *Adv. Healthc. Mater.* **2021**, *10*, 2100027. [CrossRef]
39. Madanagopal, T.T.; Tai, Y.K.; Lim, S.H.; Fong, C.H.; Cao, T.; Rosa, V.; Franco-Obregón, A. Pulsed electromagnetic fields synergize with graphene to enhance dental pulp stem cell-derived neurogenesis by selectively targeting TRPC1 channels. *Eur. Cells Mater.* **2021**, *41*, 216–232. [CrossRef]
40. Zhang, Q.; Zhang, Z.; Yin, J. Free-Standing Buckle-Delaminated 2D Organic Nanosheets with Enhanced Mechanical Properties and Multifunctionality. *Adv. Mater. Interfaces* **2019**, *6*, 1900561. [CrossRef]
41. Hung, H.S.; Kung, M.L.; Chen, F.C.; Ke, Y.C.; Shen, C.C.; Yang, Y.C.; Tang, C.M.; Yeh, C.A.; Hsieh, H.H.; Hsu, S.H. Nanogold-Carried Graphene Oxide: Anti-Inflammation and Increased Differentiation Capacity of Mesenchymal Stem Cells. *Nanomaterials* **2021**, *11*, 2046. [CrossRef]
42. Lee, J.S.; Lipatov, A.; Ha, L.; Shekhirev, M.; Andalib, M.N.; Sinitskii, A.; Lim, J.Y. Graphene substrate for inducing neurite outgrowth. *Biochem. Biophys. Res. Commun.* **2015**, *460*, 267–273. [CrossRef] [PubMed]
43. Rodriguez-Losada, N.; Wendelbob, R.; Ocaña, M.C.; Casares, A.D.; Guzman de Villoría, R.; Aguirre Gomez, J.A.; Arraez, M.A.; Gonzalez-Alegre, P.; Medina, M.A.; Arenas, E.; et al. Graphene Oxide and Reduced Derivatives, as Powder or Film Scaffolds, Differentially Promote Dopaminergic Neuron Differentiation and Survival. *Front. Neurosci.* **2020**, *14*, 570409. [CrossRef] [PubMed]
44. Chen, L.; Wang, W.; Lin, Z.; Lu, Y.; Chen, H.; Li, B.; Li, Z.; Xia, H.; Li, L.; Zhang, T. Conducting molybdenum sulfide/graphene oxide/polyvinyl alcohol nanocomposite hydrogel for repairing spinal cord injury. *J. Nanobiotechnol.* **2022**, *20*, 210. [CrossRef] [PubMed]
45. Ferrari, A.C.; Meyer, J.C.; Scardaci, V.; Casiraghi, C.; Lazzeri, M.; Mauri, F.; Piscanec, S.; Jiang, D.; Novoselov, K.S.; Roth, S.; et al. Raman spectrum of graphene and graphene layers. *Phys. Rev. Lett.* **2006**, *97*, 187401. [CrossRef] [PubMed]
46. Bracamonte, M.V.; Lacconi, G.I.; Urreta, S.E.; Torres, L.E.F.F. On the Nature of Defects in Liquid-phase Exfoliated Graphene. *J. Phys. Chem. C* **2014**, *118*, 15455–15459. [CrossRef]
47. Amaro-Gahete, J.; Benítez, A.; Otero, R.; Esquivel, D.; Jiménez-Sanchidrián, C.; Morales, J.; Caballero, Á.; Romero-Salguero, F.J. A Comparative Study of Particle Size Distribution of Graphene Nanosheets Synthesized by an Ultrasound-Assisted Method. *Nanomaterials* **2019**, *9*, 152. [CrossRef]
48. Qu, G.; Li, Y.; Chen, L.; Chen, Q.; Zou, D.; Yang, C.; Zhou, Q. Comparison of Osteogenic Differentiation Potential of Human Dental-Derived Stem Cells Isolated from Dental Pulp, Periodontal Ligament, Dental Follicle, and Alveolar Bone. *Stem. Cells Int.* **2021**, *2021*, 6631905. [CrossRef]
49. Son, Y.B.; Kang, Y.H.; Lee, H.J.; Jang, S.J.; Bharti, D.; Lee, S.L.; Jeon, B.G.; Park, B.W.; Rho, G.J. Evaluation of odonto/osteogenic differentiation potential from different regions derived dental tissue stem cells and effect of 17β-estradiol on efficiency. *BMC Oral. Health.* **2021**, *21*, 15. [CrossRef]
50. Petrescu, N.B.; Jurj, A.; Soriţău, O.; Lucaciu, O.P.; Dirzu, N.; Raduly, L.; Berindan-Neagoe, I.; Cenariu, M.; Boşca, B.A.; Campian, R.S.; et al. Cannabidiol and Vitamin D3 Impact on Osteogenic Differentiation of Human Dental Mesenchymal Stem Cells. *Medicina* **2020**, *56*, 607. [CrossRef]
51. Nayak, T.R.; Andersen, H.; Makam, V.S.; Khaw, C.; Bae, S.; Xu, X.; Ee, P.L.; Ahn, J.H.; Hong, B.H.; Pastorin, G.; et al. Graphene for controlled and accelerated osteogenic differentiation of human mesenchymal stem cells. *ACS Nano* **2011**, *5*, 4670–4678. [CrossRef]
52. Kim, J.; Choi, K.S.; Kim, Y.; Lim, K.T.; Seonwoo, H.; Park, Y.; Kim, D.H.; Choung, P.H.; Cho, C.S.; Kim, S.Y.; et al. Bioactive effects of graphene oxide cell culture substratum on structure and function of human adipose-derived stem cells. *J. Biomed. Mater. Res. A* **2013**, *101*, 3520–3530. [CrossRef] [PubMed]
53. Di Carlo, R.; Zara, S.; Ventrella, A.; Siani, G.; Da Ros, T.; Iezzi, G.; Cataldi, A.; Fontana, A. Covalent Decoration of Cortical Membranes with Graphene Oxide as a Substrate for Dental Pulp Stem Cells. *Nanomaterials* **2019**, *9*, 604. [CrossRef] [PubMed]
54. Heng, B.C.; Jiang, S.; Yi, B.; Gong, T.; Lim, L.W.; Zhang, C. Small molecules enhance neurogenic differentiation of dental-derived adult stem cells. *Arch. Oral. Biol.* **2019**, *102*, 26–38. [CrossRef] [PubMed]
55. Park, D.; Xiang, A.P.; Mao, F.F.; Zhang, L.; Di, C.G.; Liu, X.M.; Shao, Y.; Ma, B.F.; Lee, J.H.; Ha, K.S.; et al. Nestin is required for the proper self-renewal of neural stem cells. *Stem Cells* **2010**, *28*, 2162–2171. [CrossRef] [PubMed]
56. Hochuli, A.H.D.; Senegaglia, A.C.; Selenko, A.H.; Fracaro, L.; Brofman, P.R.S. Dental Pulp from Human Exfoliated Deciduous Teeth-derived Stromal Cells Demonstrated Neuronal Potential: In Vivo and In Vitro Studies. *Curr. Stem. Cell Res. Ther.* **2021**, *16*, 495–506. [CrossRef]
57. Kim, K.S.; Zhao, Y.; Jang, H.; Lee, S.Y.; Kim, J.M.; Kim, K.S.; Ahn, J.H.; Kim, P.; Choi, J.Y.; Hong, B.H. Large-scale pattern growth of graphene films for stretchable transparent electrodes. *Nature* **2009**, *457*, 706–710. [CrossRef]
58. Reddy, S.; He, L.; Ramakrishana, S.; Luo, H. Graphene nanomaterials for regulating stem cell fate in neurogenesis and their biocompatibility. *Curr. Opin. Biomed. Eng.* **2019**, *10*, 69–78. [CrossRef]

NN23

20th International Conference on Nanosciences & Nanotechnologies

BOOK OF ABSTRACTS

4-7 July 2023
Porto Palace Conference Center & Hotel
Thessaloniki, Greece

2023

08:00 - 9:00 Registration

9:00-9:30 | **KEYNOTE** | **Chair: L. Tsetseris** | **Room: Dock Six I**

Topology and ground states of layers
M. Damnjanovic
University of Belgrade, Serbia

09:30-11:00 Dock Six I	WS2: Computational I Chair: L. Tsetseris	09:30-11:00 Timber Hall II	Graphene II (Joined Session of NN23 & ISFOE23) Chair: A. Di Bartolomeo
9:30-10:00 INVITED	**Topological Carbon Nanotubes as Thouless Adiabatic Pumps** Z. P. Popović[1], M. Damnjanović[2], **I. Milošević**[1] *[1]Facultyof Physics, University of Belgrade, 12 Studentski trg, Belgrade, Serbia* *[2] Serbian Academy of Sciences and Arts, 35 Kneza Mihaila St, Belgrade, Serbia*	9:30-10:00 INVITED	**2D electronics and sensors, towards smart electronic circuits** **G. Deligeorgis**[1,2], F. Iacovella[1], D.M. Kosmidis[1], A. Provias[1,2], N. Armaou[1,2], A.Papadopoulou[1] *1. Inst. of Electronic Structure and Laser (IESL), Foundation for Research and Technology – Hellas (FORTH), Greece* *2. Department of Physics, University of Crete Heraklion 70013, Greece*
10:00-10:30 INVITED	**Tailoring magnetic exchange bias and Curie temperature in Ni-based nanoclusters** M. Bohra[1,2], S. Giaremis[3], V. Singh[1], S. Steinhauer[1], **J. Kioseoglou**[3], P. Grammatikopoulos[1] *[1]Nanoparticles by Design Unit, Okinawa Inst. of Science and Technology Graduate University, , Japan* *[2]Mahindra University École Centrale School of Engineering (MEClndia* *[3]Dept. of Physics, Aristotle University of Thessaloniki, GR-54124 Thessaloniki, Greece*	10:00-10:30 INVITED	**Graphene Oxide: Progress and Surprises** **W.K. Maser**[1], A.M. Benito[2] *Instituto de Carboquímica (ICB-CSIC), E-50018 Zaragoza, Spain*
10:30-11:00 INVITED	**In-silico Design of Polymer-based Nanostructured Materials via Simulations Across Scales and Machine-Learning Algorithms** **V. Harmandaris** *Computation-based Science and Technology Research Center, The Cyprus Inst., 2121 Nicosia, Cyprus, & Department of Mathematics and Applied Mathematics, University of Crete, GR-71409, & IACM FORTH, GR-71110 Heraklion, Crete, Greece.*	10:30-10:45	**Laser-assisted high-quality graphene-like structures for energy storage applications** **M. Athanasiou**[1], N. Samartzis[1,2], K. Bhorkar[1], V. Dracopoulos[1], T. Ioannides[1], S. N. Yannopoulos[1] *[1] Foundation for Research and Technology Hellas – Inst. of Chemical Engineering Sciences (FORTH/ICE-HT), P.O. Box 1414, GR-26504, Rio-Patras, Greece* *[2] Dept. of Physics, University of Patras, GR-26504, Rio-Patras, Greece*
		10:45-11:00	**Effects of ambient humidity on composite graphene-thymine and graphene-lipid thin films as a platform for molecular sensing** **R. Panajotović[1],** J. Vujin[1], M. Vorokhta[2], I. Khalakhan[2], I. Milošević[1], W. Huang[3], and S. Ptasinska[4] *[1] Lab for 2D materials, Inst. of physics, Serbia* *[2] Dept. of Surface and Plasma Science of the Faculty of Mathematics and Physics, Charles University, Czech Republic,* *[3] Dept. of Chemistry and Biochemistry, University of Notre Dame USA* *[4] Dept. of Physics and Astronomy, University of Notre Dame, USA*

11:00-11:30 Coffee Break
NN23 Poster (SEE POSTER PROGRAMME) – Exhibition-Networking

11:30-13:30 Dock Six I	WS2: Computational II Chair M. Damnjanovic	11:30-13:30 Timber Hall II	WS3: Advanced in Nanobiomaterials Chair: G. Kousoulas
11:30-12:00 INVITED	**Charge transfer and transport in bio-organic wires** **C. Simserides** *Nat. and Kapodistrian University of Athens, Greece*	11:30-12:00 KEYNOTE	**Technology for Bioelectronic Medicine** **G. Malliaras** *University of Cambridge, UK*
12:00-12:30 INVITED	**Safe and Sustainable by Design (SSbD) – a vital challenge for nanoinformatics** **T. Puzyn**[1,2] *[1] University of Gdansk, ul. Bazynskiego 8, 80-309 Gdansk, Poland, [2] QSAR Lab Ltd., Poland*	12:00-12:30 KEYNOTE	**Design of Multi-functional Biomaterials for Advanced Medical Devices: The Intermediate Water Concept** **M. Tanaka,** S. Kobayashi, S. Nishimura, K. Nishida, S. Shiomoto, D. Murakami, T. Anada *Inst. for Materials Chemistry and Engineering, Kyushu University, Japan*
12:30-13:00 INVITED	**Computational studies on the detection of atmospheric radicals** **L. Tsetseris**[1] *Department of Physics, School of Applied Mathematical and Physical Sciences, Nat. Technical University of Athens, GR-15780 Athens, Greece*	12:30-13:00 INVITED	**Vascular remodelling of injured tissues** **T. Mitsiadis** *University of Zurich, Switzerland*
13:00-13:15	**Improving the precision of quantum-chemical calculations by novel embedding scheme including Friedel oscillations** **A. Siklitskaya**[1], J. Pogrebetsky[1], T. Bednarek[1], A. Kubas[1] *[1]Inst. of Chemical Physics Polish Academy of Sciences* *Kasprzaka 44/52 01-224 Warsaw, Poland*	13:00-13:15	**Nanomaterial-loaded polymer coating prevents the *in vitro* growth of *Candida albicans* biofilms on silicone biomaterials** **A. Tsikopoulos**[1], K. Tsikopoulos[1], G. Meroni[2], S. Soukiouroglou[3], A. Chatzimoschou[4], L. Drago[5], S. Triaridis[6], P. Papaioannidou[1] *[1]1st Dept. of Pharmacology, School of Medicine, Faculty of Health Sciences, Aristotle University of Thessaloniki, Greece* *[2]One Health Unit, Dept. of Biomedical, Surgical and Dental Sciences, School of Medicine, University of Milan, Milan, Italy* *[3]Lab of Microbiology, Hippokration General Hospital, Thessaloniki, Greece* *[4]Lab of Infectious Diseases, Hippokration General Hospital, Thessaloniki, Greece* *[5]Lab of Clinical Microbiology & Microbiome, Dept. of Biomedical Sciences for Health, School of Medicine, U. of Milan, Italy* *[6]1st Dept. of Otorhinolaryngology - Head and Neck Surgery, School of Medicine, Faculty of Health Sciences, Aristotle University of Thessaloniki, Thessaloniki, Greece*

Laser-assisted high-quality graphene-like structures for energy storage applications

M. Athanasiou[1], N. Samartzis[1,2], K. Bhorkar[1], V. Dracopoulos[1], T. Ioannides[1], S. N. Yannopoulos[1]

[1] *Foundation for Research and Technology Hellas – Inst. of Chemical Engineering Sciences (FORTH/ICE-HT), Rio-Patras, Greece*

[2] *Dept. of Physics, University of Patras, GR-26504, Rio-Patras, Greece*

Laser-assisted graphitization of suitable carbonaceous precursors to porous graphene-like materials has attracted recently great attention. In contrast to conventional synthesis protocols relying on wet-chemistry or/and high temperature processes, which utilize harmful reagents and inert atmosphere conditions, laser assisted methods rely on the laser-induced decomposition of a carbon-based precursor, to form a porous 3D graphene-like network. Simple, one-step laser-based approaches have been recently employed in our lab for the preparation of high-quality turbostratic graphene-based structures by decomposing a diverse group of precursors including biomass, phenol-based resins and polymers. An interesting approach is the simultaneous irradiation of two different precursors which can impart the final graphene nanohybrids (e.g. metallic and metalloid oxides doping of graphene) with enhanced functionalities (redox or/and pseudo-capacitive behaviour). The use of industrial-type laser sources operating at ambient conditions testify towards a "green and dry" process compatible with additive manufacturing, providing the flexibility to directly fabricate patterned electrodes onto selected substrates. Here, we will present recent results on the production of porous graphene-like structures and nanohybrids arising from the decomposition of various precursors. Their physicochemical characterization revealed that the materials exhibit high sp^2/sp^3 and C/O ratios while their structures are highly crystalline, demonstrating also increased interlayer spacing, i.e. turbostratic arrangement. The graphene-like materials were evaluated as supercapacitor electrodes.

Akcnowledgements: "Authors would like to acknowledge the EU funded project: "*Efficient materials and processes for high-energy supercapacitors for smart textiles and electromobility applications* (EMPHASIS) – 101091997"

Effects of ambient humidity on composite graphene-thymine and graphene-lipid thin films as a platform for molecular sensing

R. Panajotović[1], J. Vujin[1], M. Vorokhta[2], I. Khalakhan[2], I. Milošević[1], W. Huang[3], and S. Ptasinska[4]

[1] *Lab for 2D materials, Inst. of physics, Serbia*

[2] *Dept. of Surface and Plasma Science of the Faculty of Mathematics and Physics, Charles University, Czech Republic*,

[3] *Dept. of Chemistry and Biochemistry, University of Notre Dame USA*

[4] *Dept. of Physics and Astronomy, University of Notre Dame, USA*

The efficiency and accuracy of an electro-chemical and bio-chemical sensor device based on graphene critically depends not only on how well the process of interest is coupled to its properties, but also on the environmental conditions, in particular ambient humidity. Functionalization of graphene with biomolecules proved to be an excellent strategy for graphene-based electrical sensors for proteins, DNA, pesticicides, bacteria, antiobiotics, as well as for heavy metal detection in water and air, due to their high binding affinity to inorganic contaminants. For these applications, a nucleic base thymine (Thy) and various lipids have been used in graphene-based Field-Effect-Transistor (FET) configuration. As both molecules have self-assembling properties, their distribution and molecular organization on the surface will vary depending on the morphology and hydrophilicity of the graphene film. In order to gain an insight into the influence of ambient water from air onto the adsorption of thymine and dipalmitoylphosphatidylcholine (DPPC) on graphene films consisting of nanoflakes, we performed Near-Ambient X-ray Photoelectron Spectroscopy experiments, where pure graphene and its composites with thymine and DPPC were exposed to 1 and 5 mb pure gaseous water in the ultra-high vacuum reaction chamber at room temperature. In addition, we analysed the Raman vibrational spectra of composite thin films and their morphology by Atomic Force Microscopy (AFM) and electron microscopy. We will present the comparison of our data with previous studies on Thy adsorption on single-layer graphene and protein-functionalized graphene nanoparticles in aqueous solution.

.

RAD 7

BOOK OF ABSTRACTS

SEVENTH INTERNATIONAL CONFERENCE ON RADIATION IN VARIOUS FIELDS OF RESEARCH

June 10-14, 2019
Herceg Novi
Montenegro

CEI
CENTRAL EUROPEAN INITIATIVE
30 years

TABLE OF CONTENTS

RAD 7 SEVENTH INTERNATIONAL CONFERENCE ON RADIATION IN VARIOUS FIELDS OF RESEARCH

Effects of water on thin films consisting of biomolecules and 2D-materials

Jasna Vujin[1], Weixin Huang[2], Sylwia Ptasinska[3], Radmila Panajotovic[1]

1 Institute of Physics, Belgrade, Serbia
2 Stanford University, Stanford, United States
3 University of Notre Dame, South Bend, United States

One of the hottest research topics in the field of 2D-materials is the one concerning their heterostructures with biomolecules. They can serve as scaffolds for growing cells, or bio-chemical sensors, for example. The most popular 2D-material, graphene, and transition metal dichalogenides(WS_2) in combination with various biomolecules (lipids, biopolymers, amino acid, protein...) attracted considerable attention as active components of organic electronic devices. A relatively simple and cheap method of producing thin graphene films is from the liquid phase. The ever present question of how water/humidity from air or biomolecule aqueous solution affects the properties of these heterostructures is very difficult to answer because of the complicated interplay between these components.

In our experiment, we first exposed bare graphene and WS_2 thin films to water in the controlled environment. Then we did the same experiment with the lipid layer (DPPC dipalmitoyl-sn-glycero-phosphotidilcholine), by collecting the XPS (X-ray Photo-Electron) spectra. In order to examine electrical properties of such heterostructures in ambient condition, we measured the current-voltage response after the deposition of aqueous solution of amino acids, protein and cell culture. In addition, we collected the information about the topography of our heterostructures and Raman.

RAD 7 SEVENTH INTERNATIONAL CONFERENCE ON RADIATION IN VARIOUS FIELDS OF RESEARCH

Application of 2D-materials in building biomolecular heterostructures

Jasna Vujin[1], Martina Gilić[2], Radmila Panajotović[1]

1 Laboratory for Graphene, Other 2D-Materials and Ordered Nanostructures, Institute of Physics, Belgrade, Serbia
2 Laboratory for Electronic Materials, Institute of Physics, Belgrade, Serbia

A quest for non-toxic, easily produced and inexpensive materials with satisfactory chemical (inertness, resistance to degradation) and physical (mechanical robustness, flexibility) properties, that can be used in combination with biological molecules and cells, was greatly accomplished by the discovery of atomically thin 2D-materials. Their exceptional mechanical and tunable electrical properties offer an excellent base for building various types of bio-chemical sensors, growth of self-assembled bio-membranes, and scaffolds for biological tissue engineering. As the most popular of these materials, graphene has become widely used, in various forms – as nanotubes, nanoflakes, nanopaticles, etc. Others, like MoS_2 and WS_2, have gained their popularity as active elements of biochemical sensors, mostly due to their tunable (semi) conductivity after physi- or chemisorption on their surface. In both conductive (graphene) and semi-conductive (MoS_2 and WS_2) thin films of 2D-materials it is necessary to assess their surface morphology, and the chemical and physical changes in combination with water, and biological molecules, such as aminoacids, proteins, lipids, etc. In order to do this, we used several experimental methods – AFM, KPFM Raman and FT-IR spectroscopy. We used graphene and WS2 thin films for deposition of two different amino acids – cystein, arginine – and sphyngomyelin – playing an important role in neuro-signalling and in the structure of neuron's axon sheath.

Book of abstracts

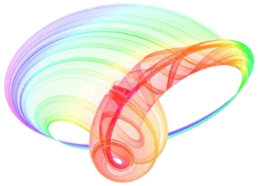

PHOTONICA2019

The Seventh International School and Conference on Photonics, 26 August – 30 August 2019, Belgrade, Serbia

& Machine Learning with Photonics Symposium (ML-Photonica 2019)

& ESUO Regional Workshop

& COST action CA16221

Editors: Milica Matijević, Marko Krstić and Petra Beličev

Belgrade, 2019

ABSTRACTS OF TUTORIAL, KEYNOTE, INVITED LECTURES, PROGRESS REPORTS AND CONTRIBUTED PAPERS

of

The Seventh International School and Conference on Photonics
PHOTONICA2019, 26 August – 30 August 2019, Belgrade, Serbia

and
Machine Learning with Photonics Symposium

and
ESUO Regional Workshop

Editors
Milica Matijević, Marko Krstić and Petra Beličev

Technical Assistance
Danka Stojanović and Goran Gligorić

Publisher
Vinča Institute of Nuclear Sciences
Mike Petrovića Alasa 12-14, P.O. Box 522
11000 Belgrade, Serbia

Printed by
Serbian Academy of Sciences and Arts

Number of copies
300

ISBN 978-86-7306-153-5

Large-scale deposition of self-assembled thin films from liquid phase exfoliated h-BN

T. Tomašević-Ilić[1], Đ. Jovanović[1], R. Panajotović[1], R. Gajić[1] and M. Spasenović[2]
[1]*Graphene Laboratory of the Center for Solid State Physics and New Materials, Institute of Physics, Belgrade, Serbia*
[2]*Center for Microelectronic Technologies, Institute of Chemistry, Technology and Metallurgy, Belgrade, Serbia*
e-mail: ttijana@ipb.ac.rs

Degradation processes, such as exposure to oxygen, humidity, temperature and ultraviolet (UV) illumination makes the intrinsic lifetime of the various optoelectronic devices, such as organic or 2D materials based solar cells, without encapsulation very short [1]. Hexagonal boron nitride (h-BN) is among the most interesting 2D materials, due to its exceptional properties as an inert passivation layer that can protect devices against environmental and chemical effects. A large area, high quality, inexpensive method for depositing thin h-BN has not been reported to date [2]. Here we demonstrate uniform large area h-BN thin films deposited from solution on solid substrates. h-BN was exfoliated from powder using liquid phase exfoliation (LPE) and deposited on a substrate using the Langmuir-Blodgett self-assembly technique (LBSA) [3]. The optical and structural properties of our thin films were characterized with UV-VIS spectrophotometry, Raman spectroscopy, X-ray photoelectron spectroscopy and optical and atomic force microscopy. Our fabrication method results in films with an optical band gap of 5.45 eV, high substrate coverage and an average thickness of 4 nm. The method features uniform deposition over large areas on any kind of solid substrate. Our inexpensive, facile, reproducible and reliable assembly method bridges the gap for use of h-BN as an ultrathin protective coating on various materials that are subjective to molecular degradation.

ACKNOWLEDGMENT: This work is supported by the Serbian MPNTR through Projects OI 171005 and III45018.

REFERENCES

[1] E. Singh, H. S. Nalwa, RSC Advances 5, 73575 (2015).
[2] G. R. Bhimanapati, N. R. Glavin, J. A. Robinson, Semiconduct. Semimet. 95, 101 (2016).
[3] T. Tomašević-Ilić et al., Appl. Surf. Sci. 458, 446 (2018).

Копаоник, 10 – 14.03.2019.
УНИВЕРЗИТЕТ У БЕОГРАДУ
Институт за физику

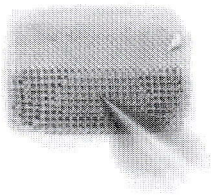

Зборник апстраката

Дванаеста радионица фотонике (2019)

(Конференција)

Book of Abstracts

12th Photonics Workshop

(Conference)

PHOTONICS
CENTER

Institute of Physics
University of Belgrade
Kopaonik, March 10-14, 2019

Дванаеста радионица фотонике (2019)

ЗБОРНИК АПСТРАКАТА

Копаоник 10-14.03.2019.

Издаје:

Институт за физику Београд

За издавача:

Др Александар Богојевић, директор

Уредници:

Др Драган Лукић, др Марина Лекић, др Зоран Грујић

Тираж: 70 primeraka

ISBN 978-86-82441-49-6

Штампа:

NEW IMAGE d.o.o.

Цара Душана 212, Земун, Београд

CIP - Каталогизација у публикацији - Народна библиотека Србије, Београд
535(048)
681.7(048)
66.017/.018(048)
PHOTONICS Workshop (12 ; 2019 ; Kopaonik)
Book of Abstracts / 12th Photonics Workshop, (Conference), Kopaonik, March 10-14, 2019. = Зборник апстраката / Дванаеста радионица фотонике (2019), (Конференција) ; [urednici Dragan Lukić, Marina Lekić, Zoran Grujić]. - Beograd : Institut za fiziku, 2019 (Beograd : New image). - 62
str. : ilustr. ; 25 cm
Tiraž 70. - Registar.
ISBN 978-86-82441-49-6
a) Оптика - Апстракти b) Оптоелектроника - Апстракти c) Технички материјали - Апстракти
COBISS.SR-ID 274585868

Conference program

Sunday, March 10th

16.30 -16.40	Refreshments and Opening ceremony

Chairman: Srđan Antić

16.40 - 17.10	**Branislav Jelenković** Nobel Prize in physics 2018 – Arthur Askin and optical tweezers
17.10 - 17.40	**Dejan Zečević** Contribution of individual synapses on dendritic spines to electrical signaling in single neurons
17.40 – 17.50	Coffee break
17.50 – 18.10	**Goran Isić** Terahertz modulation by Schottky junction in metal-semiconductor-metal microcavities
18.10 – 18.30	**Gulnur Aygun** High-Temperature Operation of THz QCLs for High Power Emission
18.30 – 18.50	**Danka Stojanović** Chiral metamaterial based on twisted closed ring resonators operative in terahertz frequency range

Monday, March 11th

Chairman: Željko Šljivančanin

16.30 - 17.00	**Srđan Antić** Optical recordings of the neuronal electrical activity using genetically encoded voltage indicators (GEVIs)
17.00 - 17.30	**Miroslav Dramićanin** Ways to Read Temperature from Luminescence
17.30 – 17.40	Coffee break
17.40 – 18.10	**Lutfi Ozyuzer** THz Devices and Applications Based on High-T_c Superconductors, Metamaterials and Quantum Cascade Lasers
18.10 – 18.30	**Radmila Panajotović** Spectroscopic insight into the structure of biomolecule-2D-material thin film

Spectroscopic insight into the structure of biomolecule-2D-material thin films

Jasna Vujin and Radmila Panajotović

Institut of Physics, Pregrevica 118, 11080 Belgrade, Serbia

Contact: R.Panajotovic (radmila@ipb.ac.rs)

Abstract. Thin film heterostructures, mostly containing various inorganic materials, have been a hot topic of contemporary research in nanotechnology for the last ten years. Still, many questions about the chemistry and physics of such structures remain, especially those related to their use as electrical devices (FET, for example). Graphene and di-halcogenides (WS_2, MoS_2, etc.), the popular 2D-materials, are widely used as substrates for organic molecules, making part of bio-chemical sensors. The operation and efficiency of these sensing devices depends to a great extent on the chemistry of surfaces and the mutual interaction of the layers.

In our experiments we used spectroscopic methods – FTIR and Raman spectroscopy to get more insight into the chemical aspect of the heterostructures formed of graphene, WS_2, and a saturated lipid (DPPC), which can serve as an active component in chemical sensors. The vibrational spectra show that the organization of liposomes on the surface of either graphene or WS_2 depends on the size and packing of the flakes in the under-.layer . In addition, because of the importance of disulfide bonds in detecting many proteins, we were interested in the interaction between the amino acid cysteine and WS_2.

REFERENCES

[1] J. Ziheng *et al*, *ACS Nano* **11** (2017), 12020-12026
[2] M. Hertz *et al*, *Nanoscale* **8** (2016), 15147
[3] GP Nicoleli *et al*, *C Journal of carbon research* **3** (2017), 9
[4] F. Li *et al*, *Electroanalysis* **27** (2015), 2098 - 20115

29th Summer School and International Symposium on the Physics of Ionized Gases

Aug. 28 - Sep. 1, 2018, Belgrade, Serbia

CONTRIBUTED PAPERS
&
ABSTRACTS OF INVITED LECTURES, TOPICAL INVITED LECTURES, PROGRESS REPORTS AND WORKSHOP LECTURES

Editors:
Goran Poparić, Bratislav Obradović,
Duško Borka and Milan Rajković

Vinča Institute of
Nuclear Sciences

Serbian Academy
of Sciences and Arts

CONTRIBUTED PAPERS & ABSTRACTS OF INVITED LECTURES, TOPICAL INVITED LECTURES, PROGRESS REPORTS AND WORKSHOP LECTURES

of the 29th Summer School and International Symposium on the Physics of Ionized Gases

August 28 – September 1, 2018, Belgrade, Serbia

Editors:
Goran Poparić, Bratislav Obradović,
Duško Borka and Milan Rajković

Publisher:
Vinča Institute of Nuclear Sciences,
University of Belgrade,
P.O. Box 522,
11001 Belgrade, Serbia

Computer processing:
Tatjana Milovanov

Printed by
Skripta Internacional, Mike Alasa 54, Beograd

Number of copies
200

ISBN 978-86-7306-146-7

CONTENTS

Section 1. ATOMIC COLLISION PROCESSES

Invited Lectures

Topical Invited Lectures

MODIFICATIONS OF 2D-MATERIAL-ORGANIC THIN FILMS HETEROSTRUCTURES PRODUCED BY MONOENERGETIC ELECTRON BEAM

Radmila Panajotović and Jasna Vujin

Graphene Lab, Center for solid state physics and new materials, Institute of Physics, Pregrevica 118, 11080, Belgrade, Serbia

An extensive use of 2D-materials as solid support for organic materials, either as a base for electronic devices, such as organic Field-Effect Transistors, or scaffolds for growing organ tissue for implants, is not accidental. Graphene, MoS_2, WS_2, MgB_2, and quite recently hematene are extraordinary useful as mechanically resistant and allegedly non-toxic thin films with tunable electric properties. In biochemical sensors, interactions of various chemical agents with the 2D-material substrate change their electrical properties and can produce an electrical signal that corresponds to the concentration of molecules on their surface. Therefore, the molecular binding and charge transfer in these devices is governed by the chemical and electrical properties of the interface, as well as by its homogeneity and roughness.The same applies to the growth of organic tissue.
In our experiment we used the Scanning Electron Microscope (SEM) to modify the electrostatic status of thin lipid/graphene and lipid/WS_2 films. We showed that the SEM beam tuned to its typical values of power and energy for imaging organic samples could be used as a lithography tool for electrical and chemical modification of lipid/2D-material heterostructures, without inducing significant changes in the morphology of the surface.

Acknowledgements:

This work is supported by the Ministry of education, science and technological development of the Republic of Serbia under the grant IO 171005. We thank Mr. Vladimir Lazović for the technical help with the use of Scanning Electron Microscope.

REFERENCES

[1] Ann E. Oliver, Atul N. Parikh, Biochimica et Biophysica Acta, 1798, 839-850 (2010)
[2] Nathaniel S. Green, Michael L. Norton, Analytica Chimica Acta, 853, 127-142 (2015)
[3] Yuqing Wang, Yi Feng, Yangming Chen, Fei Mo, Gang Qian, Dongbo Yu, Yang Wang and Xuebin, Zhang, Phys.Chem.Chem.Phys, 17, 2678 (2015)